Title	Petrology and geochemistry of the 1991 Pinatubo eruption, Philippines : Implications for the pre-eruptive processes and their time scale
Author(s)	田村, 智弥; Tamura, Tomohisa
Degree Grantor	北海道大学
Degree Name	博士(理学)
Dissertation Number	甲第14732号
Issue Date	2021-12-24
DOI	https://doi.org/10.14943/doctoral.k14732
Doc URL	https://hdl.handle.net/2115/84377
Type	doctoral thesis
File Information	Tomohisa_Tamura.pdf

Doctoral Dissertation

Petrology and geochemistry of the 1991 Pinatubo eruption, Philippines: Implications for the pre-eruptive processes and their time scale

（フィリピン、1991 年ピナツボ火山噴火の岩石学および地球化学：噴火準備過程と時間スケールの解明）

Tomohisa Tamura

Graduate School of Science, Hokkaido University
Department of Natural History Sciences

2021. 12

Contents

Part 1: Petrological and geochemical insight into magma plumbing model of the 1991 Pinatubo eruption

Part 2: Time scale of pre-eruptive processes of the 1991 Pinatubo eruption: Investigation into diffusion profile of phenocryst minerals

Abstract

Although caldera-forming large-scale eruptions are infrequent, they claim lives and cause serious damage to economic activities in their wake. It is necessary to understand the formation and evolution of the magma plumbing system deep beneath the volcano and the precursory phenomena observed during the pre-eruptive process to predict the occurrence of such large-scale eruptions and take countermeasures against them. The 1991 Pinatubo eruption, Philippines is suitable for the above study. This eruption had a VEI (Volcanic Explosivity Index) of 6, the largest eruption since the latter half of the 20th century. Modern geophysical observations were made before the eruption. Although many petrological and geophysical studies have been conducted on this eruption, the large dacitic magma chamber formation, its eruptive processes, and time scales need to be re-examined. In this study, we re-examine the petrological and geochemical properties of the 1991 eruption to clarify the pre-eruptive process, its time scale, and the relationship between time scale and geophysical data. The final objective is to provide a guideline to monitor large-scale eruption above VEI=6. This paper is divided into three parts. In Part 1, petrological and geochemical studies of the 1991 eruption is carried out to re-examine the formation process of dacitic magma. In the previous studies, it was thought that a homogenous large dacitic magma chamber was injected by basaltic magma from below just before the eruption, and that an andesitic magma erupted by magma mixing between dacitic and basaltic magmas, followed by the eruption of dacitic magma. However, this study revealed significant compositional diversity can be explained by mixing between dacitic magmas of different compositions and temperatures. These mixed dacitic magma could not have been formed by crystallizing the basaltic magma that erupted during the 1991 eruption. Still, they must have been generated by partial melting of the crustal material. In this case, the heterogeneity of the crustal material, and the pressure and thermal gradients in the melting region is expected to produce a variety of silicic melts. The injection of basaltic magma resulting in the heterogeneous dacitic magma generation by the above process. In Part 2, we analyzed the diffusion profile of the compositional zoning structure of phenocryst minerals to estimate the pre-eruptive process time scale. The target phenocryst minerals were quartz and titano-magnetite. Considering the elemental diffusion rate in each crystal, we estimated the time scales of the formation of the dacitic magma chamber and the mixing of basaltic and dacitic magmas. The diffusion time obtained from the analysis of diffusion profiles is 3-400 years

(mostly within 30 years) for quartz in dacite, and no zoning structure was observed in titano-magnetite in dacite. The inner part of quartz shows oscillatory zoning, which is consistent with the Part 1 inference, that the accumulation of silicic melts was repeated. In basalts, high-Ti rims are observed in quartz, and titano-magnetite in andesite showed zoning structure. Their time scales ranged between 1.1-3.3 days for quartz and 0.08-50 days (mostly within 3 days) for titano-magnetite. These results suggest that the accumulation of silicic melts started 400 years ago and that the magma chamber was almost completely formed 3 years before the eruption. In addition, the magma chamber may have proliferated 30 years before the eruption. Contrarily, the magma mixing due to the injection of basaltic magma started 50 days before the eruption and continued until just before the eruption. In particular, the growth of andesitic magma due to magma mixing may have proceeded rapidly 3 days before the eruption. A swarm of shallow low-frequency tremors and rapid increase in SO_2 emission were observed in the pre-eruption observation data, 3 days before the eruption, is interpreted as andesitic magma rising in the shallow volcanic conduit. The time scale of titano-magnetite indicates that andesitic magma may have increased 3 days before the eruption, suggesting that magma mixing continued as it ascended the volcanic conduit. There is no contradiction between the magmatic processes inferred by material scientific methods and the interpretation of the observed data. Contrarily, the formation process of dacitic magma cannot be verified by observational data because it takes hundreds of years. Still, the rapid growth of magma chamber 30 years before the eruption suggests the possibility of capturing a precursor phenomenon of large-scale eruptions by observing order of decades, especially by geodetic methods. In Part 3, concluding remarks, we propose guidelines for monitoring large-scale eruptions, mentioning future research implications of the Pinatubo volcano. In this study, we focused on the 1991 eruption. However, Pinatubo volcano has been active for about one million years and has had seven silicic magmatic eruptions in the last 40,000 years. This suggests that a large-scale silicic magmatic system was present before the 1991 eruption. Therefore, clarification on pre-eruptive process and its time scale for the active period before 1991 could help us understand the long-term evolution of the magma plumbing system. In the future, it is necessary to undertake more such studies of large-scale eruptions to understand the evolution of the magma plumbing system and identify volcanoes that require priority monitoring by investigating and organizing their past eruptive history. Furthermore, by continuously monitoring and accumulating geophysical observation data for at least several decades, we may detect precursor phenomena of large-scale eruptions that can predict eruptions in the future.

Introduction

Large-scale eruptions are those with VEI=5 or higher (Newhall and Self, 1982). Although they are infrequent, if they do occur, lives are lost and they have a significant impact on economic activities, causing tremendous damage. Past large-scale eruptions in Japan include the Aso-4 pyroclastic flow eruption about 90,000 years ago (Ono and Watanabe, 19850) and the Kikai caldera eruption about 7,300 years ago (Machida and Arai, 1978), both of which formed calderas by large-scale eruptions. The importance of large-scale volcanic eruptions began to be recognized in the new regulatory standards established in response to the nuclear disaster caused by the Great East Japan Earthquake in 2011. The new regulatory standards require monitoring of volcanoes that have had large-scale eruptions in the past, such as those that formed calderas, as a condition for restarting nuclear power plants. For example, Sendai Nuclear Power Plant in Kagoshima, south Kyushu, where many caldera volcanoes, most of which are distributed in Kyushu are monitored. In other words, predicting large-scale eruptions will be important for the safe and secure operation of nuclear power plants.

To predict large-scale eruptions, it is necessary to understand the formation and evolution of magma plumbing system deep beneath a volcano and recognize the pre-eruptive process as a precursor phenomenon. For this, it is important to estimate the time scale by petrological methods, such as diffusion profiles of phenocryst minerals. The new regulatory standards for nuclear power plants include two criteria for the monitoring system: crustal deformation and magma supply rate. However, only the research results of Druitt et al. (2012) used for these two criteria.

Furthermore, the Minoan eruption of the Santorini volcano in Greece, which was the subject of Druitt et al. (2012), occurred in 1,600 B.C. Naturally, there was no geophysical observation data before the eruption. In other words, the criteria for the new regulatory standards based on time scales estimated from petrological methods has not been proven from geophysical observed data.

To solve these problems, it is necessary to clarify the pre-eruptive process time scale and verify the results from geophysical observations. Although there are several examples of such studies (Tomiya et al., 2013; Kilgour et al., 2014; Moore et al., 2014, Rae et al., 2016; Viccaro et al., 2016), all of them are for small- to medium-scale eruptions, and their results cannot be directly applied to large-scale eruptions. Therefore, it is necessary to select volcanic eruptions that are enormous and for which there are geophysical observations recorded before the eruption. A volcanic eruption that fits this description is the 1991 Pinatubo eruption.

Pinatubo volcano, located in the northern part of Luzon island, Philippines, experienced its largest eruption in the latter half of the 20th century in 1991 (Schmincke, 2004). A phreatic eruption on April 2 was followed by the climactic eruption on June 15, which recorded a VEI=6 (Scott et al., 1996). In response, geophysical observations were initiated by members of PHIVOLCS (Philippine Institute of Volcanology and Seismology) on April 5 (Lockhart et al., 1996). Subsequently, members of the U.S. Geological Survey entered in late April, and the epicenter of the volcanic earthquake was identified in early May. Thus, up to two months of geophysical data have been recorded before the eruption. On the other hand, although many petrological and geophysical studies have been carried out on the 1991 eruption, the large-scale dacitic magma chamber formation and eruptive processes need to be re-examined, including their time scales.

In this study, we re-examine the petrological and geochemical properties of the 1991 eruption to clarify the pre-eruptive process, its time scale, and the relationship between time scale and geophysical observations. The final objective is to provide a guideline for the monitoring of large-scale eruptions of VEI=6 and above. This paper is divided into three parts. In Part 1, we review the formation process of dacitic magma and discuss the pre-eruptive process of the magma plumbing system. In Part 2, we examine the time scale of the pre-eruptive process and discuss the relationship between the time scale and geophysical observations. Finally, in Part 3, we conclude with guideline for monitoring large-scale eruptions.

Part 1:

Petrological and geochemical insight into magma plumbing model for the 1991 Pinatubo eruption

Abstract

The magmatic processes of the 1991 Pinatubo eruption are widely considered to be typical of large explosive silicic eruptions. Previous studies have shown that basaltic magma was injected into a homogeneous dacitic magma chamber just before eruption to form a hybrid andesitic magma. Ascent of the hybrid magma through the chamber generated the initial eruption, which was followed days later by the climactic eruption of the dacitic magma. Here, we present new petrological and geochemical analyses of the juvenile eruptive products, which reveal that the basaltic magma was injected not into a homogeneous dacitic magma, but into a hybrid dacitic magma. Compositional variations of plagioclase and amphibole phenocrysts and whole rock chemistry of dacitic pumices suggest that the hybrid dacitic magma was formed by the mixing of at least two distinct silicic end-member magmas. The whole-rock major and trace element and isotopic chemistry of the dacitic pumices suggests that these end-member magmas could not have been produced by the fractional crystallization of either the 1991 basaltic magma or the previous Buag period basaltic magma (~1.0-0.5 ka). Moreover, trace element variations preclude the formation of the more silicic end-member magma by factional crystallization of the less silicic one. Thus, the silicic end-member magmas were produced independently, but simultaneously, by the melting of heterogeneous crustal materials. Based on these results, we conceptualize the pre-eruptive processes of the 1991 Pinatubo eruption as follows. First, basaltic magma distinct from that of the Buag period underplated and heated the crust to form silicic melt pockets of varied compositions in a lower crustal mush zone. Then, these silicic melts were extracted from the mush, ascended through the crust, and accumulated as a silicic melt-rich magma at shallower depths within the mush zone. The accumulation process can be approximated as the mixing of two silicic end-member magmas. The formation and growth of the hybrid silicic magma continued from 0.5 ka until 1991, forming the 1991 shallow dacitic magma chamber. Just before the 1991 eruption, basaltic magma was injected into the hybrid dacitic magma chamber, triggering the eruption. We concluded that the pre-eruptive processes and the evolution of the magma plumbing system of the 1991 eruption required an unrest for 500 years in maximum.

Chapter 1: Introduction

Forecasting future volcanic eruptions requires an understanding the pre-eruptive processes from the formation and evolution of the magma plumbing system until eruption. Because large silicic eruptions tend to be highly explosive and hazardous, the structure of silicic magma chambers have been widely discussed. Several large eruptions were produced from zoned magma chambers in which compositional and thermal gradients were developed through silicic magma differentiation (e.g., McBirney et al., 1985; Streck and Grunder, 2008) and mafic injections, forming layers of hybrid magma (e.g., Wiebe, 1988; Bindeman and Bailey, 1994; Kaneko et al., 2007). Previous petrological studies of large explosive silicic eruptions have shown that mafic injections into large silicic magma chambers can trigger eruptions (e.g., Sparks et al., 1977; Pichavant et al., 2002; Eichelberger et al., 2006; Watanabe et al., 2006). Such triggering processes are short-term precursor phenomena that could be detectable by dense geophysical monitoring networks (e.g., Tomiya et al., 2013; Rae et al., 2016; Viccaro et al., 2016).

The processes by which large silicic magma bodies form have also been discussed. Hildreth and Wilson (2007) showed that silicic magma chambers form by the accumulation of silicic melt from a mushy magma body (e.g., Hildreth, 1981; Bacon and Druitt, 1988; Bachmann and Berganz, 2004; Marsh, 2015). The simultaneous generation of several silicic magmas via their independently stagnation in multiple magma chambers has also been proposed (e.g., Cooper et al., 2012); mixing of these distinct magmas forms large silicic chambers of hybrid composition (Druitt et al., 2012; Matsumoto et al., 2018). Such formation processes occur over longer periods, months to years or longer, preceding large silicic eruptions. To understand and properly evaluate possible precursor volcanic activity, these long-term processes should be carefully investigated for previous eruptions.

The 1991 cataclysmic eruption of Pinatubo volcano, northern Luzon Island, Philippines (Wolfe and Hoblitt, 1996; Paladio-Melosantos et al., 1996), erupted ~5 km^3 dense rock equivalent of dacitic magma (Scott et al., 1996) in the largest silicic eruption of the last century. Detailed petrological studies have revealed that the 1991 eruption began with the injection of basaltic magma into the voluminous dacitic magma chamber, which formed a hybrid andesite magma. This hybrid magma then ascended through the dacitic chamber and was erupted in the initial eruption on June 7 and 12, followed by the climactic eruption of the dacitic magma on

15 June (Pallister et al., 1992; Pallister et al., 1996; Daag et al., 1996; Bernard et al., 1996; Hattori and Sato, 1996). This model for the 1991 eruption (Pallister et al., 1992) is considered typical of large explosive silicic eruptions. Hammer and Rutherford (2003) and Borisova et al. (2014) proposed the volume and location of the magma reservoir tapped during the 1991 eruption, and other geochemical and experimental studies have discussed the origin and variation of the 1991 dacitic magma (e.g., Bernard et al., 1996; Scaillet and Evans, 1999; Prouteau and Scaillet, 2003; Jego et al., 2005). Nonetheless, the processes by which the dacitic magma formed are not yet fully understood.

To better understand the pre-eruptive processes of the 1991 eruption, it is essential to clarify the diversity and evolution of the erupted dacitic magma prior to eruption. Here, we reinvestigated the diversity of the 1991 eruptive products. Whereas previous studies considered the 1991 Pinatubo dacite magma to have been homogeneous (e.g., Pallister et al., 1992; Bernard et al., 1996), our results reveal variations of its chemical compositions, magmatic temperature, and storage depth. Based on these results, we propose a model for the formation and evolution of the magmatic plumbing system of the 1991 Pinatubo eruption. Moreover, we compare the 1991 eruption to the previous eruption of Pinatubo, the Buag period eruption ca. 500 years ago (Newhall et al., 1996; Muro et al., 2008), to discuss the genesis of the 1991 Pinatubo magmatic system.

Chapter 2: Sequence of 1991 eruption and samples

Pinatubo awoke in 1991 from about 500 years of quiescence since the Buag period eruption (Newhall et al., 1996). The 1991 eruptive sequence is summarized in Figure 1. A felt earthquake was reported late on March 15 (Sabit et al., 1996) and eruptive activity began with a phreatic eruption on April 2, 1991. A lava dome appeared at the summit on June 7 and grew over the following days, before being destroyed by the first Plinian eruption on June 12. The climactic eruption began on June 15 and continued for 9 to 10 hours; this eruptive duration was confirmed by the infrasonic wave at Kariya, Japan (Tahira, 1992; Tahira et al., 1996). Continues eruptive activity clearly decreased after an eruption on September 2. After a period of quiescence, another lava dome was emplaced in the summit crater from July to October in 1992.

Here, we focus on juvenile samples from three main events of the 1991 eruption: the lava dome extruded on June 7, the first Plinian eruption on June 12, and the climactic eruption on June 15 (Fig. 1). The lava dome on June 7 (hereafter. 'June 7 lava') contained mafic enclaves ('June 7 enclave'). Gray, vesicular scoria was erupted on June 12 ('June 12 scoria'). Juvenile materials of June 15 climactic eruption are divided into two types of pumice, white, vesicular, phenocryst-rich ('June 15 Ph-rich pumice') and gray, massive, phenocryst-poor pumice ('June 15 Ph-poor pumice'). Based on Pallister et al. (1996), we use 'Ph-rich' and 'Ph-poor'. Although single sample of the June 7 enclave was investigated, multiple samples of other types were available, respectively.

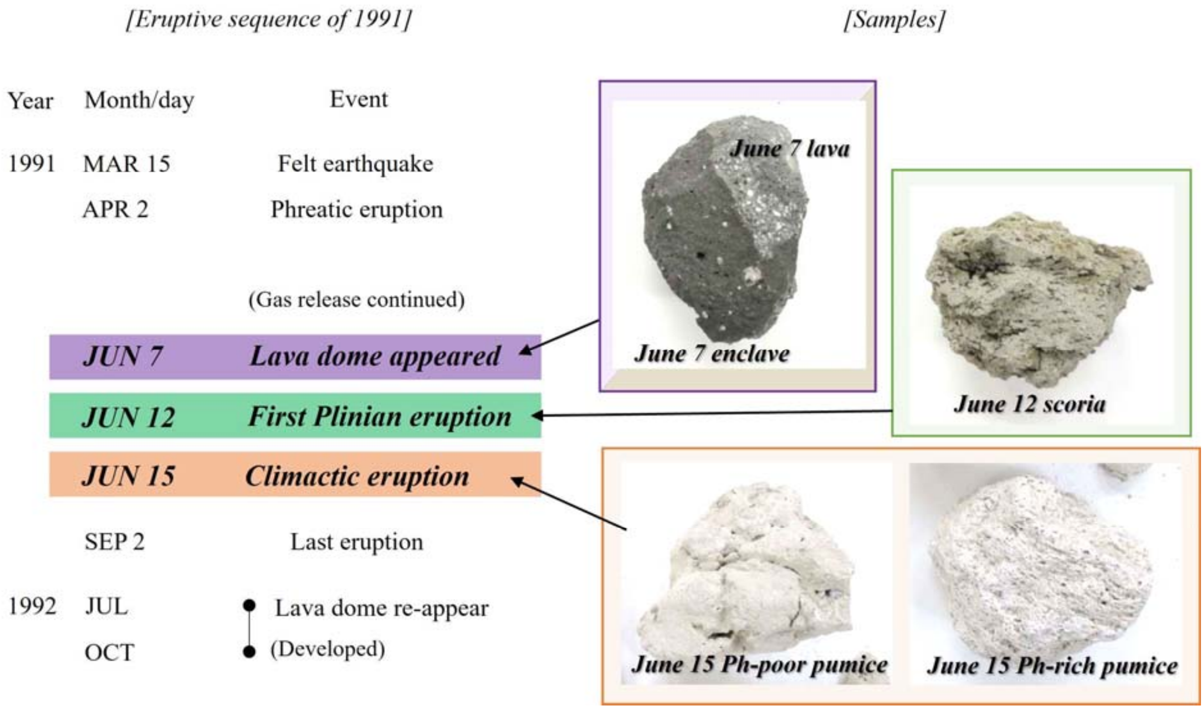

Fig. 1. Juvenile rock samples of the 1991 Pinatubo eruption used in this study. We examined five types of juvenile samples from three main events of the 1991 eruption: the dome lava extruded on June 7 (June 7 lava), a mafic enclave included in the lava dome fragment (June 7 enclave), scoria erupted during the first Plinian eruption on June 12 (June 12 scoria), and white, phenocryst-rich pumices and gray, phenocryst-poor pumices erupted during the climactic eruption on June 15 (June 15 Ph-rich pumice and June 15 Ph-poor pumice, respectively).

Chapter 3: Analytical methods

All samples were prepared and analyzed at Hokkaido University.

3.1. Modal analysis

Modal phenocryst contents of representative samples were determined by point counting of thin sections with grids drawn at intervals of 500 µm. We counted 1,000-2,000 points in each thin section. Following Wilcox (1954), crystals larger and smaller than 0.3 mm were counted as phenocrysts and groundmass, respectively.

3.2. EPMA

Mineral chemical analyses were performed using the JEOL-8800R electron probe microanalyzer operating 15 kV accelerating voltage and using a focused beam for all minerals; the beam current was set to 10 nA for plagioclase, 15 nA beam for amphibole and biotite, and 20 nA beam current for Fe-Ti oxides, olivine, and clinopyroxene, respectively. Mineral core and rim compositions were determined at centers and edges of minerals. Matrix glass compositions of juvenile materials in dacitic pumices were determined using the same microanalyzer operating at 15 kV accelerating voltage and 10 nA beam current, with a 2-µm diameter beam scanning a 10 × 10 µm square area. To avoid Na migration, X-ray data for Na were counted only for the first 30s. Corrections for all analysis using the microanalyzer were performed using the ZAF method.

3.3. XRF

Whole rock compositions were determined by X-ray fluorescence (XRF), using a Spectris MagiX PRO system with a Rh tube. Major and trace elements were measured using glass beads prepared by fusing the sample powder with an alkali flux (a 1:4 mixture of lithium tetraborate and lithium metaborate); major and trace elements were measured for 30 samples with enough size diluted to 1:2 and only major elements were measured for 4 samples with smaller size diluted to 1:10.

3.4. ICP-MS

Trace and rare earth elements (REE) were determined for selected 19 samples by inductively coupled plasma mass spectrometry (ICP-MS) using a Thermo Fisher Scientific X-series device. All the samples were prepared by the alkali fusion method (Roser et al., 2000). About 100 mg of powdered sample was digested in a 1:1 mixture of HCl and HF. After drying, the residual sample was fused with 500 mg of Na_2CO_3 at 1050 ˚C in a muffle furnace for ten minutes. The fused sample was then dissolved with 5% HNO_3, HCl and small amount of HF with a dilution factor of 20,000.

3.5. MC-ICP-MS

The Sr-Nd-Pb isotopic compositions of the same 19 samples were determined by multi collector ICP-MS (Neptune plus, a Thermo Fisher Scientific) All the samples were prepared by the methods of Pin et al. (1994) and Noguchi et al. (2011) for Sr, Pin et al. (1994) and Pin and Zalduegui (1997) for Nd, and Kuritani and Nakamura (2002) for Pb. Sr and Nd mass fraction factors were corrected using $^{86}Sr/^{88}Sr = 0.1194$ and $^{146}Nd/^{144}Nd = 0.7219$, respectively. That of Pb was corrected using Tl as an external standard ($^{205}Tl/^{203}Tl=2.3871$: Dunstan et al., 1980). Our analytical accuracy and reproducibility were monitored by analyses of the NIST987 standard for Sr, JNdi-1 standard for Nd, and NIST981 for Pb. Corrected data were normalized to $^{87}Sr/^{86}Sr = 0.710240$ for NIST987, $^{143}Nd/^{144}Nd = 0.512117$ for JNdi-1, and $^{206}Pb/^{204}Pb = 16.9424$, $^{207}Pb/^{204}Pb = 15.5003$ and $^{208}Pb/^{204}Pb = 36.7266$ for NIST981 (Kuritani and Nakamura, 2002). The isotopic ratios of the JB-3 (Geological Survey of Japan standard) were measured during the present study. The obtained values were consistent with those of Kuritani et al. (2017).

Chapter 4: Petrology and Mineral chemistry

Juvenile materials of the 1991 eruption are represented by five materials, June 7 andesitic dome lava and basaltic enclave, June 12 andesitic scoria, and June 15 phenocryst-rich (Ph-rich) and -poor (Ph-poor) dacitic pumices (Fig. 1). The two types of June 15 dacitic pumices have the same phenocryst assemblages and chemical compositions of major phenocrysts. Similarly, the June 7 andesitic dome lava and June 12 andesitic scoria share the same phenocryst assemblages. Detailed petrographical features of these rocks were described by Pallister et al. (1996). Thus, we briefly describe the petrography and mineral chemistry of the five juvenile materials, grouped by rock name in the subsections below.

4.1. Dacite - pumices from the June 15 climactic eruption

The June 15 Ph-rich pumices (Fig. 2a) contain 11.9-22.3 vol.% phenocrysts (Table 1); the major phenocryst phases are plagioclase (8.0-16.6 vol.%), amphibole (1.2-8.1 vol.%), and quartz (≤2.8 vol.%). Minor phenocrysts are olivine (≤0.1 vol.%), clinopyroxene (≤0.3 vol.%), biotite (≤2.6 vol.%), and oxides minerals (≤0.4 vol.%) such as titano-magnetite and ilmenite. Several plagioclase (<2.4 mm) and amphibole (<2.7 mm) phenocrysts show oscillatory zonings. Amphibole phenocrysts are hornblende (Fig. 2f, Table 2), and some show thin reaction rims of cummingtonite. Biotite occurs as both isolated phenocrysts and reaction rims around hornblende phenocrysts. Quartz phenocrysts are ovoid to tabular, and some present resorbed rims. Groundmass is glassy to hyalo-ophitic with microlites of plagioclase, amphibole and opaque minerals.

The June 15 Ph-poor pumices (Fig. 2b) are gray vesicular to massive, and contain 3.2-5.7 vol.% phenocrysts (Table 1). As in the Ph-rich pumices, the major phenocryst phases are plagioclase (2.5-3.7 vol.%), amphibole (0.3-1.1 vol.%), and quartz (0.2-1.0 vol.%). Minor phenocrysts are olivine (≤0.1 vol.%) and Fe-Ti oxides (titano-magnetite and ilmenite, ≤0.1 vol.%), but, in contrast to the Ph-rich pumices, biotite and clinopyroxene are not observed. Major phenocrysts usually appear broken and are smaller (plagioclase,<1.3 mm; amphibole,<0.8 mm) than those in the Ph-rich pumices (Table 1). Amphibole phenocrysts are hornblende, but have only thin cummingtonite reaction rims. Quartz phenocrysts are recognizably broken. Groundmass is glassy to hyalo-ophitic with microlites of plagioclase, amphibole and opaque minerals.

The cores of plagioclase phenocrysts have a broad, skewed distribution of An# (100 × Ca/(Ca+Na+K)) with a single peak at An# = 30-40 and a tail of calcic phenocrysts (An#>40) (Fig. 3). Plagioclase phenocrysts with An#<35 usually show reverse zoning, whereas those with higher An# tend to be normally zoned (Fig. 4). The cores of amphibole phenocrysts have a broad distribution of Si content (atoms per formula unit, pfu) with a single peak at 6.8-7.1 and phenocrysts with less Si (<6.8) are rarely observed (Fig. 3). In the Si vs. $(Na+K)_A$ diagram (i.e., Na + K content in the amphibole A site), many amphibole phenocrysts plot as hornblende, whereas those with higher $(Na+K)_A$ values (>0.2) and less Si (<6.5) plot in the tschermakite field (Fig. 5). Although hornblende phenocrysts containing more Si (>6.8) show weak reverse zoning, those with less Si show normal zoning (Fig. 6). The cores of titano-magnetite phenocrysts show a narrow distribution of Mg/Mn ratios with a single peak at Mg/Mn = 3-5 (Fig. 3).

4.2. Andesite – June 7 lava dome fragments and June 12 scoria

Andesitic samples include June 7 lava and June 12 gray, vesicular scoria (Fig. 1). Although the phenocryst content of the 7 June lava dome (29.4 vol.%) is greater than that of 12 June scoria (15.9 ~ 19.1 vo.%; Table 1), the petrography and mineral chemistry of both are similar. Thus, we describe the petrography of the dome lava and scoria together.

Major phenocryst phases (Figs. 2c, d) are plagioclase (10.2-17.1 vol.%), amphibole (3.6-6.0 vol.%), olivine (0.7-2.6 vol.%), clinopyroxene (0.2-1.1 vol.%) and quartz (0.3-2.5 vol.%). Minor phenocrysts are Fe-Ti oxides (titano-magnetite and ilmenite, ≤0.2 vol.%) and biotite (≤0.3 vol.%). Pallister et al. (1996) also reported the presence of anhydrite phenocrysts. Amphibole phenocrysts are generally isolated phenocrysts of hornblende or pargasite, but several hornblende phenocrysts have pargasite reaction rims (Fig. 2g). Crystal clots comprising plagioclase, hornblende, and Fe-Ti oxide minerals are also observed. Plagioclase (< 4 mm) and hornblende (< 3.8 mm) phenocrysts commonly show oscillatory zoning, although some plagioclase phenocrysts have dusty outer rims. Olivine phenocrysts are completely mantled by pargasite reaction rims (Fig. 2c). Quartz phenocrysts are oboid and show rim textures. Groundmass is glassy to hyalo-ophitic with microlites of plagioclase, amphibole and Fe-Ti oxides (Figs. 2c, d).

Plagioclase phenocryst cores show a skewed unimodal An# distribution with a peak at An# = 30-40 and a tail of more calcic phenocrysts (Fig. 3). Although normal and reverse zoned plagioclase phenocrysts coexist as in the dacite sample, those with cores of lower An# (<35-40) obviously show strong reverse zoning with rims of An#>50 (Fig. 4). The Si contents of amphibole phenocryst core range from 5.9 to 7.1, showing two distinct compositional peaks at 6.8-7.1 and 5.9-6.2 (Fig. 3) corresponding to hornblende and pargasite, respectively (Fig. 5). Although the cores of titano-magnetite phenocrysts show a broad distribution of Mg/Mn ratios, many have Mg/Mn = 4-5 (Fig. 3). The cores of olivine and clinopyroxene phenocrysts in the dome lava show similar compositional variations with Mg# (100 × Mg/(Mg+Fe)) = 82-89, whreas clinopyroxenes are less magnesian (Mg# = 79-87) than olivines (Mg# = 85-90) in the scoria (Fig. 3).

4.3. Basalt - mafic enclaves hosted in the June 7 lava dome fragments

We obtained a single mafic enclave (SiO_2 = 53.1 wt.%) hosted in the 7 June dome lava (Fig. 1). This porphyritic sample contains plagioclase (8.8 vol.%), amphibole (6.4 vol.%), olivine (2.9 vol.%) and clinopyroxene (1.4 vol.%), quartz (0.7 vol.%) and titano-magnetite (0.1 vol.%) phenocrysts, and the intersertal groundmass comprises acicular plagioclase and amphibole microlites. Almost all plagioclase phenocrysts (<4.2 mm) show honeycomb structures. Pargasite dominates the amphibole phenocrysts (<1.7 mm), but hornblende phenocrysts mantled by pargasite are often present. Olivine phenocrysts are always surrounded by pargasite reaction rims (Fig. 2h). Quartz phenocrysts are ovoid and show corona structures (Sato, 1975). Titano-magnetite phenocrysts are smaller than 0.7 mm.

Although it was difficult to determine the chemical compositions of plagioclase phenocrysts due to their honeycomb structures, the few analyses that we were able to perform highlight a broad compositional range with An# varying from 30 to 84 (Fig. 3). Most amphibole phenocrysts are pargasite with 6.0-6.4 Si pfu, and hornblende phenocrysts are rare (Fig. 3). The Mg/Mn ratios of titano-magnetite phenocryst cores are varied, ranging from 3 to 11 (Fig. 3). As in the andesitic scoria sample, clinopyroxene phenocrysts are less magnesian (Mg# = 76-88) than olivine phenocrysts (Mg# = 83-90; Fig. 3).

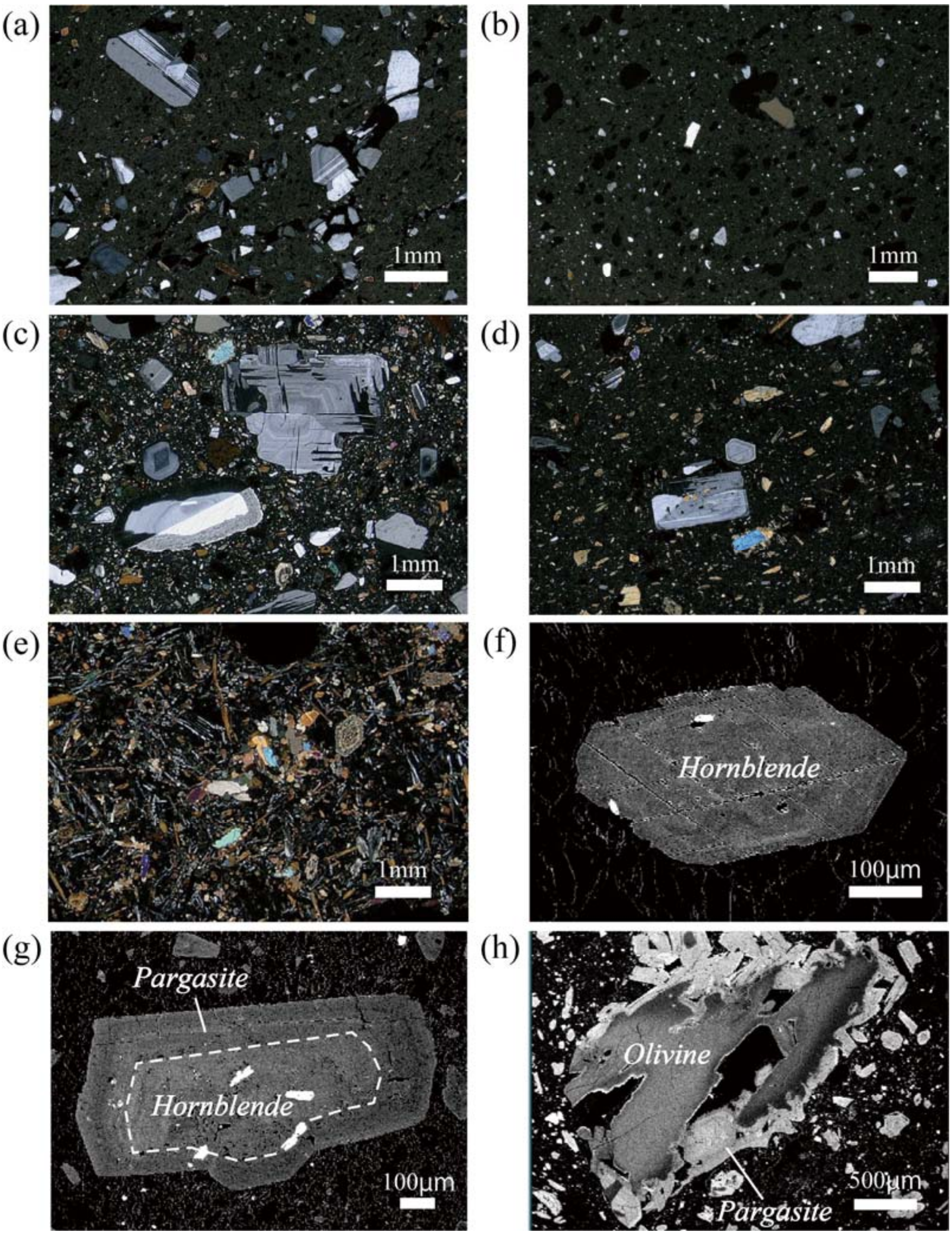

Fig. 2. Photomicrographs of juvenile materials from the 1991 eruption. (a-e) and (f-h) show cross-polarized light and back-scattered electron images, respectively. (a) June 15 Ph-rich dacitic pumice; (b) June 15 Ph-poor dacitic pumice; (c) June 7 andesitic lava dome fragment; (d) June 12 andesitic scoria; (e) basaltic enclave included in the June 7 dome lava; (f) isolated hornblende phenocryst in the June 15 Ph-rich dacite pumice; (g) hornblende phenocryst with pargasite reaction rim on June 12 andesitic scoria; and (h) olivine phenocrysts with pargasitic amphibole reaction rims in the basaltic enclave.

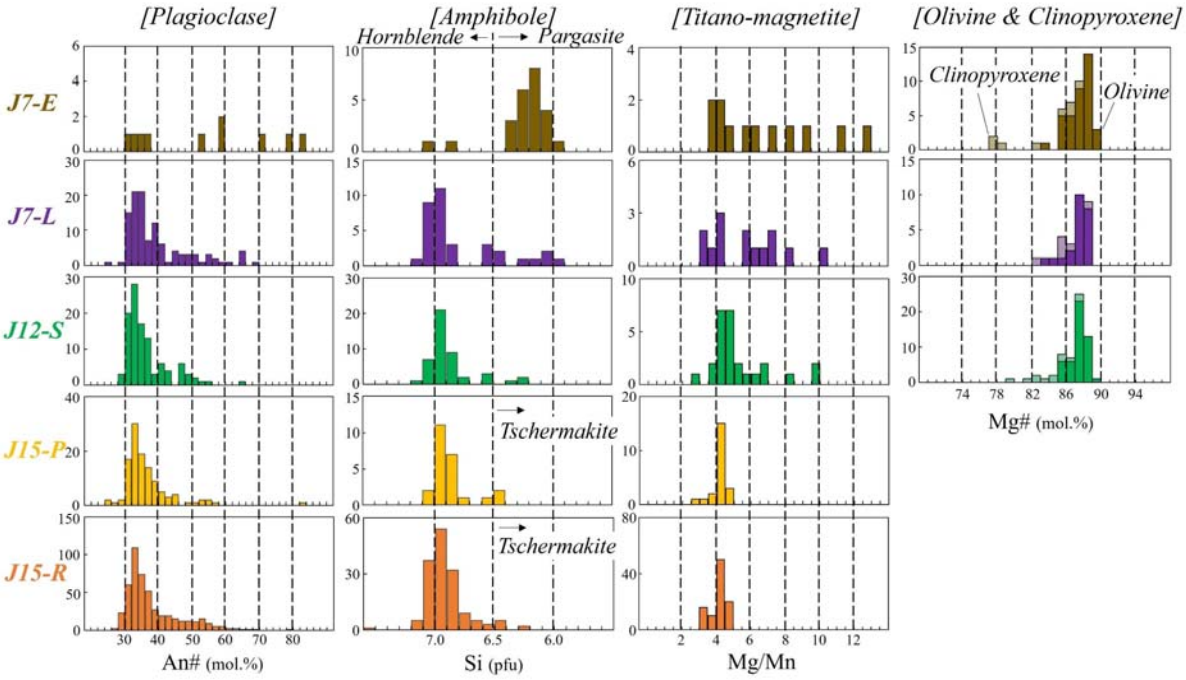

Fig. 3. Distributions of the core compositions of plagioclase, amphibole, titano-magnetite, olivine and clinopyroxene phenocrysts in juvenile materials from the 1991 eruption. Abbreviations: An#, plagioclase anorthite content expressed as 100 × Ca/(Ca+Na+K); Si, Si atom per formula unit (pfu) in amphibole and the corresponding classification between hornblende and pargasite, based on Deer et al. (1992); Mg#, magnesium number in olivine and clinopyroxene expressed as 100 × Mg/(Mg+Fe).

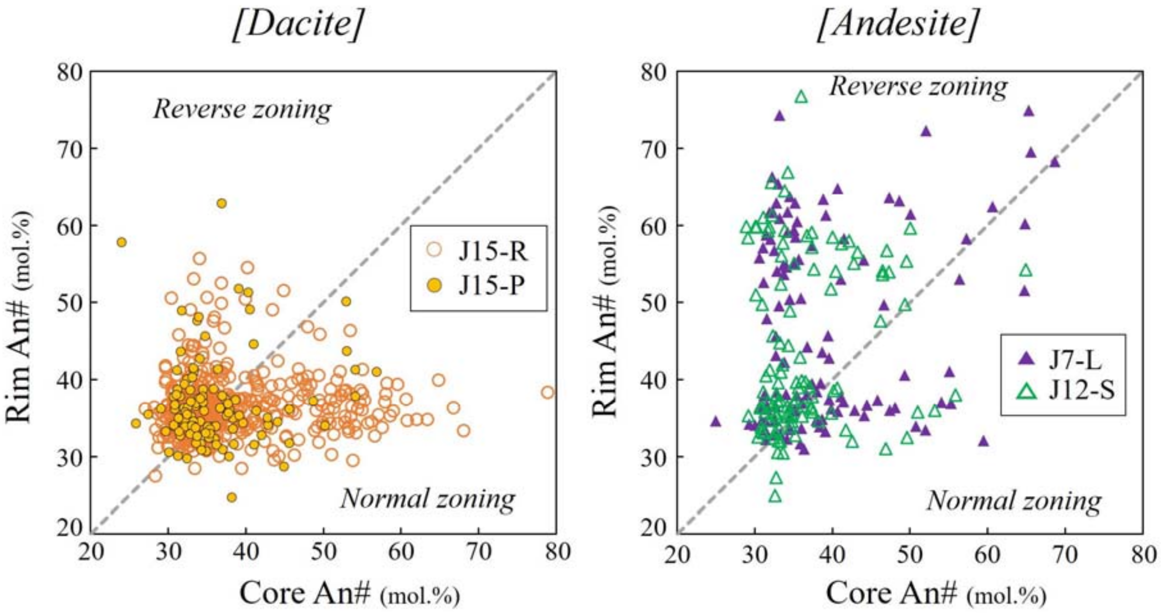

Fig. 4. Core vs. rim diagram of plagioclase in dacite and andesite samples. (a) Open and filled circles are from the June 15 Ph-rich (J15-R) and Ph-poor (J15-P) dacitic pumices, respectively. (b) Open and filled triangles are from the June 12 scoria (J12-S) and June 7 lava (J7-L), respectively.

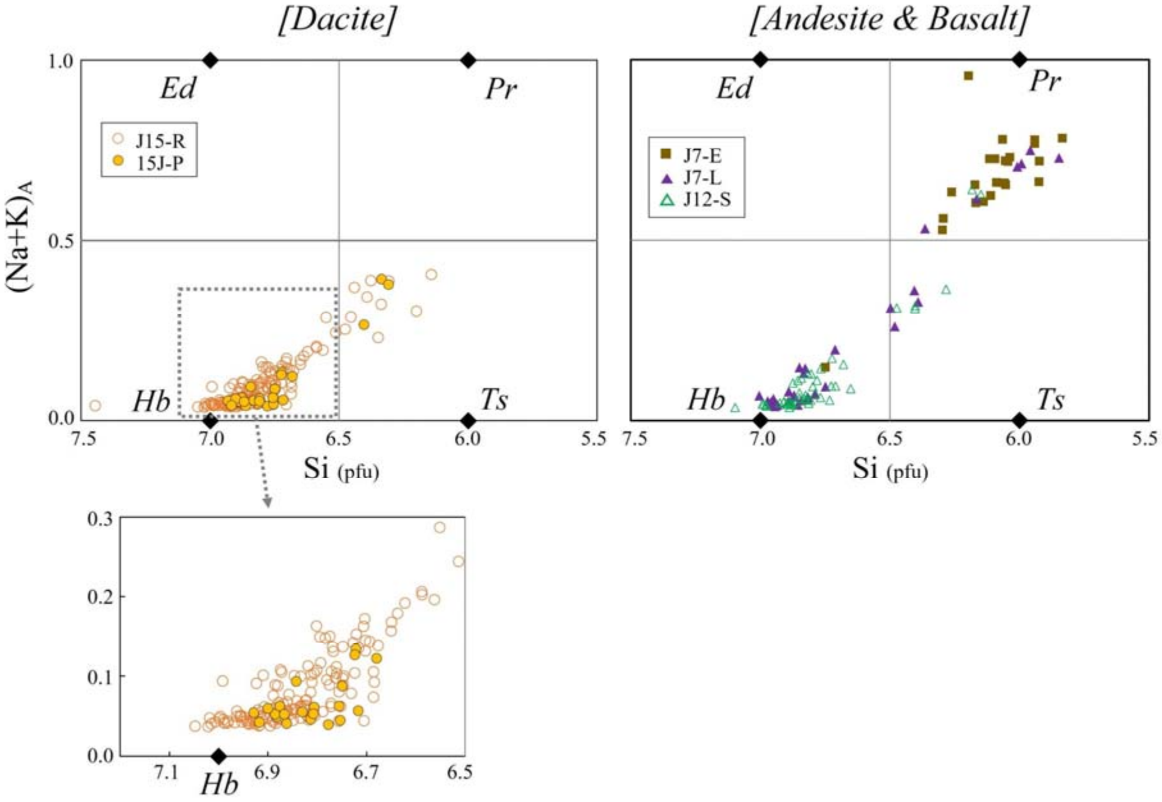

Fig. 5. Classification of amphibole cores in the juvenile 1991 samples. Classification boundaries and end-members are from Deer et al. (1992). This figure shows Si (pfu) against (Na+K) in the amphibole A site in the cores of amphibole phenocrysts, calculated for 13 cations (Leake et al., 1997). End-members are: Ed, edenite; Pr, pargasite; Hb, magnesio-hornblende; and Ts, Tschermakite. (a) Open and filled circles are from the June 15 Ph-rich (J15-R) and Ph-poor (J15-P) pumices, respectively. (b) Enlarged view of the area in (a) near the hornblende end-member. (c) Open and filled triangles are from the June 12 scoria (J12-S) and June 7 lava (J7-L), respectively, and the filled squares are from the June 7 enclave (J7-E).

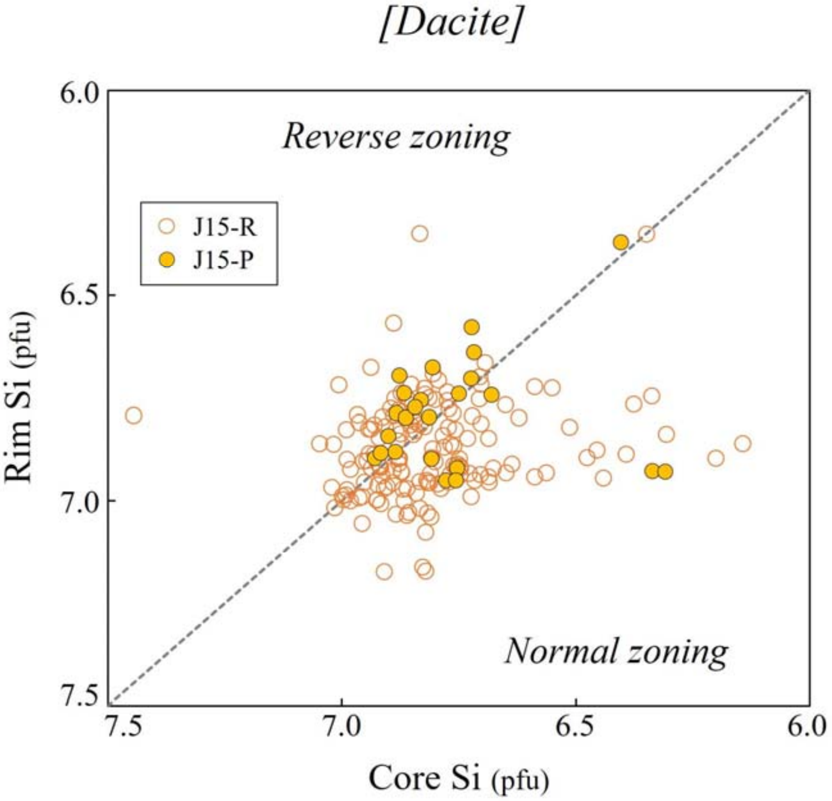

Fig. 6. Core vs. rim diagram of Si contents (pfu) in the 1991 dacitic samples. Open and filled circles are from the June 15 Ph-rich (J15-R) and Ph-poor (J15-P) pumices, respectively.

Table 1. Modal mineral abundances (vol.%, calculated on a vesicle-free basis) of representative samples from the 1991 Pinatubo eruption.

Rock type	Unit	Sample name	Pl	Amp	Ol	Cpx	Bt	Qtz	Opq	Ph
Dacite	J15-R	121205C-Bm3	9.6	1.9	n.c.	n.c.	n.c.	n.c.	0.4	11.9
		121205C-B2	8.0	2.9	n.c.	n.c.	2.6	n.c.	0.2	13.7
		121205C-B3	11.9	1.2	n.c.	n.c.	n.c.	0.4	0.2	13.8
		121202C-B1	14.8	4.8	n.c.	n.c.	n.c.	2.5	0.1	22.3
		120801MPinC-K	13.9	8.1	0.1	0.2	n.c.	0.1	0.1	22.3
		120801MP-a	16.6	3.5	n.c.	0.3	n.c.	n.c.	n.c.	20.4
		120801MP-b	14.8	4.2	n.c.	0.1	n.c.	2.8	0.1	22.0
		(Ave.)[*1]	12.6	3.5	< 0.1	< 0.1	0.1	0.6	0.1	17.0
	J15-P	121205C-C	3.6	1.1	n.c.	n.c.	n.c.	1.0	n.c.	5.7
		121205C-M1	2.6	0.4	n.c.	n.c.	n.c.	0.2	0.1	3.2
		121202C-C	2.5	0.3	n.c.	n.c.	n.c.	0.6	n.c.	3.4
		PH-13-F-PP	3.7	0.3	n.c.	n.c.	n.c.	0.4	n.c.	4.4
		(Ave.)[*1]	3.1	0.5	< 0.1[*2]	n.c.	n.c.	0.5	< 0.1	4.2
Andesite	J12-S	P22892-3A	12.0	4.8	0.7	0.2	0.3	1.1	n.c.	19.1
		P22892-3	10.2	3.6	1.3	0.3	n.c.	0.3	0.2	15.9
		(Ave.)[*1]	11.1	4.2	1.0	0.2	0.1	0.7	0.1	17.5
	J7-L	CN6791-D	17.1	6.0	2.6	1.1	< 0.1	2.5	< 0.1	29.4
Basalt	J7-E	P22892-1A	8.8	6.4	2.9	1.4	n.c.	0.7	0.1	20.3

Picked crystals larger than 0.3 mm in diameter were counted as phenocrysts based on Wilcox (1954).

[*1] Average (Ave.) were calculated for all samples of each lithology: we used 25 samples of the June 15 Ph-rich pumice (J15-R), 4 samples of the June 15 Ph-poor pumice (J15-P), 2 samples of the June 12 scoria (J12-S), and a single sample each of the June 7 lava (J7-L) and the June 7 enclave (J7-E).

[*2] Olivine was very minor, but present, in the June 15 Ph-poor pumice; thus, it was not counted in the individual samples, but assigned an average abundance of <0.1 vol.%.

Abbreviations: Pl, plagioclase; Amp, amphibole; Ol, olivine; Cpx, clinopyroxene; Bt, biotite; Qtz, quartz; Opq, opaque minerals; Ph, total phenocryst content; n.c., not counted.

Chapter 5: Whole rock geochemistry

5.1. Major and trace elements

As in previous studies (Daag et al., 1996; Pallister et al., 1996; Bernard et al., 1996; Hattori and Sato, 1996), our new data clarifies that the juvenile materials of the 1991 Pinatubo eruption comprise dacite, andesite and basalt (Table 2, Fig. 7). SiO_2 contents of almost all June 15 Ph-rich and Ph-poor pumices range from 64.0 to 66.4 wt.%; only two samples have lower SiO_2 contents of 62.0 and 62.8 wt.%. The SiO_2 contents of the June 7 lava are nearly the same as those of the June 12 scoria, both within the range 59.5-60.1 wt.%. The SiO_2 contents of the June 7 enclave from within the dome lava is basaltic, at 53.1 wt.%. Compatible elements of these rocks (such as TiO_2, MgO, CaO and Cr) decrease with increasing SiO_2 contents. In contrast, some incompatible element concentrations (such as K_2O and Rb) are nearly constant, regardless of SiO_2 contents (Table 2, Fig. 7), whereas others (such as Zr and Ba) slightly increase with increasing SiO_2 contents (Fig. 7). Basaltic rocks from the Buag period (Muro et al., 2008) are also plotted in Figure 7; their chemical compositions, especially incompatible element concentrations such as K_2O, Rb and Zr, clearly differ from that of the basaltic enclave from the 1991 eruption, whereas the Ba contents of both basalts are similar.

5.2. Rare earth elements

Chondrite-normalized rare earth element (REE) contents of the basaltic enclave (J7-E) are notably higher than those of the andesites (J7-L and J12-S) and dacites (J15-R and J15-P) (Fig. 8). The REE patterns are characterized by high values of light/heavy REE ratios (L-REE/H-REE), low medium/heavy REE ratios (M-REE/H-REE), and weak Eu anomalies that increase from the basaltic to dacitic samples. These patterns are almost parallel and decrease from the basaltic to the dacitic samples (Fig. 8). For comparison, The H-REE contents of Buag period basalts are similar to those of the 1991 basaltic sample, whereas the L-REE/H-REE ratio of the 1991 basalt is much higher than those of the Buag period (Fig. 8).

5.3. Isotopic chemistry

The Sr-Nd-Pb isotopic compositions of the juvenile materials of the 1991 eruption (Table 2) change (beyond analytical errors) with increasing whole-rock SiO_2 content as follows (Fig. 9): $^{87}Sr/^{86}Sr$ decreases from 0.704335 to 0.704177, $^{143}Nd/^{144}Nd$ increases from 0.512795 to

0.512927, $^{206}Pb/^{204}Pb$ decreases from 18.4593 to 18.4220. The isotopic compositions of the dacitic samples define linear trends in each SiO_2 vs. isotope ratio diagram, but their slopes differ from those defined by the andesite and basalt samples (Fig. 9).

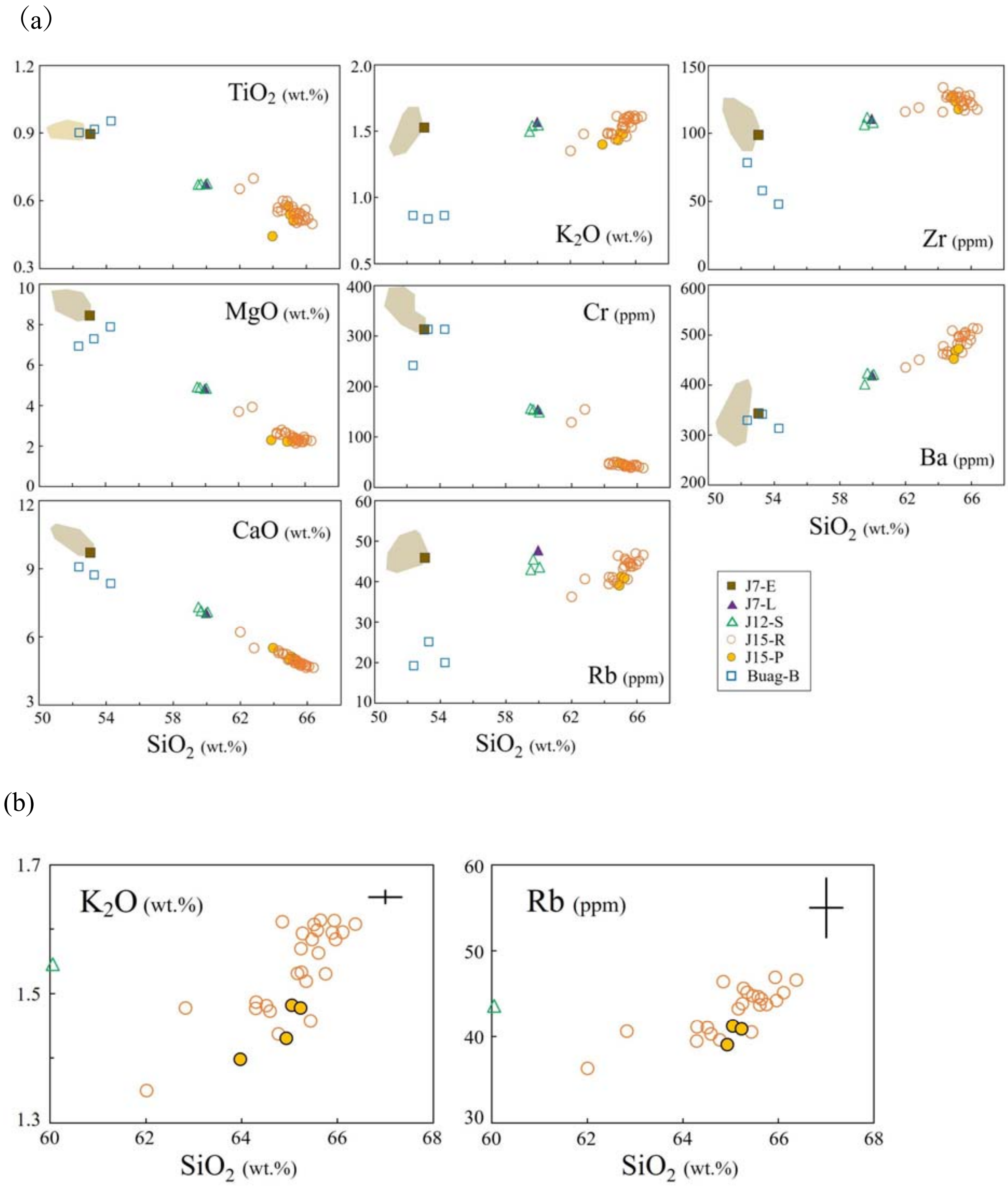

Fig. 7. Whole rock major and trace element compositions of Pinatubo volcanic rocks. (a) The shaded area outlines previous data in 1991 basaltic rocks (Daag et al., 1996; Pallister et al., 1996; Bernard et al., 1996; Hattori and Sato, 1996). In this study, we used exclusively our data on the 1991 basalt because previous data were scattered. Open squares represent the Buag period basalt (Buag-B, ~1.0-0.5 ka; Muro et al., 2008). (b) These figures focus on the composition of dacite. The vertical and horizonal bars show the analytical error.

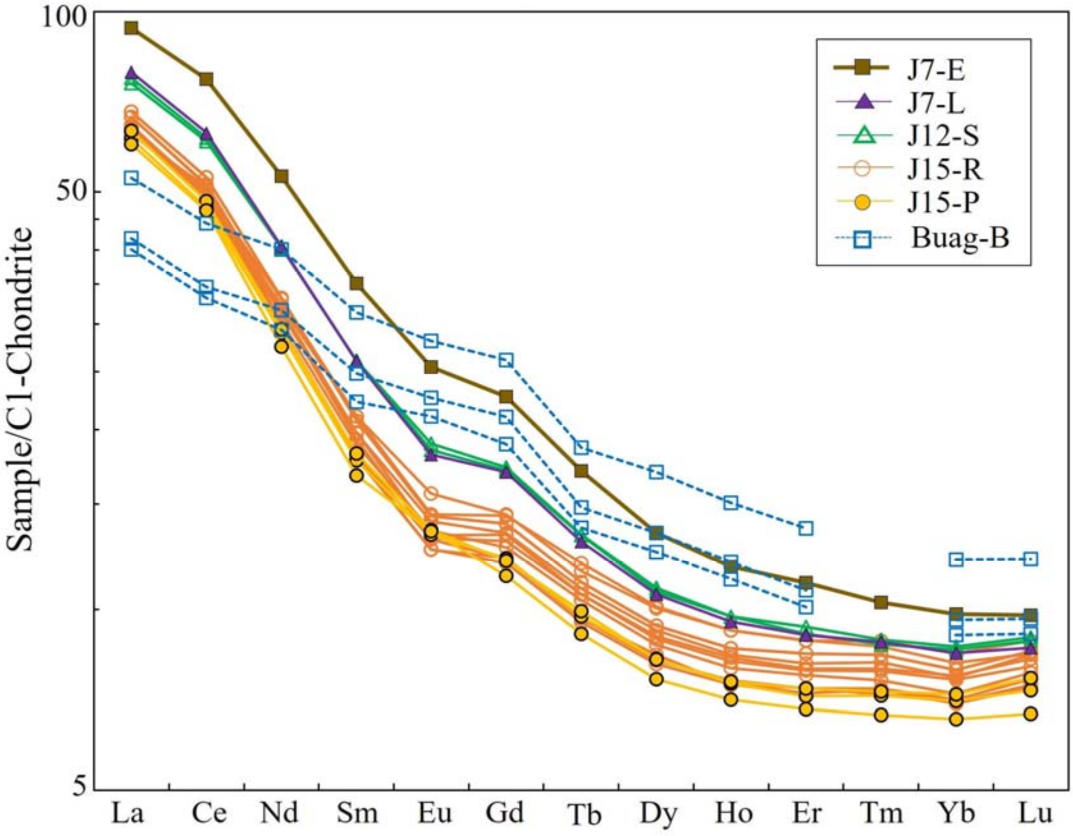

Fig. 8. REE patterns of Pinatubo volcanic rocks normalized to C1-chondrite (Sun and McDonough, 1989). Buag period basalts (~1.0-0.5 ka) from Muro et al. (2008) are plotted for comparison.

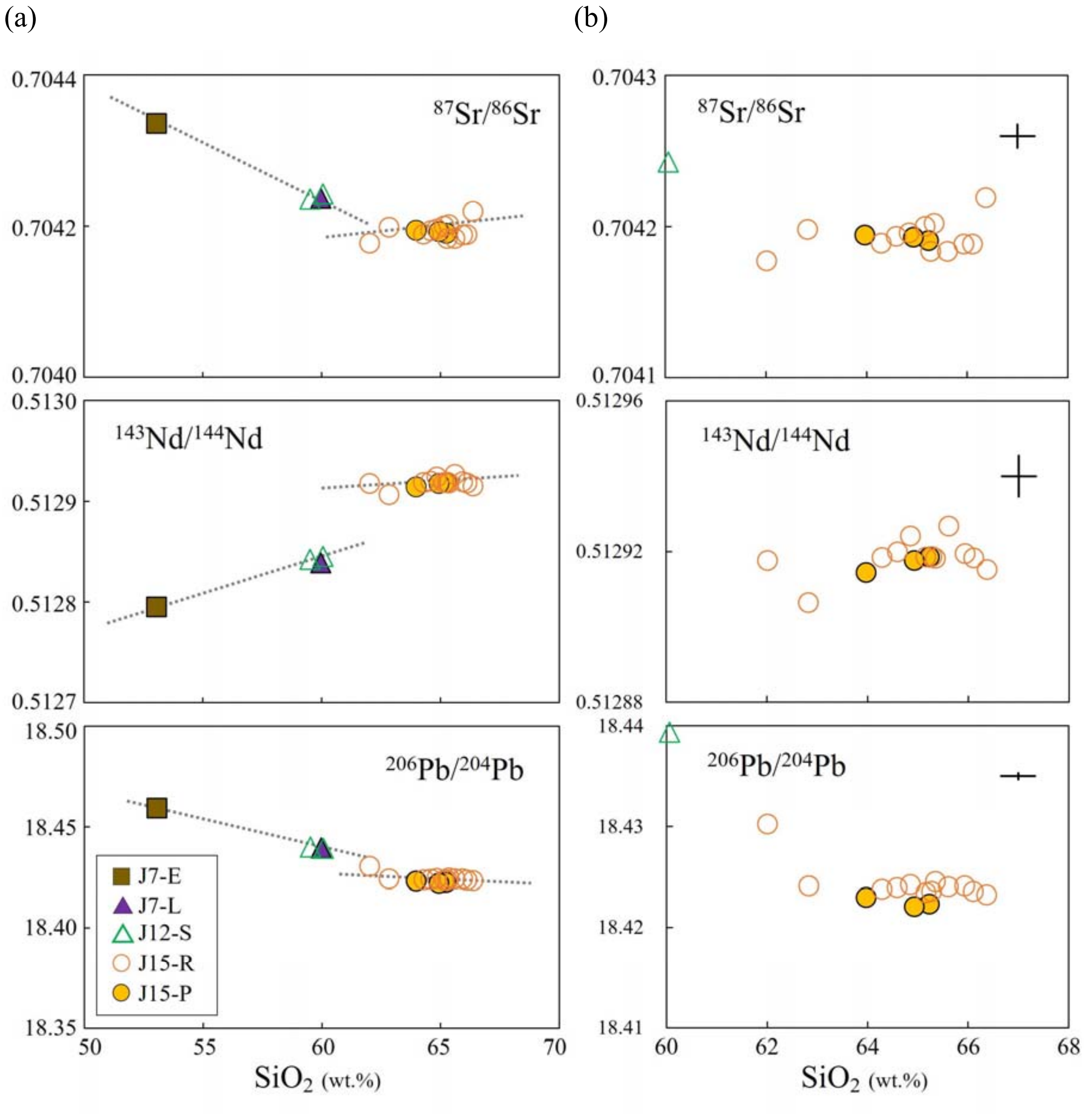

Fig. 9. Sr-Nd-Pb isotopic compositional variations of 1991 Pinatubo samples. (a) Dotted lines show approximately linear fits to the basalt and andesite samples and to the dacite samples only. (b) These figures focus on the composition of dacite. The vertical and horizonal bars show the analytical error.

Table 2. Whole-rock major (wt.%) and trace (ppm) elements and isotopic compositions of representative 1991 samples.

Unit	J7-E	J7-L	J12-S	J15-R	J15-R	J15-R	J15-R	J15-P
Sample name	P22892-1A	CN6791-D	P22892-3	120801C-O	121202C-H	120801MP-d	121202C-B1	121202C-C
SiO_2	53.08	59.89	59.63	62.05	65.23	63.77	66.72	65.38
TiO_2	0.90	0.67	0.67	0.65	0.57	0.55	0.50	0.51
Al_2O_3	14.85	15.91	15.64	16.46	16.20	16.51	16.24	16.85
$Fe_2O_3^{t*1}$	8.78	6.26	6.29	5.58	4.81	4.64	4.18	4.23
MnO	0.16	0.13	0.13	0.12	0.11	0.11	0.10	0.10
MgO	8.44	4.83	4.82	3.69	2.51	2.56	2.27	2.24
CaO	9.70	7.05	7.04	6.20	4.95	5.33	4.65	5.04
Na_2O	3.19	3.94	3.91	4.31	4.45	4.53	4.48	4.65
K_2O	1.53	1.57	1.54	1.35	1.53	1.47	1.62	1.48
P_2O_5	0.31	0.25	0.25	0.2	0.22	0.19	0.18	0.18
Total	100.04	99.87	99.30	100.06	100.11	99.66	100.94	100.23
V	243	166	165	148	120	116	103	103
Cr	313	154	150	129	46	48	38	43
Co	33	23	23	20	16	15	14	13
Ni	101	52	51	39	20	20	18	17
Rb	46	48	44	36	43	39	47	41
Sr	561	572	559	571	539	573	541	577
Y	19	16	18	17	16	16	14	16
Zr	99	111	108	116	126	116	117	118
Nb	1.3	2.1	2.3	2.5	3.5	2.7	3.5	2.5
Ba	343	420	421	435	482	462	512	472
La	22.2	18.8	18.3	14.9	16.1	14.9	15.2	15.0
Ce	47.2	38.4	37.7	30.1	32.3	30.1	30.3	29.5
Nd	24.8	18.9	18.9	15.0	15.5	14.6	13.8	13.7
Sm	5.37	3.98	3.98	3.22	3.17	3.02	2.77	2.79
Eu	1.48	1.05	1.07	0.91	0.83	0.81	0.73	0.79
Gd	4.67	3.49	3.51	2.96	2.86	2.76	2.51	2.48
Tb	0.64	0.49	0.50	0.43	0.42	0.41	0.36	0.37
Dy	3.41	2.69	2.72	2.55	2.39	2.34	2.09	2.09
Ho	0.67	0.54	0.55	0.52	0.49	0.48	0.43	0.43
Er	1.83	1.50	1.51	1.47	1.40	1.34	1.22	1.22
Tm	0.26	0.23	0.22	0.22	0.21	0.21	0.19	0.19
Yb	1.67	1.44	1.46	1.38	1.35	1.31	1.20	1.23
Lu	0.25	0.22	0.23	0.21	0.22	0.23	0.19	0.20

(continued)

Unit	J7-E	J7-L	J12-S	J15-R	J15-R	J15-R	J15-R	J15-P
Sample name	P22892-1A	CN6791-D	P22892-3	120801C-O	121202C-H	120801MP-d	121202C-B1	121202C-C
$^{87}Sr/^{86}Sr$*2	0.704335	0.704237	0.704243	0.704177	0.704200	0.704189	0.704219	0.704191
$^{143}Nd/^{144}Nd$	0.512795	0.512839	0.512845	0.512918	0.512919	0.512918	0.512915	0.512919
$^{206}Pb/^{204}Pb$	18.4593	18.4395	18.4394	18.4302	18.4234	18.4238	18.4232	18.4223
$^{207}Pb/^{204}Pb$	15.6005	15.5938	15.5948	15.5913	15.5901	15.5899	15.5897	15.5899
$^{208}Pb/^{204}Pb$	38.6501	38.6161	38.6199	38.6049	38.5953	38.5949	38.5940	38.5932

V-Ba and La-Lu were analyzed by XRF and ICP-MS, respectively.

*1 Total Fe expressed as $Fe_2O_3^t$. In Harker diagrams (Fig. 7), total Fe is expressed as $FeO^t = FeO + 0.8998Fe_2O_3$ and normalized to 100%.

*2 Maximum standard errors are 0.000008 for Sr, 0.000005 for Nd, 0.0003 for ^{206}Pb and ^{207}Pb, and 0.0008 for ^{208}Pb.

Chapter 6: Discussions

6.1. Magma mixing and the end-member magmas recorded in the 1991 eruptive rocks

Previous studies have suggested that the paroxysmal eruption of the 1991 Pinatubo activity on 15 June was triggered by an injection of basaltic magma into the voluminous dacitic magma chamber, attributing the andesitic scoria emitted during the preceding eruption on 12 June to the magma mixing of basaltic and dacitic magmas (e.g., Pallister et al., 1996; Bernard et al., 1996). Our new whole-rock and mineral chemistry dataset supports that conclusion: The andesite samples from both 7 and 12 June plot along mixing lines between the basaltic enclave and the 15 June dacite in whole-rock (Fig. 7) and Sr-Nd-Pb isotope silica variation diagrams (Fig. 9).

Here, based on the compositional distribution of phenocrystic minerals in the juvenile products of the 1991 eruption (Fig. 3), we discuss the phenocryst assemblages and mineral chemistries of the end-member basaltic and dacitic magmas. Plagioclase and amphibole phenocrysts in the dacitic samples show nearly unimodal compositional distributions with peaks that match those of the andesitic rocks (Fig. 3). Thus, as the most silicic magma observed, the dacitic magma erupted on 15 June can be identified as one of the two end-member magmas. In both the phenocryst-rich and phenocryst-poor dacitic rocks, plagioclase phenocrysts with lower An# (<50) and hornblende phenocrysts with higher Si (>6.7 pfu) dominate (Fig. 3). In addition, the dacitic magma contains titano-magnetite phenocrysts with Mg/Mn = 4-5, which, according to their Mg/Mn ratios, are in equilibrium with coexisting ilmenite (Bacon and Hirschmann, 1988). Moreover, quartz phenocrysts are dominant in the dacitic rocks and do not show corona structures as observed in the basaltic sample. Thus, quartz was a phenocrystic minerals in the dacitic end-member magma. Considering these petrographical features, we estimate the phenocryst assemblage of the dacitic end-member magma to have been less calcic plagioclase + hornblende + quartz + titano-magnetite + ilmenite ± minor biotite.

In contrast, the basaltic and andesitic samples contain magnesian olivine phenocrysts (up to Mg# = 90, Fig. 3), which are representative of primitive basaltic magmas (Bernard et al., 1996; Pallister et al., 1996). In these samples, olivine always occurs as an isolated phenocryst; the basaltic end-member magma must therefore have contained olivine phenocrysts.

However, the basaltic and andesitic samples include other, less-silicic phenocryst phases, such as clinopyroxene and pargasite, that are absent in the dacitic end-member magma.

Although clinopyroxene phenocrysts in the basalt are relatively magnesian (Mg# = 78-88, Fig. 3), the Fe-Mg distribution coefficient between olivine and clinopyroxene (Obata et al., 1974) dictates that these phenocrysts could not have coexisted with magnesian olivine phenocrysts. Thus, the basaltic and andesitic samples must be the product of magma mixing, and their phenocrysts assemblages, including clinopyroxene, must represent minerals crystallized after the basaltic and dacitic end-member magmas mixed. In addition, because pargasite reaction rims around olivine have similar compositions to pargasite phenocrysts (Fig. 2h), it seems that pargasite phenocrysts also crystallized from the mixed magma (Coombs and Gardner, 2004; Kiss et al., 2014). Moreover, calcic plagioclase phenocrysts (An# >80) are common in the basalt sample (Fig. 3). These plagioclase phenocrysts must also be derived from the mixed magma, because magnesian olivine phenocrysts do not form crystal clots with plagioclase. Thus, we conclude that the phenocryst assemblage of the basaltic end-member magma included solely olivine.

6.2. Diversity of the dacite end-member magma

Although previous studies have reported the whole-rock chemical compositions of the dacitic samples (Daag et al., 1996; Pallister et al, 1996; Bernard et al., 1996; Hattori and Sato, 1996; Castillo and Punongbayan, 1996; Fournelle et al., 1996; Luhr and Melson, 1996), chemical variations among the dacitic samples have not been discussed. However, our new dataset clarifies possible geochemical and petrographical variations in the dacite.

The 15 June dacitic samples clearly form a linear compositional trend in silica variation diagrams of major and trace element and Sr-Nd-Pb isotope. However, these trends do not extrapolate toward the andesitic and basaltic rocks in almost all diagrams (Figs. 7, 9). Therefore, the compositional variations of the dacitic magma cannot be attributed to the injection of the basaltic magma into the dacitic end-member magma; it seems that the variations in the dacitic magma existed prior to the basaltic injection. We thus conclude that the dacitic magma, into which the basaltic magma was injected, was heterogeneous.

Although the amount of phenocryst in phenocryst-rich and phenocryst-poor pumice varies greatly (Table 1), the whole rock compositions of them are similar (Figs. 7, 9; Table 2). Figure 10 shows the relationship between the amount of phenocryst and the whole rock compositions of 1991 samples. The whole rock composition of each pumice does not increase or decrease with the amount of phenocryst, plagioclase and amphibole (mainly hornblende) contents, whereas it shows a scattered distribution. In other words, there is no correlation between the amount of phenocryst and the whole rock composition. Therefore, the heterogeneity of dacitic magma is could not formed by the difference of the amount of phenocryst.

The compositional distributions of plagioclase and amphibole in the 1991 heterogeneous dacitic magma are nearly unimodal, and dominantly comprise phenocrysts with An# = 30-50 and 7.1-6.6 Si pfu, respectively (Fig. 3). However, many plagioclase and hornblende phenocrysts with higher An# (>40) and lower Si (<6.7 pfu) cores, respectively, are normally zoned, whereas those with lower An# and higher Si cores, respectively, mostly show reverse zonations (Figs. 4, 6). Figure 11 shows representative zoning profiles of plagioclase phenocrysts in the June 15 dacite. The phenocryst in Figure 11a has a core that is normally zoned from An# ≈ 50 at the center of the core to An# ≈ 30 at the core-rim boundary, whereas that in Figure 10b has a core that is reversely zoned from An# ≈ 30 at the core center to An# ≈ 50 at the core-rim boundary. Father towards their outer rims, both phenocrysts change chemical compositions to be An# = 30-50. These features can be explained by the mixing of two end-member magmas: A hotter, less silicic magma containing plagioclase phenocrysts with An# ≈ 50 cores, and a cooler, more silicic magma containing plagioclase phenocrysts with An# ≈ 30 cores. The zonal structure of these phenocrysts indicates that their outer rims grew to have compositions corresponding to the mixed magma (Fig. 11). Thus, there was sufficient time for the outer rims to grow to considerable thickness after mixing occurred.

Combined with the liner compositional variations of the dacitic samples in silica variation diagrams, these two populations of zoned plagioclase and hornblende phenocrysts strongly indicate that the 1991 heterogeneous dacite was the product of the mixing of at least two silicic end-member magmas prior to the injection of the 1991 basaltic magma.

6.3. Magmatic temperature of the silicic end-member magmas

Previous studies calculated the magmatic temperature of the 1991 dacite using the compositions of coexisting Ti-magnetite and ilmenite phenocrysts (Pallister et al., 1996; Rutherford and Devine, 1996). However, based on our above results, those estimates reflect the temperature of the product of mixing of at least two silicic end-member magmas. Thus, we here estimate magmatic temperature and storage depth of the two silicic end-member magmas.

Based on the normally and reversely zoned plagioclase and hornblende phenocryst populations (see section 6.2), we can estimate the chemical compositions of plagioclase and hornblende phenocrysts in each silicic end-member magma; we can then estimate magmatic temperatures of both magmas from plagioclase-amphibole pairs showing the same zonation by using the method of plagioclase-amphibole thermometer (Holland and Blundy, 1994). We calculated magmatic temperatures by using the average chemical compositions of three types of plagioclase-hornblende pairs: normally (An# = 43.7-52.8, Si = 6.59-6.74 pfu), reversely (An# = 32.0-33.9, Si = 6.82-7.04 pfu), and weakly zoned pairs (An# = 34.4-35.8, Si = 6.80-6.94 pfu). Moreover, we estimated the storage pressures of these pairs based on the average hornblende compositions by the method of Mutch et al. (2016) (Table 3). We obtained temperatures and pressures of 765-807 ˚C and 293-352MPa, 694-722 ˚C and 199-273 MPa, and 708-735 ˚C and 245-287 MPa for the normally, reversely, and weakly zoned pairs, respectively (Fig. 12). Both the temperature and pressure of the normally zoned pairs are greater than those of the reversely zoned pairs, which are similar to those of the weakly zoned pairs.

6.4. Origin of the 1991 heterogeneous dacitic magma

The origin of the 1991 Pinatubo dacitic magma has been extensively discussed (Bernard et al. 1996; Rutherford and Devine, 1996; Scaillet and Evans, 1999; Prouteau and Scaillet, 2003). Bernard et al. (1996) concluded that the interaction of a basaltic magma that stagnated in the crust with surrounding crustal materials formed the 1991 Pinatubo dacite, which can be classified as the partial melting of lower crustal materials. In contrast, Prouteau and Scaillet (2003) rejected the partial melting of crustal materials on the basis of melting experiments and proposed that the dacite was formed by high pressure fractionation of a basaltic magma. In this section, based on our new data, we discuss the origin of the 1991 heterogeneous dacitic magma.

Bernard et al. (1996) suggested that the 1991 Pinatubo dacite could not have been produced by the fractional crystallization of a coexisting basaltic magma. Our new data supports their conclusion: the K_2O and Rb contents of both the basaltic and dacitic magmas are similar, regardless of their incompatible element contents (Fig. 7). In addition, the REE contents of the basaltic enclave are higher than those of the dacitic samples (Fig. 8) and the Sr-Nd-Pb isotopic compositions of the basalt and dacite samples are distinct (Fig. 9). Thus, the silicic end-member magmas of the 1991 dacitic magma could not have been generated by the fractional crystallization of the basaltic magma related to the 1991 eruption.

We also consider the possibility that the previous basaltic magma erupted at Pinatubo volcano (the Buag period basalt) could have produced the dacitic magma. The K_2O and Rb contents of the Buag period basalt (Muro et al., 2008) are lower than those of the 1991 dacites (Fig. 7), which might suggest that the 1991 silicic end-member magmas resulted from the fractional crystallization of the Buag period basaltic magma. However, the REE patterns of the Buag basalt show gentler slopes than those of the 1991 dacite samples and intersect those of the dacites between Ce and Nd (Fig. 8), indicating that the dacite samples could not have been produced by the fractional crystallization of the Buag basalt. Therefore, the 1991 heterogeneous dacitic magma must have an origin distinct from that of basaltic magmas at Pinatubo, suggesting that it was produced by the partial melting of crustal materials.

In contrast, Prouteau and Scaillet (2003) compiled experimental metabasaltic melts and indicated that they are inconsistent with the chemical compositions of the 1991 Pinatubo dacite. However, they compared the experimental melts with the whole-rock chemistry of the dacite, which contains phenocrystic minerals. The chemical compositions of matrix glasses in 1991 Pinatubo dacitic pumices are similar to those of experimental melts produced by dehydration and/or water-saturated melting at 100-1,000 MPa (Beard and Lofgren, 1991; Rapp et al., 1991; Wolf and Wyllie, 1994) (Fig. 13, Table 4). The Al_2O_3 contents of the experimental melts increase with decreasing SiO_2 content as the melting temperature and/or H_2O content of the crustal materials increase (Winther, 1996). Moreover, the pressure of melting increases with increasing Al_2O_3 content (Fig. 13) to 800-1,000 MPa, corresponding to 30-50 km depth, the maximum crustal thickness reported on Luzon Island (Wu, 1979; Mooney et al., 1998). Thus, the partial melting of crustal materials at various depths could have generated the 1991 heterogeneous Pinatubo dacite.

Because the 1991 heterogeneous dacite is the product of mixing between at least two silicic end-member magmas (see section 6.2), we here investigate their compositional relationship. Although their chemical compositions might be estimated by extrapolating the linear trends of the 1991 dacitic samples in silica variation diagrams (Figs. 7, 9), it is difficult to determine the chemical compositions without making unreasonable assumptions, because the chemical compositions of their phenocrystic minerals are similar (Figs. 4, 6). Thus, to discuss the origin of these silicic magmas, we assumed two silicic end-member magmas: ‘D1’, the least silicic magma observed (63.97 wt.% SiO_2), and ‘D2’, the most silicic (66.37 wt.% SiO_2; Fig. 14). We calculated other major and trace element contents of the D1 and D2 magmas from the approximately linear relation in the SiO_2 variation diagrams (Table 5).

We investigated whether the more silicic D2 magma could be produced by fractional crystallization of the less silicic D1 magma. We performed a major element mass balance calculations (Tsune, 2005) by choosing the average composition of plagioclase, amphibole and titano-magnetite, contained in the dacite. We obtained relative proportions of melt and minerals by best fit, with the sum of square of residuals (SSR) = 0.05 and the root mean square of residuals (RMSR) = 0.07, sufficiently small compared to the recommendation of Tsune (2005), i.e., SSR < 1 and RMSR < 0.5. We obtained plagioclase: amphibole: magnetite proportion of 62:36:2, which differs from the modal proportions obtained by point counting. Then, based on the mineral proportions determined by mass balance and using bulk partition coefficients, we used the Rayleigh fractional crystallization model to determine the end-member trace element contents (Fig. 15). We used the mineral-melt partition coefficients of Matsumoto and Nakagawa (2010) for all trace elements, because they studied similar silicic magma. Although the fractional crystallization of the D1 magma can explain the observed variation of the Y/Rb ratio of the dacite samples and the estimated silicic end-member magmas, it cannot explain the observed variations of the Zr/Rb and Ba/Rb ratios, indicating that the D2 magma cannot be derived from the D1 magma.

Our model calculation thus suggests that the two silicic end-member magmas are not genetically related. Thus, it is plausible that crustal melting separately but simultaneously produced at least two silicic end-member magmas (e.g., Feeley et al., 1998; Hansen et al., 2002; Toya et al., 2005). Matsumoto and Nakagawa (2010) proposed that the partial melting of crustal materials could generate heterogeneous silicic melts. They assumed that mafic magmas might underplate the lower crust, modifying the crustal materials. In the case of crustal melting due to a single heat source, the temperature shows a logarithmic decreasing with distance from the thermal source (Hanson, 1992). Because of this thermal gradient, the hotter regions are limited to the crustal materials near the thermal source, resulting to the formation of smaller amounts of partial melts with higher degree of partial melting. In contrast, the wider and cooler regions far from the thermal source could produce larger amounts of partial melts with lower degrees of partial melting (Matsumoto and Nakagawa, 2010). If above process applies to the 1991 dacitic magma, higher degree of partial melting causes the small amounts of melt (= D1) at near boundary of heat source, whereas lower degree of melting does the large amounts of melt (= D2) at far distance from boundary. Moreover, distinct silicic melts might be also produced by partial melting of heterogeneous crustal materials. This speculated process might occur beneath Pinatubo volcano.

The calculated temperatures and pressures of the normally and reversely zoned mineral pairs differ beyond errors, suggesting that the magmatic temperatures and depths of the silicic end-member magmas were distinct. That is, silicic magmas with variable temperatures and accumulated at different depths and subsequently mixed to form the hybrid silicic magma. We consider that the cooler, more silicic magma stagnated at the shallower crust, whereas the hotter, less silicic magma stagnated at deeper level. According to our calculated depths, the deeper silicic magmas ascended must have ascended to mix with the shallower ones, forming the 1991 heterogeneous dacitic magma at approximately the storage depth of the more silicic end-member magmas.

6.5. Formation and evolution of magma plumbing model in 1991 eruption

Based on our new analysis of juvenile materials of the 1991 Pinatubo eruption, we conceptualize the pre-eruptive processes as follows (Fig. 16).

(1) Partial melting of crustal materials by basaltic magmas. After the Buag period (~1.0-0.5 ka), a basaltic magma distinct from the Buag basalt ascended and stagnated beneath the lower crust. This magma heated the overlying crustal materials, forming zones of silicic mush (Fig. 16a).

(2) The formation of heterogeneous silicic end-member magmas. By melting heterogeneous crustal materials under thermal gradient, heterogeneous silicic melts with variable chemical compositions and magmatic temperatures were produced at various depths and accumulated into melt lenses to form a crystal mush chamber. The melt lenses grew into magma pockets and/or chambers in the mush (Fig. 16b). In general, cooler, more silicic magmas accumulated at shallower depths within the mush, and hotter, less silicic magmas at greater depths.

(3) The formation of a large, silicic magma chamber. Small magma pockets in the mush zone were gradually extracted and ascended through the mush, accumulating to form a large silicic magma chamber in the upper part of the mush zone (Hildreth and Wilson, 2007), eventually developing into the 1991 silicic magma chamber (Fig. 16c). Our new dataset of the 1991 dacite suggests that the formation of a large chamber can be considered as a mixing process between at least two silicic end-member magmas (Fig. 16d), such as D1 and D2 in Figure 14. This large, hybrid magma chamber was situated between 6 and 14 km depth according to geophysical investigations (Mori et al., 1996; White, 1996) and

previous petrological studies (Rutherford and Devine, 1996; Pallister et al., 1996; Hammer and Rutherford, 2003). Moreover, it is estimated that uneruptable materials at 4-6 km depth (Rutherford and Devine, 1996; Hammer and Rutherford, 2003) correspond to the top of the mush zone (Fig. 16d).

(4) Triggering of the 1991 eruption (Pallister et al., 1992, 1996). Just prior to the 1991 eruption, the 1991 basaltic magma was injected into the dacitic magma chamber. This generated the andesitic magma, which ascended and was extruded as the lava dome on June 7, which, in turn, was destroyed by the Plinian eruption on June 12 (Fig. 16e). Finally, the 1991 dacitic magma occupying the chamber was erupted during the June 15 climactic eruption.

Previous studies of the 1991 Pinatubo eruption have focused on the processes that triggered the explosive eruptions, such as the injection of the basaltic magma into the voluminous silicic magma chamber (Pallisters et al., 1992; Pallister et al., 1996). This process is recognized as evidence of mixing and mingling between the basaltic and silicic magmas. Our results reveal that the formation and evolution of the silicic magma chambers was recorded by phenocrystic minerals in the silicic eruptive materials, and further investigation of the zonal structures of those phenocrystic minerals could constrain the timescale of pre-eruptive processes of the 1991 Pinatubo eruption. However, we cannot confirm the detailed genesis of the 1991 dacitic magma because whole rock compositions from past eruptive periods at Pinatubo (Buag, Maraunot, etc.) are limited (Muro et al., 2008), although the whole rock compositions of the 1991 and Buag period dacitic magmas are similar. Thus, we speculate that the generation of silicic end-member magmas, like the D1 and D2 magmas in this study, has occurred repeatedly in the Pinatubo magma plumbing system. In contrast, the 1991 basalt is distinct from the Buag basalt (Figs. 7, 8), suggesting that voluminous silicic eruptions at Pinatubo are controlled by the formation of basaltic magmas in the mantle wedge beneath the volcano. Although our study revealed the formation and evolution of the magma plumbing system during at most the 500 years following the Buag period, the long-term (since 40 ka) evolution of the modern Pinatubo stage (Newhall et al., 1996) has not yet been revealed. Considering the similarity of the whole rock compositions produced during each huge eruption, it should be possible to determine the long-term (i.e., several thousand to ten thousand years) formation and evolution of the magma plumbing system based on geochemical research. To this end, it is essential to reveal all possible variations among the silicic magmas, as shown in this study.

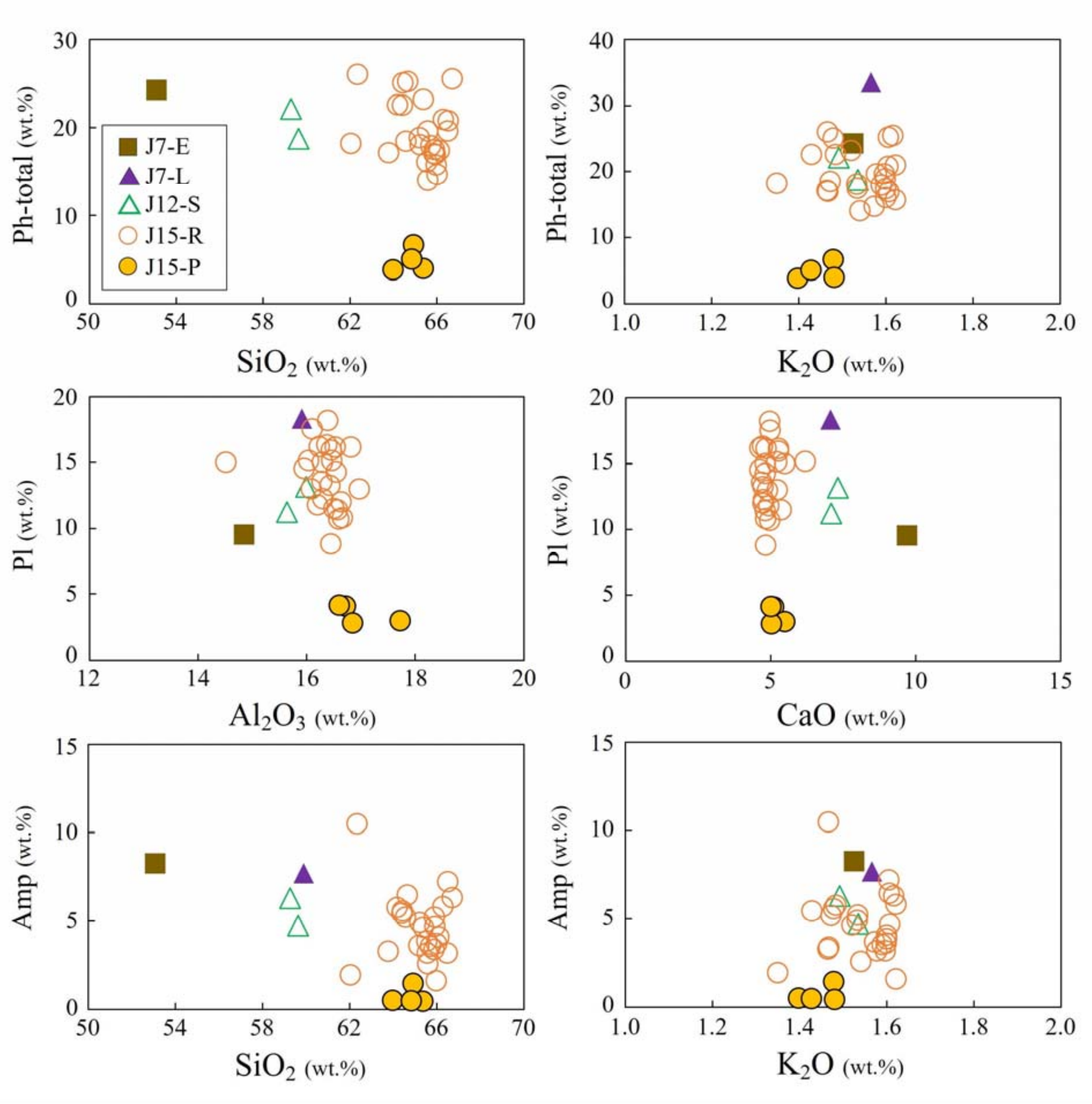

Fig. 10. Relationship between the amount of phenocryst contents (wt.%) and bulk compositions (wt.%) of 1991 samples. The amount of phenocryst content includes total phenocryst (Ph-total), plagioclase (Pl) and amphibole (Amp).

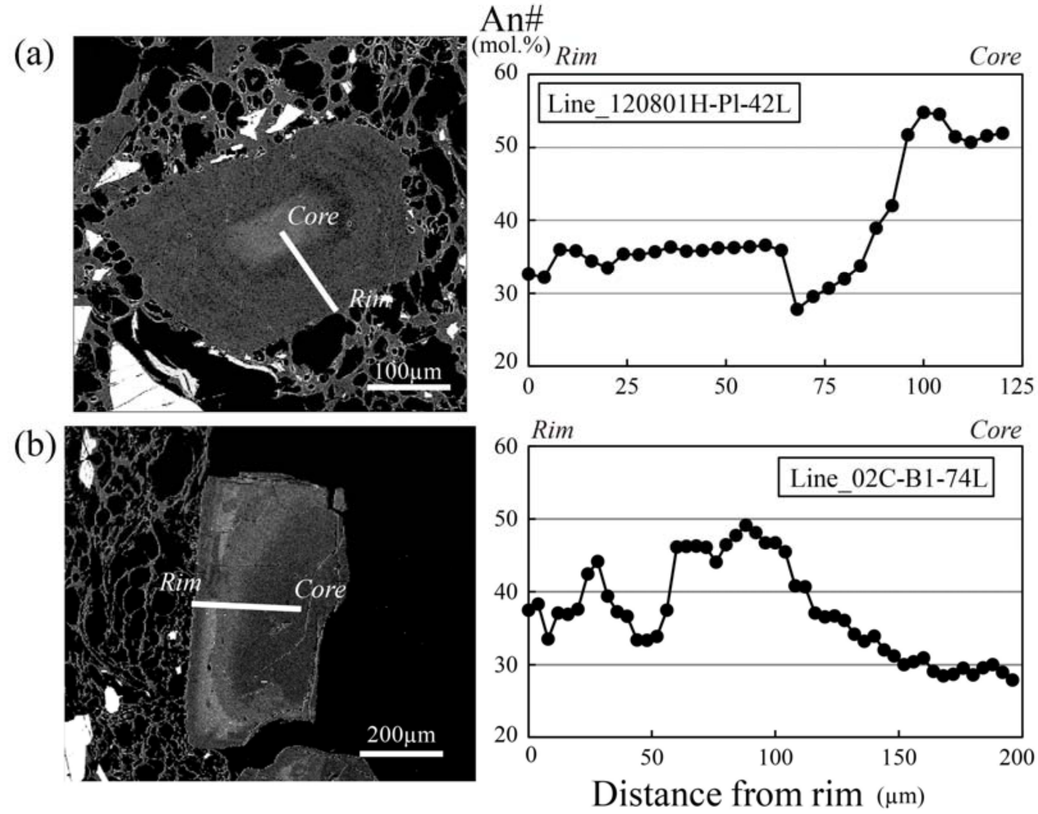

Fig. 11. Representative zoning profiles of plagioclase phenocrysts in dacitic samples. Plagioclase phenocrysts with cores having An# ≈ 50 are normally zoned, reaching An# ≈ 30 at the core-rim boundary (a), whereas those with cores having An# ≈ 30 exhibit reverse zonations, reaching An# ≈ 50 at the core-rim boundary (b).

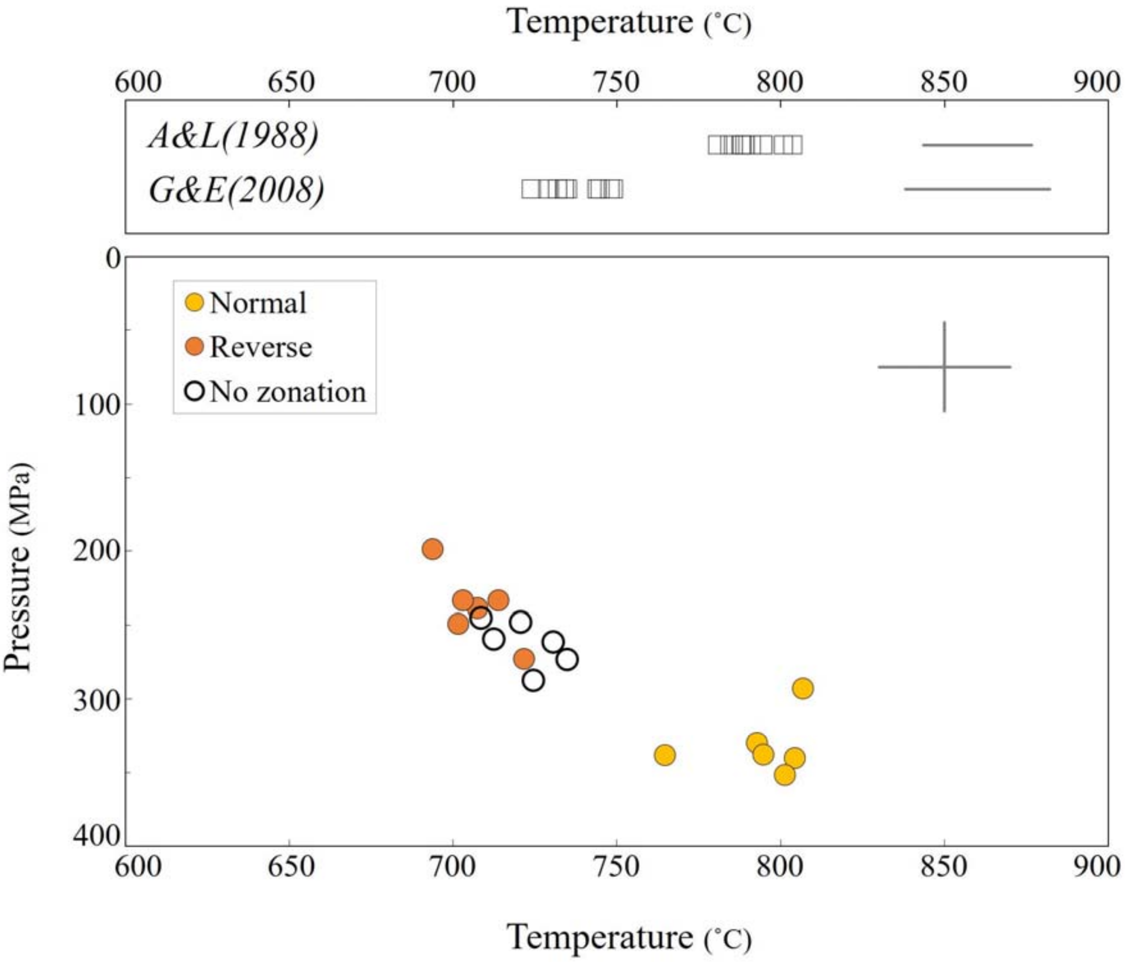

Fig. 12. Magmatic temperatures calculated for the 1991 dacitic magma. (top) Temperatures obtained using the magnetite-ilmenite geothermometer by Andersen and Lindsley (1988) and Ghiorso and Evans (2008). The original temperatures of Andersen and Lindsley (1988) are lowered by 30 ˚C in accordance with Geschwind and Rutherford (1992). The average absolute deviations (aad) of Andersen and Lindsley (1988), and Ghiorso and Evans (2008) are ±33 ˚C and ±44 ˚C, respectively (gray bars). (bottom) Magmatic temperatures calculated on our sample using the plagioclase-amphibole (Thermometer B; add ±40˚; gray horizon bar) of Holland and Blundy (1994). We used the average chemical compositions of plagioclase-hornblende pairs showing normal, reverse, or weak zoning (see Table 3). Pressure values were calculated by Mutch et al. (2016; aad±60 MPa, gray vertical bar).

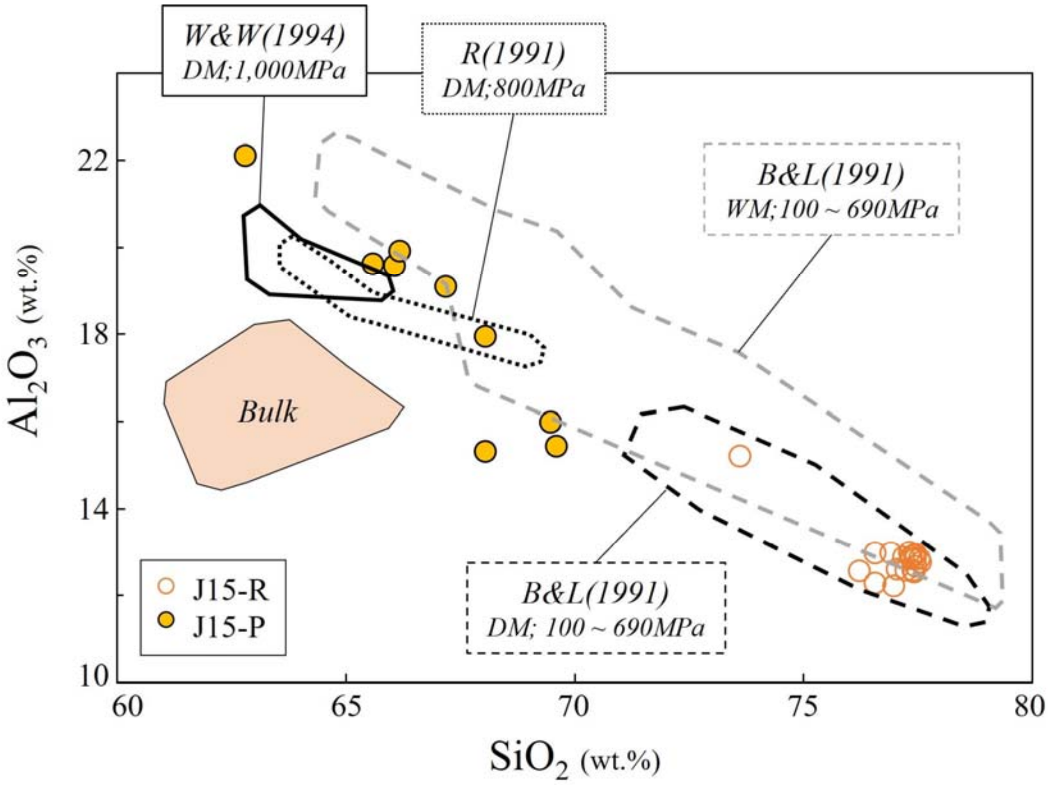

Fig. 13. Comparison of matrix glass compositions in dacitic pumices with experimental melts obtained by the dehydration melting (DM) or water-saturated melting (WM) of crustal materials. Black and gray dashed polygons outline the results for dehydration and water-saturated melting experiments, respectively, at 100-690 MPa (Beard and Lofgren, 1991). Black dotted and solid polygons outline the results of dehydration melting experiments at 800 MPa (Rapp et al., 1991) and 1,000 MPa (Wolf and Wyllie, 1994), respectively. Gray filled and black open circles show the matrix glass compositions of phenocryst-poor (J15-P) and -rich (J15-R) pumices, respectively. The gray shaded area outlines the bulk composition of dacitic pumices.

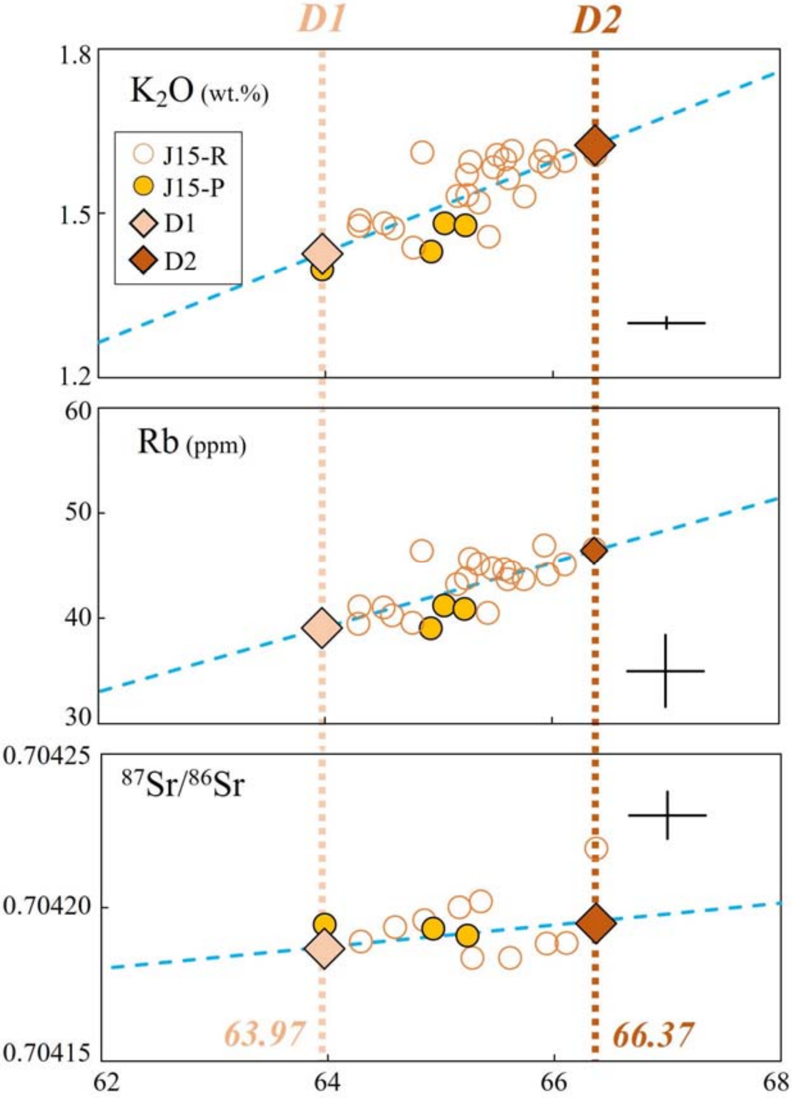

Fig. 14. Representative whole-rock major, trace and isotopic compositions of the 1991 dacites and two silicic end-member magmas. We assumed two end-member magmas with SiO_2 contents taken as the extreme values of the observed dacites: D1, the less silicic magma (63.97 wt.% SiO_2, left diamond and dotted line), and D2, the more silicic magma (66.37 wt.% SiO_2, right diamond and dotted line). The other elemental isotopic compositions of the end-member magmas were calculated from linear fits to the observed data (blue dashed lines). The vertical and horizonal bars show the analytical error.

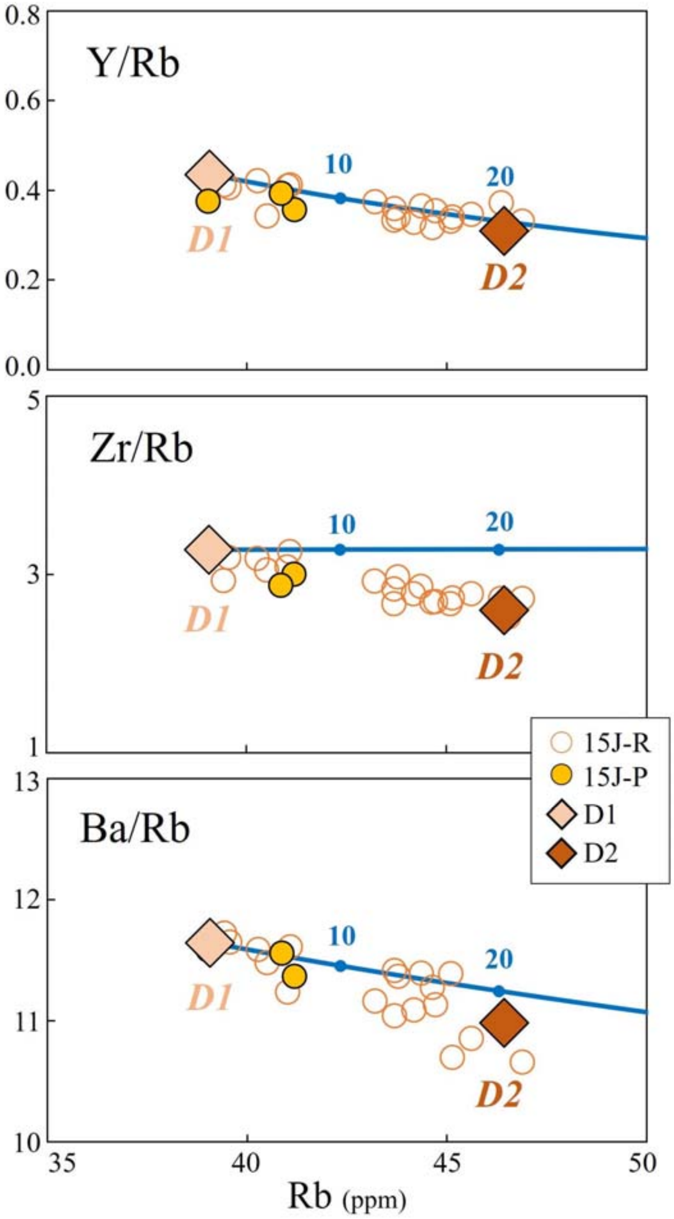

Fig. 15. Rb concentrations and Rb-normalized trace element contents of 1991 dacites and the D1 and D2 end-member magmas. Gray lines show the results of a Rayleigh fractional crystallization model calculated based on the mineral proportion in the D1 and D2 magmas (determined by mass balance between the two magmas, see section 6.4). Numerical values along the gray lines show the proportion of fractional crystallization. The end-member D2 magma does not plot along the fractional crystallization trend, and thus could not have been generated by the fractional crystallization of the D1 magma.

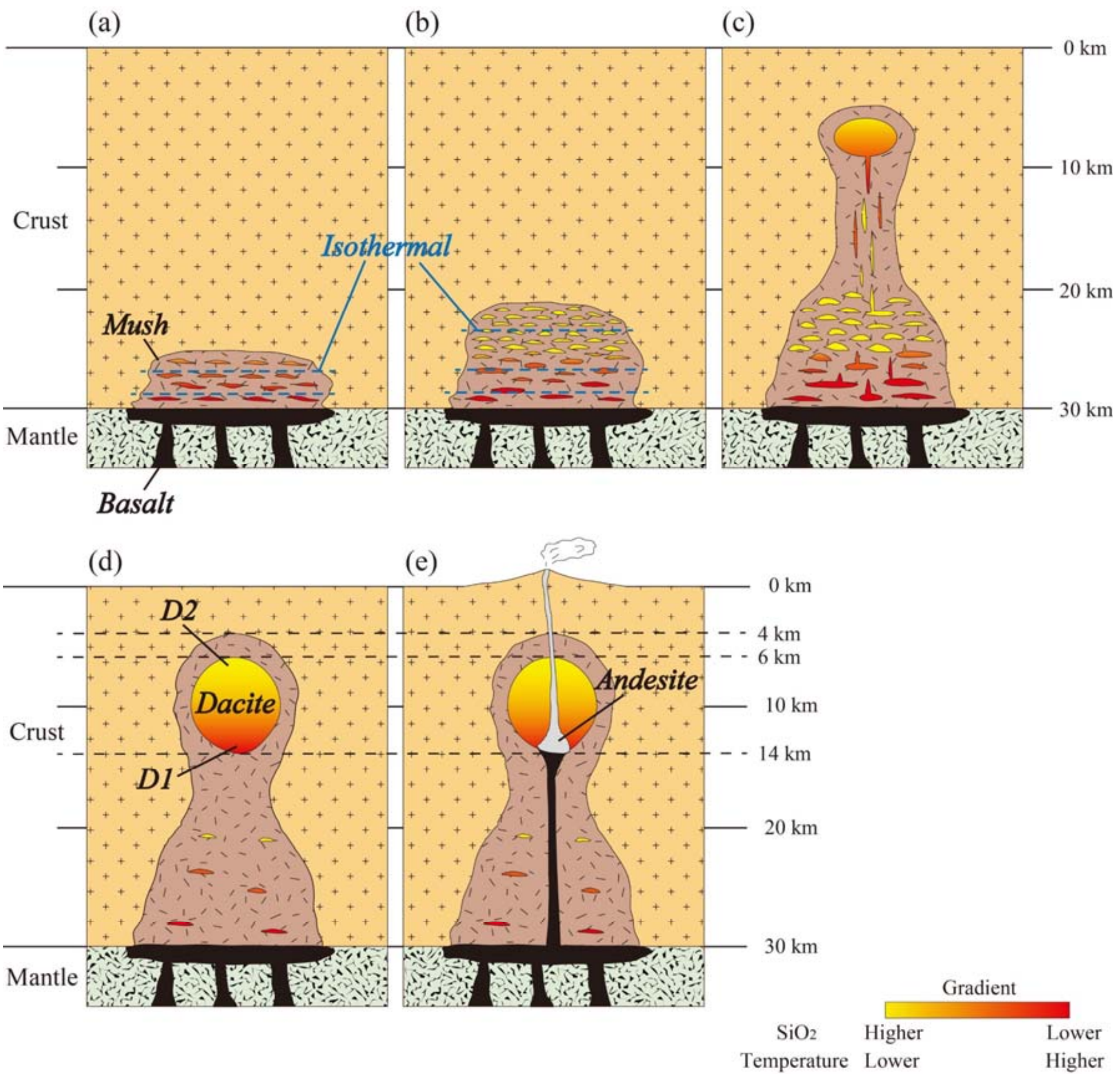

Fig. 16. Schematic representation of the magma plumbing system of the 1991 Pinatubo eruption.: (a) Partial melting of crustal materials due to basaltic magma underplating. New basaltic magma ascended and stagnated beneath the lower crust, heating the crustal materials and forming silicic melt lenses. Dashed blue lines show isothermal contours. Cooler, more silicic melt lenses formed at shallower depths within the crystal mush, whereas hotter,less silicic ones formed at greater depths. (b) The formation of heterogeneous silicic end-member magmas. Due to the heterogeneity of crustal materials and the thermal gradient, heterogeneous silicic melts were produced. Smaller melt lenses grew to form small magma pockets and/or chambers within the mush. (c) The formation of a large silicic magma chamber. The gradual extraction, ascent, and accumulation of smaller magma pockets formed a large magma chamber at shallower depths within the crystal mush zone. (d) Continued magma extraction, ascent, and accumulation formed the hybrid 1991 silicic magma chamber, which is considered as magma mixing of at least two silicic end-member magmas, such as D1 and D2. (e) Triggering of the 1991 eruption. Just before the 1991 eruption, basaltic magma injected into 1991 dacitic magma chamber to produce andesitic magma that was extruded as a lava dome on June 7. The dome was subsequently destroyed by the June 12 Plinian eruption.

Table 3. Magmatic temperature (°C) of the 1991 dacitic magma (major element concentrations in wt.%; n.d., not detected) based on plagioclase-amphibole geothermomter.

Zonation type	Normal zoning		Normal zoning		Reverse zoning		Reverse zoning		No zonation		No zonation	
Phenocryst	Plagioclase	Hornblende	Plagioclase	Hornblende	Plagioclase	Hornblende	Plagioclase	Hornblende	Plagioclase	Hornblende	Plagioclase	Hornblende
Sample name	121202C-B1		121202C-C		121202C-B1		121202C-C		121202C-B1		121202C-C	
Point	Core	Core	Core	Core	Core	Core	Core	Core	Core	Core	Core	Core
SiO_2	55.08	47.76	56.16	46.40	61.12	50.39	60.25	48.34	59.89	48.62	59.58	48.30
TiO_2	-	1.00	-	1.34	-	0.78	-	0.84	-	0.91	-	0.95
Al_2O_3	27.98	8.34	27.29	9.34	24.59	6.39	24.69	7.95	25.11	7.74	25.12	7.98
FeO^{t*1}	0.17	13.19	0.16	12.56	0.15	11.59	0.15	13.07	0.15	12.84	0.15	13.05
MnO	-	0.52	-	0.44	-	0.47	-	0.57	-	0.54	-	0.54
MgO	0.01	14.92	0.01	14.90	0.01	16.42	0.01	15.03	0.01	15.33	0.01	15.15
CaO	10.95	10.78	9.97	10.83	6.74	10.98	6.88	10.74	7.48	10.65	7.34	10.72
Na_2O	5.29	1.44	6.00	1.66	7.57	1.15	7.59	1.42	7.20	1.37	7.40	1.41
K_2O	0.18	0.34	0.22	0.35	0.38	0.23	0.38	0.34	0.33	0.29	0.34	0.32
Total	99.65	98.28	99.81	97.83	100.55	98.39	99.95	98.30	100.16	98.28	99.93	98.40
$An\#^{*2}$	52.8	-	47.4	-	32.3	-	32.7	-	35.8	-	34.7	-
Si^{*3}	-	6.74	-	6.59	-	7.04	-	6.82	-	6.83	-	6.80
Al^{t*3}	-	1.41	-	1.33	-	0.87	-	1.10	-	1.07	-	1.34
T^{*4}	807		801		694		722		731		735	
P^{*5}	-	293	-	352	-	199	-	273	-	261	-	273

[*1] Total Fe is expressed as FeO^t.

[*2] An# is reported in mol.%.

[*3] Units of Si and Al^t are per formula unit.

[*4] Temperature calculated following Holland and Blundy (1994).

[*5] Pressures (MPa) calculated by Mutch et al. (2016).

Table 4. Chemical compositions (wt.%; n.d., not detected) of matrix glass in dacitic pumice.

Unit	J15-R	J15-R	J15-R	J15-R	J15-R	J15-P	J15-P	J15-P
Sample name	121202C-B1	121202C-B1	120801C-O	120801C-K	120801C-K	PH13F-PP-3	PH13F-PP-3	PH13F-PP-3
Point	B1-12-1	B1-66-3	O-28	K-4	K-21	PP-2	PP-3	PP-4
SiO_2	75.76	75.87	76.49	74.76	75.70	64.22	63.48	65.41
TiO_2	0.11	0.11	0.18	0.17	0.12	0.16	0.08	0.11
Al_2O_3	12.67	12.60	12.38	11.86	12.33	19.21	18.82	18.60
FeO^{t*1}	0.74	0.75	0.73	0.96	0.81	1.26	0.98	1.01
MnO	0.04	0.04	0.01	0.02	0.07	0.05	0.03	0.07
MgO	0.20	0.23	0.19	0.49	0.21	1.00	0.77	0.61
CaO	1.16	1.23	1.17	1.19	1.26	5.04	4.81	4.76
Na_2O	3.80	4.02	4.20	4.27	4.14	5.26	5.65	5.13
K_2O	3.30	3.23	3.40	3.38	3.29	1.71	1.43	1.65
P_2O_5	0.02	n.d.	0.07	0.03	0.08	< 0.01	0.05	0.02
Total	97.80	98.08	98.81	97.14	98.01	97.91	96.10	97.37

[*1] Total Fe is expressed as FeO^t.

Table 5. Estimated bulk major (wt.%) and trace (ppm) elements, and isotopic compositions of two silicic end-member magmas.

End-member	D1	D2
SiO_2	63.97	66.37
TiO_2	0.56	0.52
Al_2O_3	16.84	16.15
FeO^{t*1}	4.29	3.86
MnO	0.11	0.10
MgO	2.59	2.2
CaO	5.44	4.53
Na_2O	4.58	4.46
K_2O	1.43	1.62
P_2O_5	0.20	0.18
Total	100.00	100.00
Rb	39.1	46.4
Sr	572	544
Y	17	14
Zr	128	121
Nb	4.1	4.2
Ba	455	510
La	14.9	15.6
Ce	29.9	31.2
Nd	14.4	14.2
Sm	3.0	2.9
Eu	0.83	0.74
Yb	1.3	1.2
Lu	0.2	0.2
$^{87}Sr/^{86}Sr$	0.704187	0.704195
$^{143}Nd/^{144}Nd$	0.512918	0.512919
$^{206}Pb/^{204}Pb$	18.4232	18.4235

[*1] Total Fe is expressed as FeO^t.

Abbreviations: D1, less silicic end-member; D2, more silicic end-member (see text for detail).

Chapter 7: Conclusions

We analyzed the petrology and geochemistry of juvenile eruptive products of the 1991 Pinatubo eruption to re-evaluate the role of magma mixing during the pre-eruptive formation and evolution of the magma plumbing system. Our main conclusions are as follows.

1. The basaltic magma that triggered the eruption was injected into a hybrid dacitic magma. The compositional variations of phenocrysts, such as plagioclase and amphibole, and the whole rock compositions of dacitic pumices suggest that the hybrid dacitic magma was the products of various dacitic melts and/or magmas, which can be approximately considered as the mixing of at least two similar, but distinct, silicic end-member magmas; here, we considered a hotter, less silicic magma (D1) and a cooler, more silicic one (D2).
2. Our new data confirm that the hybrid dacitic magma could not have been produced by the fractional crystallization of the injected 1991 basaltic magma. Thus, the dacitic magmas must have been generated by the partial melting of crustal materials due to heating by the underplating basaltic magma.
3. We showed that is not possible to form the more silicic end-member magma by fractional crystallization of the less silicic one. Thus, these silicic end-member magmas must have been produced independently, but simultaneously. We attribute the heterogeneous silicic melts to the melting of heterogeneous crustal materials at various temperatures and depths.
4. The pre-eruptive processes of the 1991 Pinatubo eruption can be divided into the formation of the hybrid dacite magma and the triggering of the eruption. The former was initiated by the formation of heterogeneous silicic melts in a crystal mush zone within the crust. The extraction and accumulation of these melts produced a large hybrid silicic magma chamber. The injection of the basaltic magma into the chamber then triggered the eruption.
5. We conclude that the pre-eruptive formation and evolution of the magma plumbing system of the 1991 eruption required at most 500 years, i.e., since the former Buag period.

Part 2:

Time scale of pre-eruptive processes of the 1991 Pinatubo eruption: Investigation into diffusion profile of phenocryst minerals

Abstract

Pinatubo volcano is the only one that erupted in 1991, the largest eruption in the latter half of the 20th century. Although geophysical data before the eruption exist, there are no examples of studies that verify the time scales of pre-eruptive processes inferred from petrological methods based on geophysical observation data. In this study, we estimated the time scales of the formation and evolution of the magma plumbing system in the 1991 eruption from the diffusion profiles of phenocryst minerals and verified the results with geophysical data to investigate the relationship between the magmatic processes and the precursor phenomena. The main magmatic processes in the 1991 eruption are the accumulation of compositionally and thermally heterogeneous silicic melts produced by partial melting and magma mixing between hybrid dacite and ascending basalt. The time scales of each magmatic process were estimated by investigating the diffusion profiles of quartz in dacitic pumice for the accumulation and titano-magnetite in andesitic scoria for the magma mixing. As a result, the accumulation of silicic melts started more than 400 years ago and continued until 3 years before the eruption. Furthermore, the shallow magma chamber may have grown rapidly from 30 years before the eruption. On the other hand, the magma mixing started less than 50 days before the eruption and continued until 2 hours ago. Andesitic magma may have grown rapidly 3 days before the eruption. Furthermore, the time scale of magmatic process was verified from geophysical observations, and the timing of the rapid growth of andesitic magma is consistent with the swarm of shallow low-frequency tremor and rapid increase of SO_2 emission. The inflation of magma mixing and the rise of its mixed magma may be observed as shallow low-frequency tremor in the conduit. Moreover, this is preceded the swarm of deep long period earthquakes as basaltic magma ascent. Thus, geophysical observations on the order of weeks or months may be sufficient to assess whether the eruption is imminent.

Chapter 1: Introduction

In many volcanoes, precursor phenomena such as crustal deformation, seismic activity, thermal anomalies, or changes in the composition of volcanic gases and hydrothermal fluids are often observed before an eruption (e.g., Daag et al. 1996; Sakai et al. 2001; Umakoshi et al. 2001; Yoshida et al. 2002). If we can understand how these geophysical and geochemical observations correspond to the magmatic processes at the depths of volcanoes revealed by petrology, we can not only understand volcanic eruptions but also contribute to eruption prediction. For this understanding, it is essential to inscribe the time axis of magmatic processes using petrological methods. In this context, there are several previous studies that have tried geophysical observations against the time scales of magmatic processes estimated from petrological methods (Tomiya et al., 2013; Kilgour et al., 2014; Moore et al., 2014; Rae et al., 2016; Viccaro et al. 2016). However, these studies are currently limited to recent small- to medium-scale eruptions with observational cases (VEI 4 or less; Newhall and Self, 1982).

On the other hand, due to the lack of geophysical observation of large-scale eruptions that form calderas with VEI greater than 6, the time scales of magma plumbing systems have been investigated mainly by petrological methods (e.g., Wark et al., 2007; Druitt et al., 2012; Matthews et al, 2012; Chamberlain et al., 2014; Matsumoto et al., 2018). These studies have revealed that the time scale between magma injection into magma chamber and eruption that triggers large-scale eruptions is on the order of years to centuries (Wark et al., 2007; Matthews et al., 2012; Tomiya et al., 2013; Matsumoto et al., 2018). In some volcanoes, eruptions are triggered not only by mafic magma but also by the injection of silicic magma (Morgan et al., 2006; de Silva et al., 2008; Saunders et al., 2010; Druitt et al., 2012). These results point to the importance of long-term geophysical observations prior to eruptions in large-scale eruptions such as those that form calderas (Druitt et al., 2012). In order to verify the pre-eruptive process of these unrecorded past large-scale eruptions, it is necessary to compare the time scales of the formation and evolution of the magma plumbing system estimated by petrological methods with those of geophysical observations before the eruption, and to clarify the relationship between them.

Pinatubo volcano located in the northern part of Luzon Island, Philippines (Fig. 1), which erupted in June 1991 with a VEI=6, ejecting a large amount of dacitic magma (Scott et al., 1996). Since Pinatubo volcano had been in a quiescent phase for about 500 years, no geophysical observations had been made, but the phreatic eruption two months before the climactic eruption triggered observations by PHIVOLCS (Philippine Institute Volcanology and Seismology) and USGS (U.S. Geological Survey) (Lockhart et al, 1996). Thereby, geophysical observations have been recorded for up to two months until climactic eruption on June 15. This eruption was one of the largest eruptions of the second half of 20th century, and many studies were conducted after the eruption (e.g., Pallister et al. 1992, 1996; Bernard et al. 1996; Luhr and Melson, 1996; Muro et al. 2008; Borisova et al, 2014), which revealed the structure of the magma plumbing system before the eruption and magmatic processes during the eruption. The 1991 eruption was triggered by the injection of basaltic magma into a shallow dacitic magma chamber just before the eruption (Pallister et al., 1992, 1996). In addition to that, basaltic injection was assumed based on the seismic activity before the eruption (White, 1996), but the contrast between magmatic processes and observational data with clear time scales by petrological methods has not been studied. Later, U-Th dating was used to estimate the age of phenocryst mineral formation (King et al., 2016), but the magmatic processes and their time scales have not yet been clarified.

Recently, the evolution of the magma plumbing system and the eruptive process of the 1991 eruption have been re-examined, and not only the magmatic process immediately before the eruption but also the evolutionary process of the dacitic magma chamber has been clarified (Part 1). In order to clarify the time scale of the formation and evolution process of the magma plumbing system of 1991 eruption, we analyzed the compositional zoning structure of quartz and titano-magnetite in volcanic products. We then contrast the geophysical data recorded before the eruption with the magmatic processes revealed by petrological methods, and discuss the relationship between them.

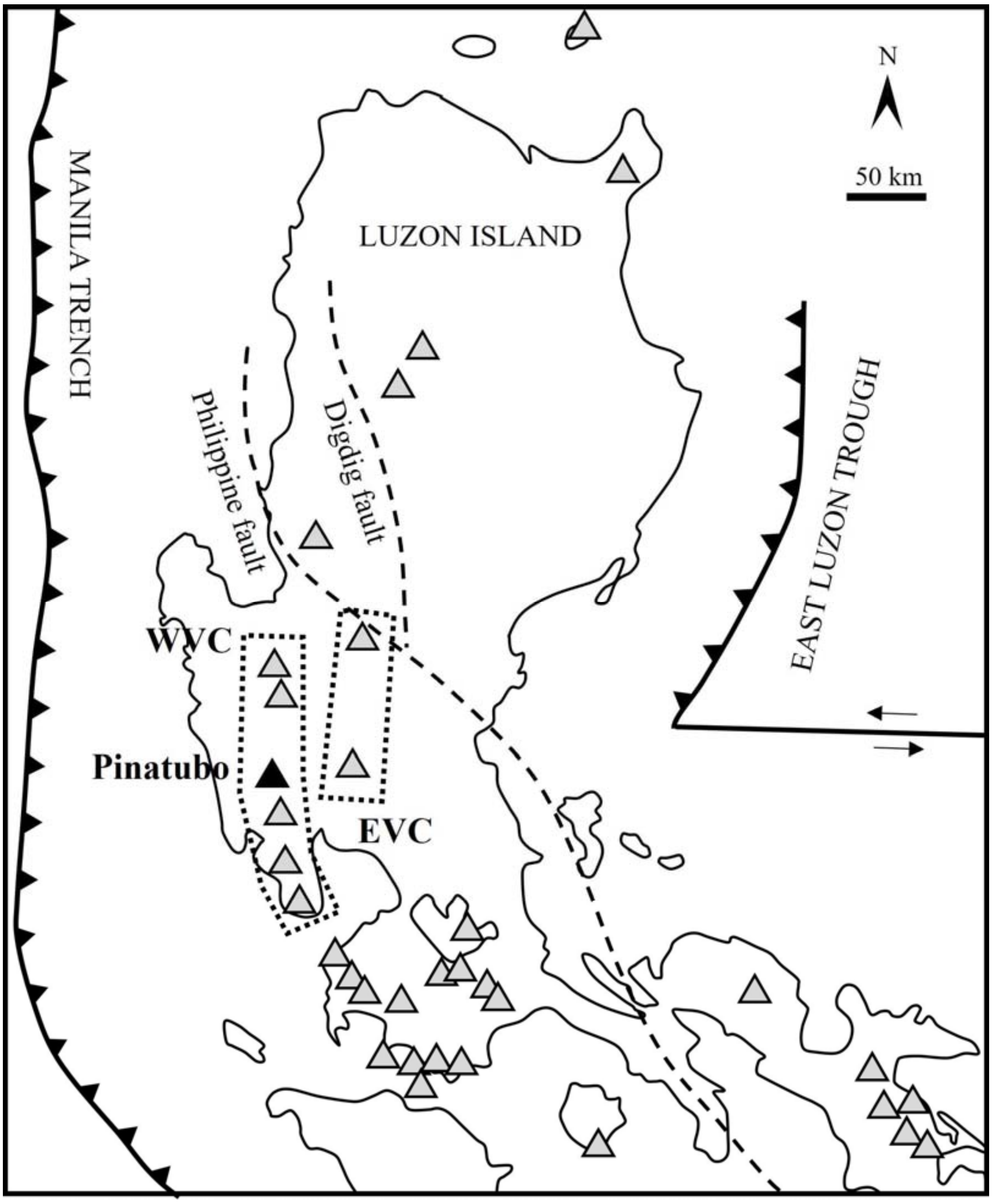

Fig.1. Location map of Pinatubo volcano at the north part of Luzon Island, Philippines. WVC and EVC show western and eastern volcanic chains, respectively. Pinatubo volcano belongs in WVC, and is labeled as black triangle. Gray triangles show other volcanoes. This figure was modified after Borisova et al. (2014).

Chapter 2: History of activities in Pinatubo volcano

Pinatubo volcano started its activity about 1 million years ago, and is divided into ancestral and modern activities after the formation of the Tayawan caldera about 40,000 years ago (Delfin, 1983, 1984; Newhall et al., 1996). The ancestral activity is due to andesitic to dacitic magma, with pyroclastic flow deposits and multiple vents associated with the formation of the Tayawan caldera. On the other hand, the modern activity produced six pyroclastic flow eruptions except for the 1991 eruption, all of which were dominated by dacitic magma (Fig. 2). The interval between the six eruptions tends to decrease with age, and the quiescent period before the 1991 eruption was about 500 years (Newhall et al., 1996).

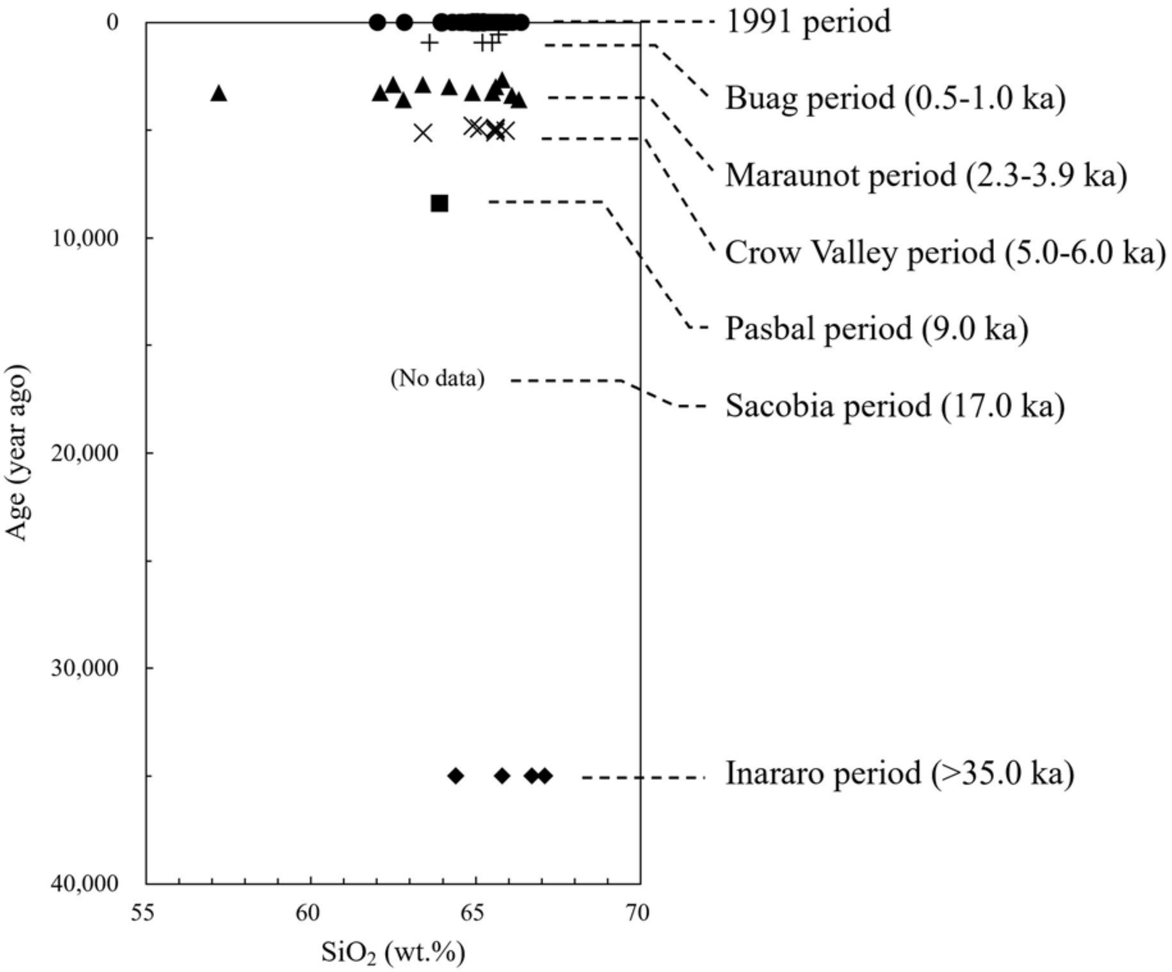

Fig. 2. Volcanic periods and bulk compositions of Pinatubo volcano during past 40,000 years. Bulk compositions before 1991 eruption were taken from Newhall et al. (1996).

Chapter 3: Outline of the 1991 Pinatubo eruption

The 1991 activity began with a phreatic eruption on April 2, which was preceded by felt earthquake on March 15 (Sabit et al., 1996). Thereafter, small eruptions emitting volcanic gas and ash continued intermittently until the end of May. In June, it continued to erupt on a small scale, and a lava dome of andesitic magma appeared on June 7. The first plinian eruption occurred on June 12, ejecting andesitic magma. A dozen more eruptions of the vulcanian type followed (Hoblitt et al., 1996), and finally a climactic eruption occurred on June 15. This eruption lasted for 9-10 hours (Tahira, 1992; Tahira et al., 1996), ejected a large amount of dacitic magma, and was the largest eruption in the second half of the 20th century (Schmincke, 2004).

Geophysical observations were initiated by PHIVOLCS on April 2 following the phreatic eruption on April 2 (Fig. 3; Lockhart et al., 1996; Sabit et al., 1996). After April 26, USGS began to install instruments, and the epicenters of volcanic earthquakes began to be identified around May 7 (Lockhart et al., 1996; Mori et al., 1996). SO_2 emissions in volcanic gases were also measured by COSPEC (correlation spectrometer) once every 3-4 days after May 13 (Daag et al., 1996). Observations around the summit by tiltmeter began on June 1, although only at one location, and continued until June 13 when the instrument was destroyed (Ewert et al., 1996). On the other hand, several USGS seismic instruments were damaged by small eruptions that occurred before June 12, and furthermore, all instruments installed around the mountain body were destroyed until the climactic eruption on June 15 (Lockhart et al., 1996). However, before the first plinian eruption on June 12, the epicenter locations of volcanic earthquakes were identified and their time trends were investigated (Hoblitt et al., 1996; Mori et al., 1996).

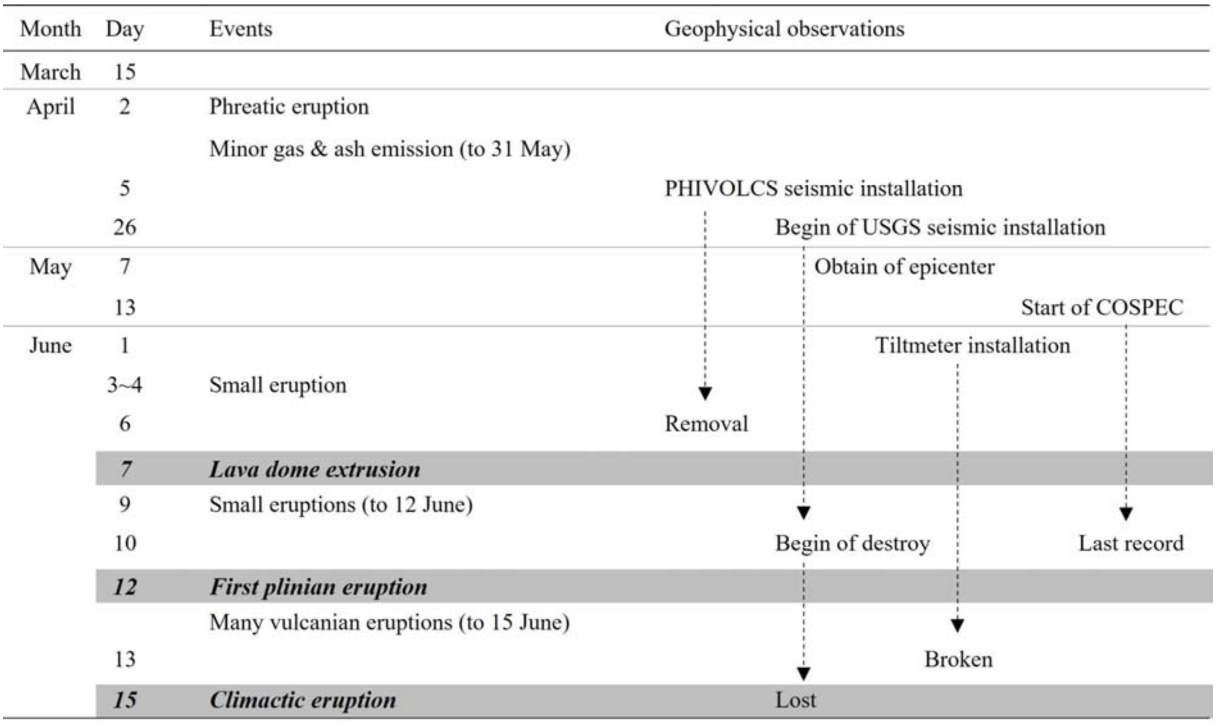

Month	Day	Events	Geophysical observations
March	15		
April	2	Phreatic eruption	
		Minor gas & ash emission (to 31 May)	
	5		PHIVOLCS seismic installation
	26		Begin of USGS seismic installation
May	7		Obtain of epicenter
	13		Start of COSPEC
June	1		Tiltmeter installation
	3~4	Small eruption	
	6		Removal
	7	***Lava dome extrusion***	
	9	Small eruptions (to 12 June)	
	10		Begin of destroy Last record
	12	***First plinian eruption***	
		Many vulcanian eruptions (to 15 June)	
	13		Broken
	15	***Climactic eruption***	Lost

Fig. 3. Transitions of eruptive activity and geophysical observations at Pinatubo volcano in 1991. This figure was based on Harlow et al. (1996), Sabit et al. (1996), Lockhart et al. (1996), Daag et al. (1996), Ewert et al. (1996).

Chapter 4: Magma plumbing system of the 1991 eruption

The main magmatic events of the 1991 eruption were the appearance of a lava dome on June 7 and the first plinian eruption on June 12 by andesitic magma and the subsequent climactic eruption on June 15 by dacitic magma. The andesitic lava on June 7 contains basaltic enclaves, and it has been clarified that the andesitic magma was produced by mixing between basaltic magma of this enclave and dacitic magma of the climactic eruption (Pallister et al., 1992, 1996).

The 1991 climactic eruption was caused by the injection of basaltic magma into a magma chamber of dacitic magma just before the eruption (Pallister et al., 1992, 1996). The basaltic injection caused magma mixing with the dacitic magma, and then the andesitic magma was produced and ejected on June 7 for lava dome and June 12 for first plinian. Subsequently, the dacitic magma also released as climactic and large-scale eruption (Pallister et al., 1996).

For the dacitic magma of the 1991 eruption, it was recently pointed out that the dacitic magma is heterogeneous based on the whole rock composition and contained phenocryst mineral composition, and that these diversities can be approximated by magma mixing of at least two silicic end-member magmas (Fig. 4; see Part 1). As a result, heterogeneous silicic magmas were generated due to the heterogeneity of the crustal material and the temperature gradient from the heat source, and these magmas accumulated to form the dacitic magma of 1991 (see Part 1). The 1991 eruption was preceded by the formation of heterogeneous silicic melts due to partial melting of crustal materials, the accumulation of these melts to produce a large amount of hybrid dacitic magma at shallow level, and the injection of basaltic magma into this magma.

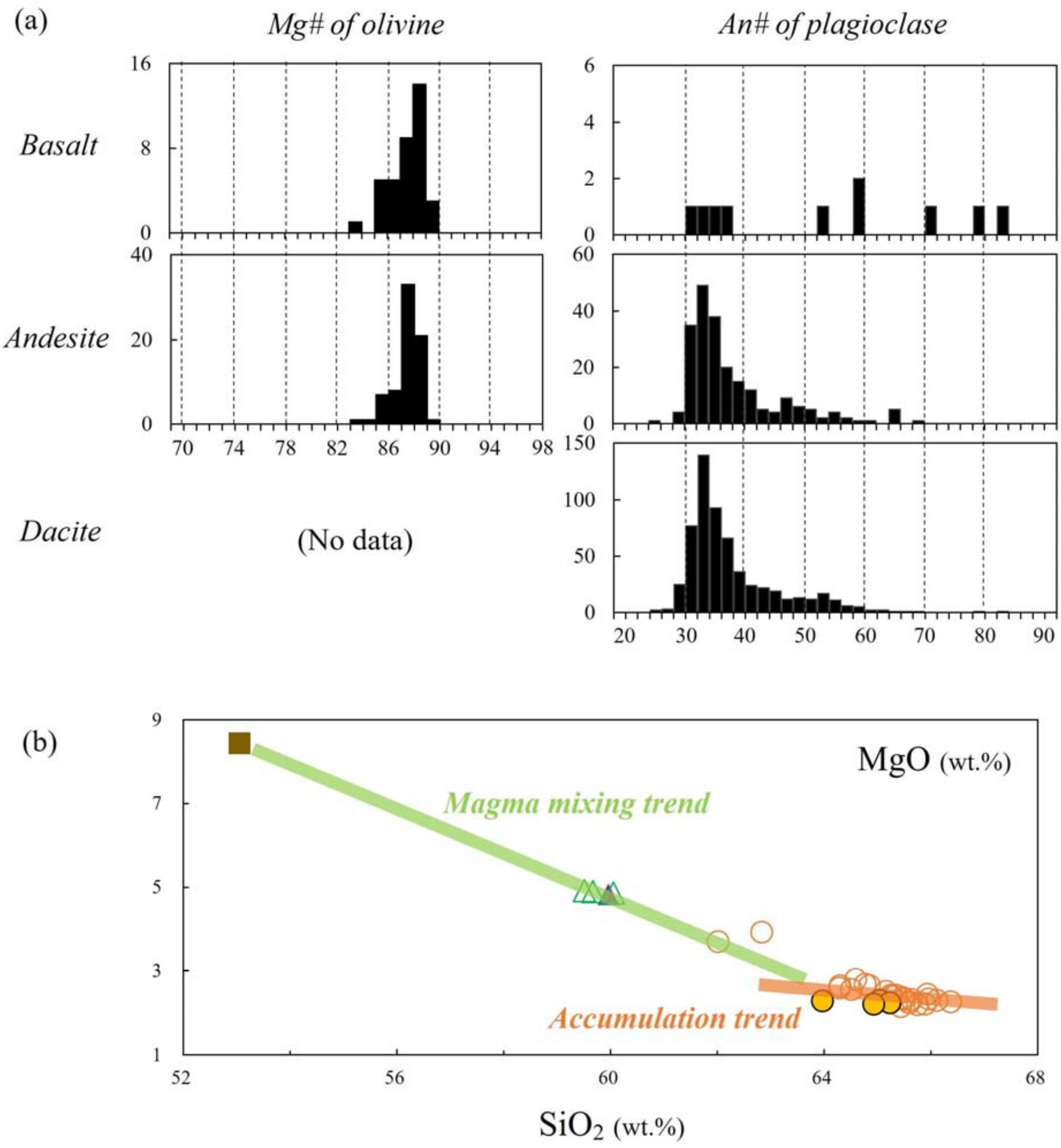

Fig. 4. Chemical compositions of phenocrysts (a) and whole rocks (b) in the 1991 Pinatubo eruption. See Part 1 for detail.

Chapter 5: Samples

5.1. Rock samples

Petrological characteristics of the rock samples used in this study are summarized in Table 1. The rock samples are basaltic enclave in the June 7 andesitic lava dome fragments, the June 12 andesitic scoria, and the June 15 dacitic pumice. Basaltic enclave shows whole rock composition of SiO_2 = 53.1 wt.% and contain plagioclase, hornblende, olivine, and clinopyroxene as major phenocryst, and quartz and opaque minerals (titano-magnetite only) as minor phenocryst (Table 1; see Part1).

Andesitic scoria has whole rock composition of SiO_2 = 59.5-60.1 wt.% and contains plagioclase, hornblende, olivine, and clinopyroxene as major phenocryst and quartz, biotite, and opaque minerals (magnetite + ilmenite) as minor phenocryst (Table 1). Although the June 7 lava dome fragment was not used in this study, it is of the same origin of andesitic magma because it shows similar phenocryst mineral assemblage and whole rock composition as the andesitic scoria on June 12 (Pallister et al., 1996; Part 1).

Dacitic pumice shows whole rock composition of SiO_2 = 62.0-66.4 wt.% and contains plagioclase, hornblende, and quartz as major phenocryst and opaque minerals (magnetite + ilmenite) as minor phenocryst (Table 1). It also rarely contains olivine, clinopyroxene, and biotite phenocrysts. There are also two types of pumice, gray with massive and white with vesicle (Pallister et al., 1996). Although the amount of phenocryst mineral in each type differs (Table 1), the whole rock composition and isotopic composition are similar, indicating the same origin of dacitic magma (Pallister et al., 1996; Part 1).

5.2. Focused minerals

In this study, we analyze the compositional zoning structure of quartz and titano-magnetite phenocryst minerals in all types of products from the 1991 eruption to examine the time scale of magmatic processes. These two minerals, together with common hornblende and low Ca plagioclase, are phenocryst minerals that were in equilibrium with dacitic magmas (Part 1), and quartz and titano-magnetite in andesitic to basaltic samples are dacitic end-member magma-derived phenocryst minerals according to magma mixing. In addition, the zoning structure of titano-magnetite could not be examined because the zoning structure of basaltic enclave is modified by cooling after eruption. The zoning structure of quartz could not be also examined because the amount of this phenocrysts in andesitic scoria was small and a clear zoning structure could not be confirmed due to the cutting surface during the preparation of thin sections.

Table 1. Sample and phenocryst list in the 1991 eruption.

Chemical type	Rock type	Unit	Bulk	Phenocrysts (vol.%)							
			SiO_2 (wt.%)	Plagioclase	Amphibole	Olivine	Clinopyroxene	Biotite	Quartz	Opaque[*1]	Total
Dacite (PR)	PR-pumice	June 15	64.0~66.4	9.6~16.6	1.2~8.1	tr.	n.c.~0.3	n.c.~2.6	n.c.~2.8	n.c.~0.4	11.9~22.3
Dacite (PP)	PP-pumice	June 15	64.0~65.2	2.5~3.7	0.3~1.1	n.c.	n.c.	n.c.	n.c.~0.1	n.c.~0.1	3.2~5.7
Andesite	Scoria	June 12	59.5~60.1	10.2~12.0	3.6~4.8	0.7~1.3	0.2~0.3	n.c.~0.3	0.3~1.1	n.c.~0.2	15.9~19.1
Andesite	Lava	June 7	60.0	17.1	6.0	2.6	1.1	< 0.1	2.5	< 0.1	29.4
Basalt	Enclave	June 7	53.1	8.8	6.4	2.9	1.4	n.c.	0.7	0.1	20.3

This table was based on Part 1.

[*1] Opaque includes titano-magnetite and ilmenite phenocrysts except for basaltic sample.

Abbreviations: PR = phenocryst-rich. PP = phenocryst-poor. n.c. = not counted. tr. = trace.

Chapter 6: Methods

6.1. Analytical methods

Quartz and titano-magnetite phenocrysts were not only found in thin sections, but in the scoria and pumice samples, the samples were crushed, the minerals were collected, and the quartz and titano-magnetite were separated by hand-picking and embedded in thin section for analysis.

For the quantitative analysis of Ti content in quartz crystal, field emission electron probe microanalyzer (FE-EPMA; JEOL JXA-8530F) with good analytical accuracy was used. The measurement conditions were 15 kV accelerating voltage and 200 nA beam current. Correction for analysis using the microanalyzer was performed using the ZAF method. Zoning structure of quartz was observed by using cathodoluminescence images (hereafter referred to as “CL image”). The color contrast expressed in CL images is linearly and positively correlated with the amount of Ti content in quartz (e.g., Peppard et al., 2001; Wark and Spear, 2005; Rusk et al., 2008). Using this relation, we converted CL image to grayscale and estimated Ti content in other quartz crystals using the results of quantitative analysis of some quartz. The procedure from grayscale to estimation of Ti content is shown in Appendix A.

The chemical composition of titano-magnetite was analyzed using electron probe microanalyzer (EPMA; JEOL JXA-8800R). The measurement conditions were 15 kV accelerating voltage and 20 nA beam current. Correction for analysis using the microanalyzer was performed using the ZAF method. Zoning profiles were analyzed at intervals of 2-4 μm, considering the size of each crystal.

6.2. Diffusion profiles

The analysis of the diffusion profile of quartz follows the methods of previous studies (e.g., Cherniak et al., 2007; Wark et al., 2007; Gualda et al., 2012; Matthews et al., 2012), and the detailed analysis procedure is shown in Appendix B. The diffusion time is calculated for all quartz used in this study, but the calculated diffusion time is the maximum value because the quartz was not cut with parallel to c-axis.

The analysis of titano-magnetite diffusion profile follows the methods of previous studies (e.g., Nakamura, 1995; Tomiya et al., 2013; Matsumoto et al., 2018), and the detailed analysis procedure is shown in Appendix C.

Chapter 7: Zoning structure of quartz

7.1. Petrography of quartz

Quartz in dacitic pumice is 1.9 mm in maximum grain size and 2.8 vol.% in maximum content. The shape of phenocryst is elliptical, but partially fragmentary (Figs. 5a-f). On the other hand, quartz in basaltic enclave has a maximum grain size of 2.3 mm and 0.7 vol.% in content. The surroundings of phenocryst are markedly uneven and irregularly shaped (Figs. 5g-i).

7.2. Core and rim of quartz

Core and rim compositions of quartz in dacitic pumice and basaltic enclave are shown in Fig. 6. Quartz in dacitic pumice shows Ti = 65-162 ppm in the core and Ti = 69-170 ppm in the rim. The core and rim tend to be comparable or the Ti content in the rim is slightly higher (Fig. 6). On the other hand, the basaltic enclave of quartz shows Ti = 91-124 ppm in the core and Ti = 190-195 ppm in the rim. Ti content of the rim is much higher than that of the core and shows a clear reverse zoning structure (Fig. 6). Ti content of the rim is very much higher than that of the quartz rim of dacitic pumice.

7.3. Zoning pattern of quartz

According to CL images of quartz phenocryst, most of them show oscillatory zoning structures (Fig. 5a-f). The number of zoning band varies from crystal to crystal. Some crystals are euhedral, while others are fragmented. On the other hand, regardless of whether the crystals pass through the center or not, all crystals have zoning band at outer rim (Fig. 5).

Quartz of basaltic enclave is similar to that of dacitic pumice in that it has crystals with oscillatory zoning structure (Fig. 5g), but the outer rim in crystals have a very bright rim (Fig. 5g-i). This is a feature not found in dacitic pumice quartz.

The compositional profile of quartz shows compositional changes from core to rim (Fig. 7). Dacitic pumice quartz shows repeated increases and decreases in Ti content (Fig. 7a-f), corresponding to the color variation in the CL images. The amount of variation ranges roughly from 50 ppm to 170 ppm, with most of the variation within 150 ppm. Similar to dacitic pumice, quartz of basaltic enclave may also show oscillatory zoning structure or, conversely, a homogeneous composition inside (Fig. 7). However, as in the core-rim diagram (Fig. 6), quartz in basaltic enclave shows very high Ti content in outer rim. This feature is not found in quartz of dacitic pumice.

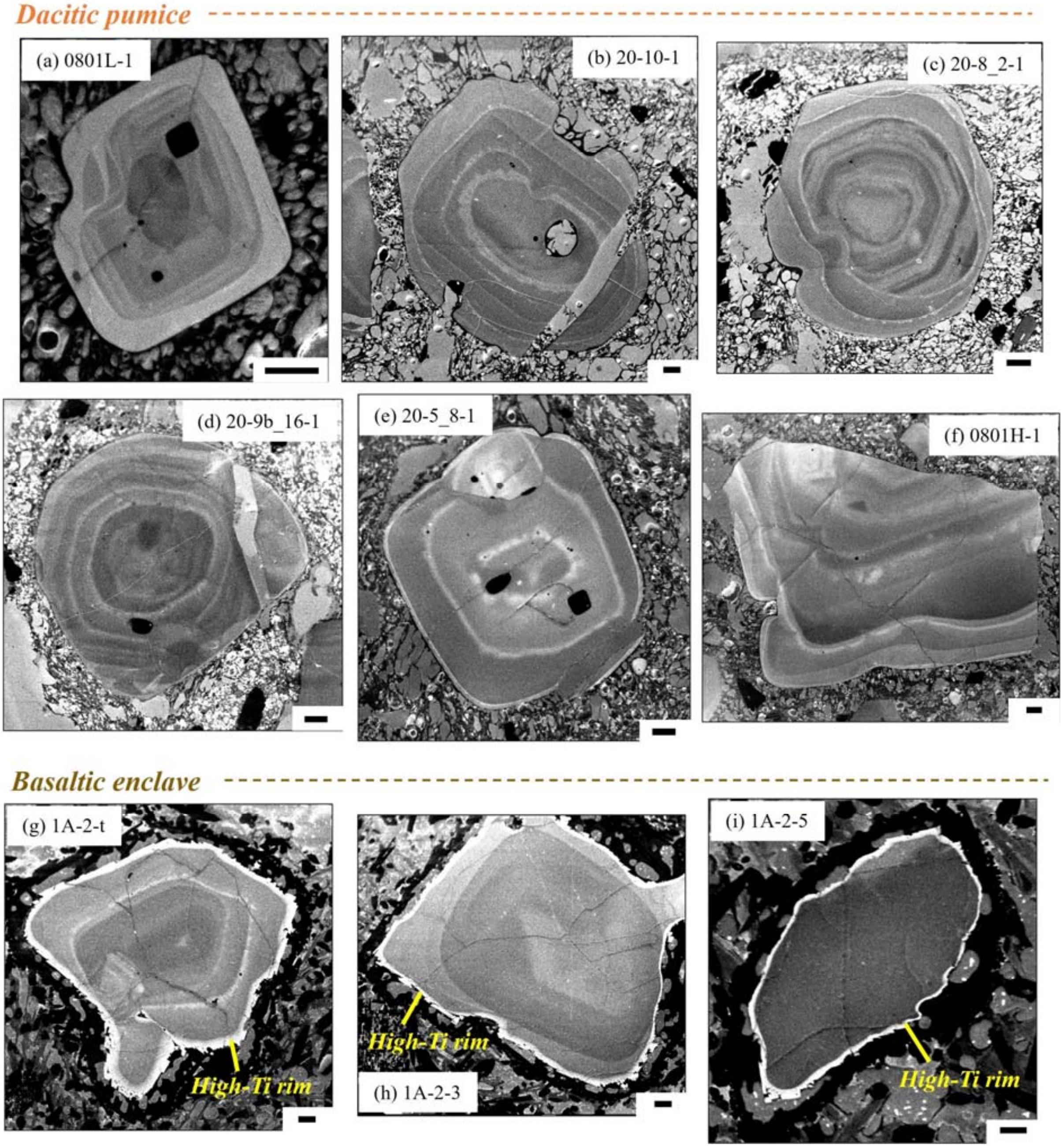

Fig. 5. Cathodoluminescence images of quartz in juvenile materials from the 1991 eruption. (a) to (f) are crystals in dacitic pumice and (g) to (i) are crystals in basaltic enclave. The black bar in the image shows the scale of 100 μm.

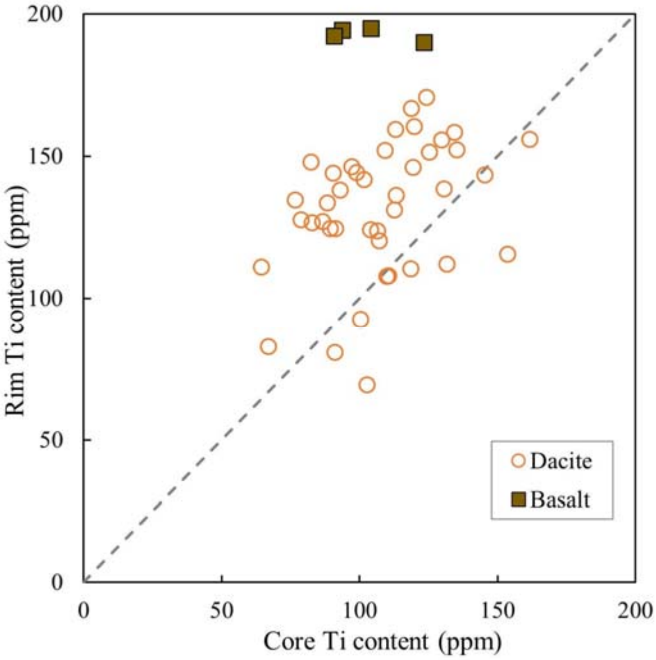

Fig. 6. Core-rim diagram of Ti content in quartz. Open circle and solid square show quartz in dacitic pumice and in basalt enclave, respectively.

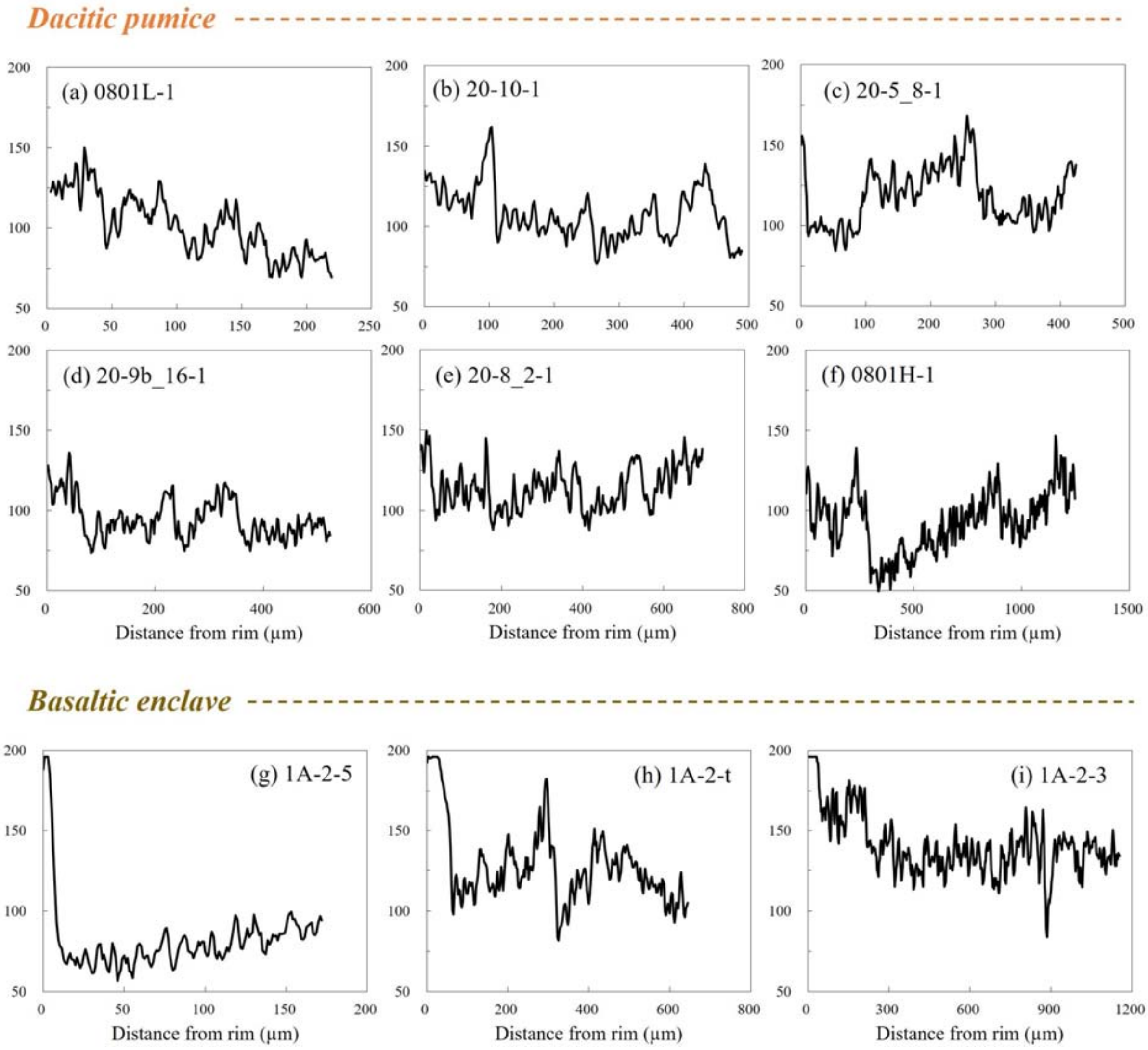

Fig. 7. Compositional profiles of quartz. (a) to (f) and (g) to (i) show the composition of quartz in dacitic pumice and basaltic enclave, respectively.

8. Zoning structure of titano-magnetite

8.1. Petrography of titano-magnetite

Titano-magnetite in andesitic scoria has a maximum grain size of 0.6 mm and a maximum of 0.2 vol.% in content. This phenocryst shows a short columnar shape, but some of the surroundings is partially deformed into a curved to concave shape (Fig. 8a-f). BSE image shows a color change at the outer rim of crystal (Fig. 8a-f). This color variation ranges from a few μm to several tens of μm. Titano-magnetite in dacitic pumice shows a maximum grain size of 0.8 mm, a maximum of 0.1 vol.% in content, and a short columnar shape (Fig. 8g-i). On the other hand, titano-magnetite in dacitic pumice shows homogeneous coloration from core to rim.

8.2. Core and rim of titano-magnetite

Core and rim compositions of titano-magnetite in andesitic scoria and dacitic pumice are shown in Fig. 9. Titano-magnetite in andesitic scoria shows TiO_2 = 3.7-4.6 wt.% (some with 6.4-7.0 wt.%) and Al_2O_3 = 1.5-2.4 wt.% in the core, and TiO_2 = 3.8-7.7 wt.% and Al_2O_3 = 1.7-3.8 wt.% in the rim. Because the core is relatively homogeneous and the rim has a wide range of compositions, titano-magnetite rim of andesitic scoria shows a reverse zoning structure (Fig. 9). On the other hand, titano-magnetite of dacitic pumice shows a relatively homogeneous composition with TiO_2 = 3.7-4.6 wt.% and Al_2O_3 = 1.6-2.0 wt.% in both core and rim, similar to the composition of titano-magnetite core of andesitic scoria (Fig. 9).

8.3. Zoning pattern of titano-magnetite

The compositional profile of titano-magnetite is shown in Fig 10. Titano-magnetite in andesitic scoria shows a clear reverse zoning structure at outer rim, while that in dacitic pumice shows a homogeneous composition from core to rim. The compositional variation in the profile is the same as the core-rim feature shown in Fig 9.

In titano-magnetite rim of andesitic scoria, the position at which compositional change begins depends on the element (Figs. 8a-f): TiO_2 and Al_2O_3 change at 10-20 μm inside the rim, whereas MgO changes at 30 μm or more inside the rim. Compared to TiO_2 and Al_2O_3, the composition of MgO changes more to the inner side. In addition, some crystals have a compositional change further out than the inner zoning structure (Fig. 10f). In this case, the compositional change outside outer rim is of the same width for all elements.

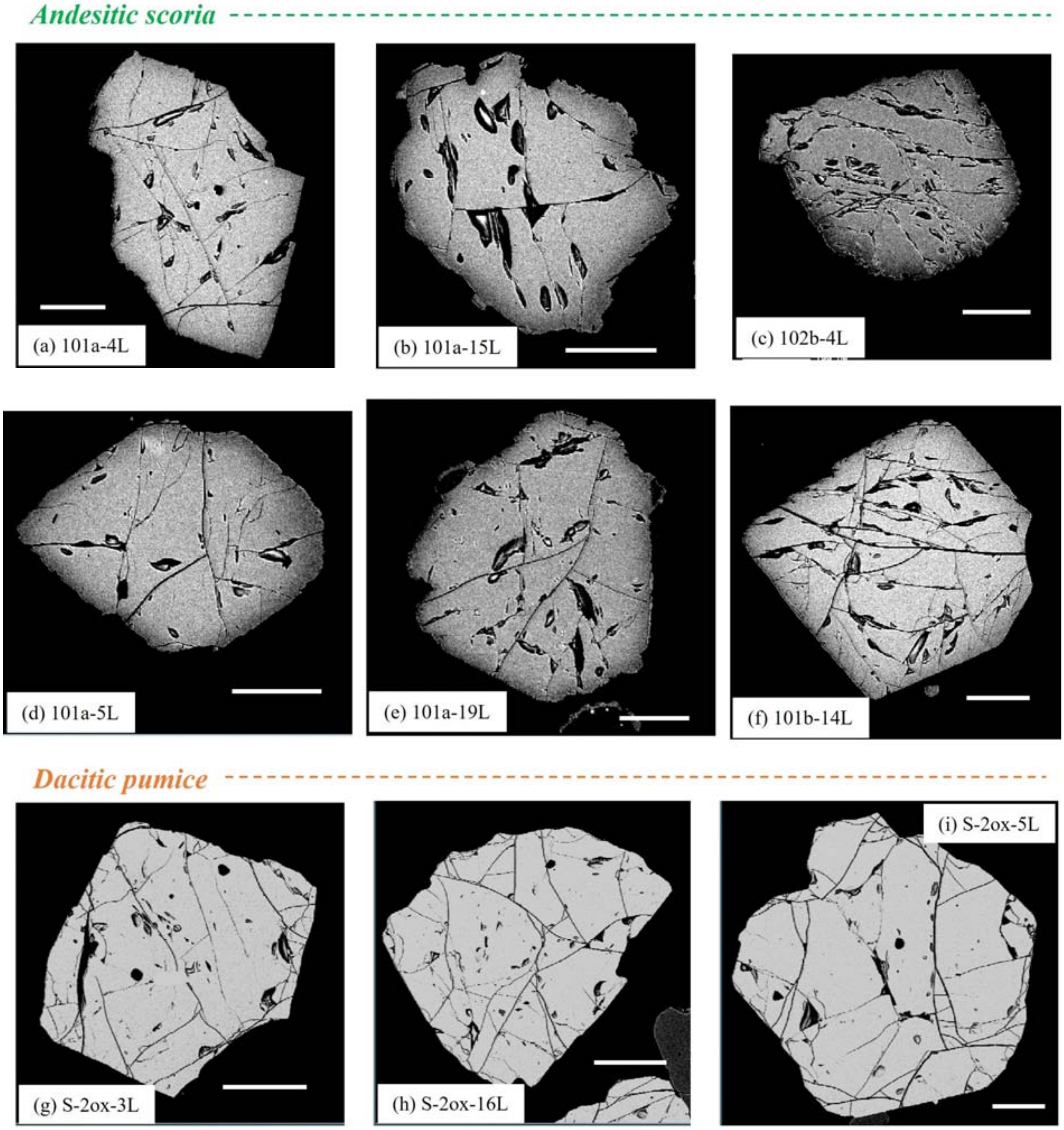

Fig. 8. Back-scattered electron images of titano-magnetite. (a) to (f) and (g) to (i) show titano-magnetite in andesitic scoria and dacitic pumice, respectively. The white bar in this image shows the scale of 100 µm.

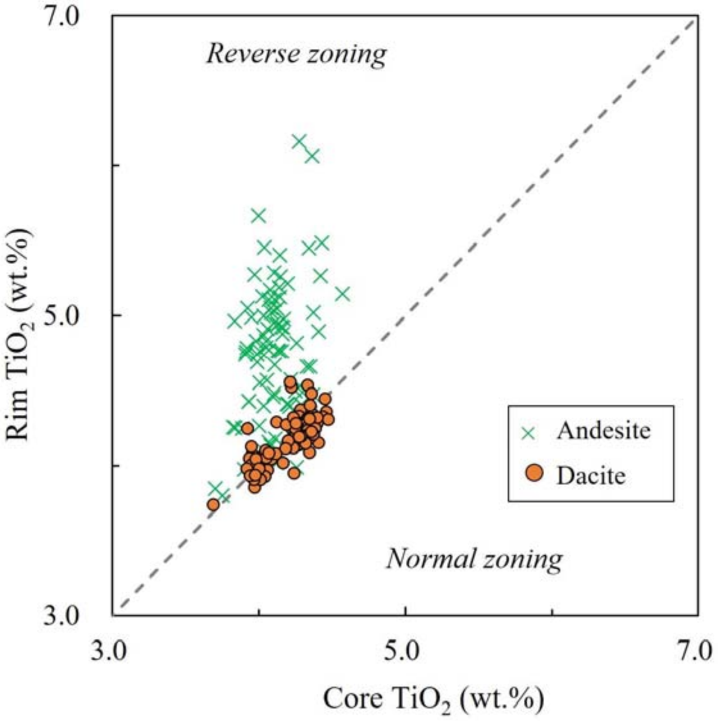

Fig. 9. Core-rim diagram of TiO2 content of titano-magnetite. Cross and black circle show the compositions of titano-magnetite in andesitic scoria and dacitic pumice, respectively.

Andesitic scoria

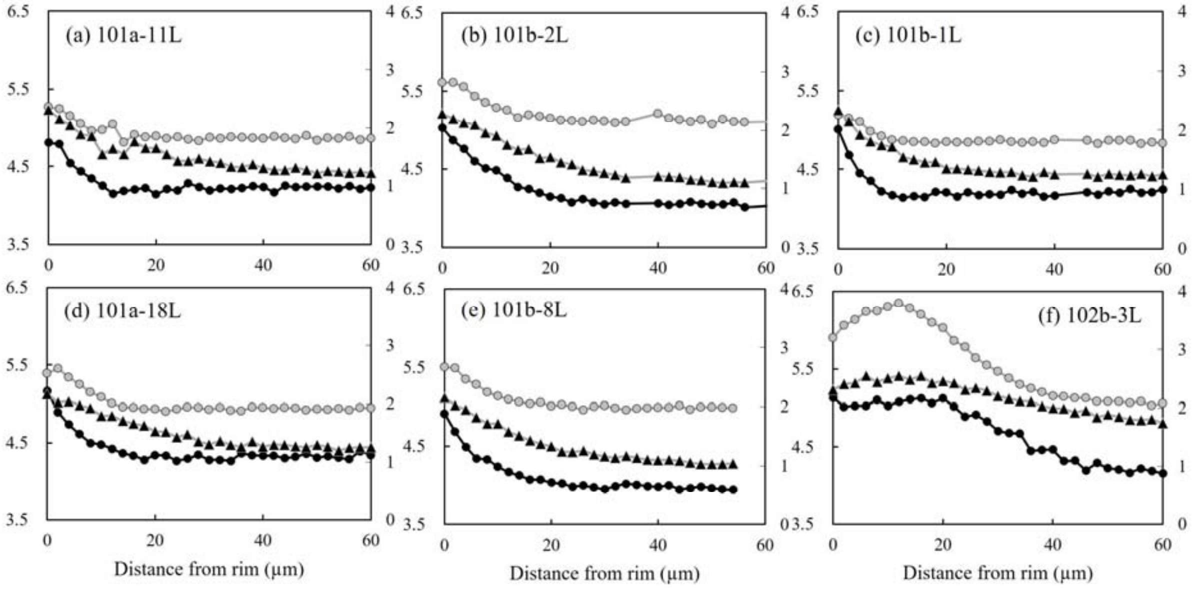

Dacitic pumice

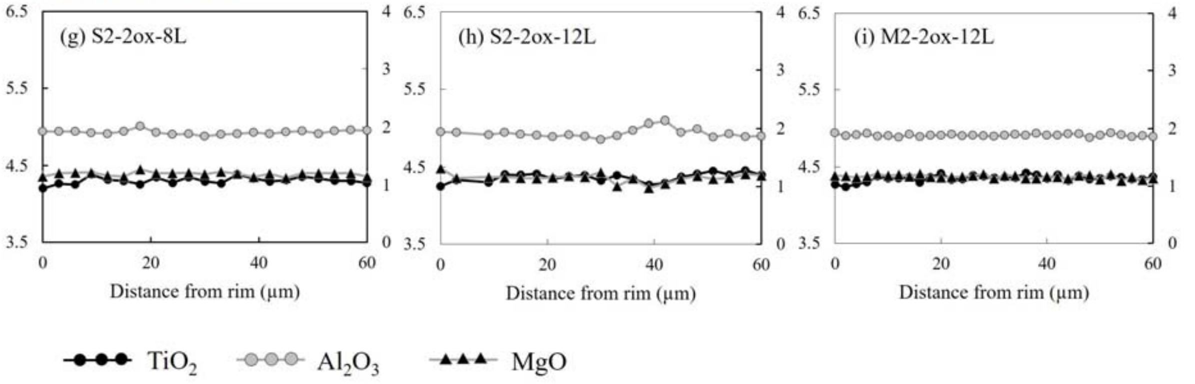

Fig. 10. Compositional profiles of titano-magnetite. (a) to (f) and (g) to (i) show the composition of titano-magnetite in andesitic scoria and dacitic pumice. Black solid, gray solid and gray dashed lines show TiO_2, Al_2O_3 and MgO contents, respectively.

9. Time scales of diffusion profiles

9.1. For dacite

Diffusion time estimated continuously from core to rim in quartz contained in dacitic pumice is shown (Fig. 11). Some crystals show a tendency of decreasing diffusion time from core to rim, while others do not show a clear decrease in diffusion time (Fig. 11). Since the diffusion time is expected to decrease gradually from core to rim in crystal growth, we considered the error of F-Ti oxides geothermometer (±33°C; Blundy and Cashman, 2008, see Appendix B for details). As a result, the diffusion time shows a similar or decreasing trend from core to rim, which is consistent with the process of crystal growth.

Diffusion time of quartz in dacite pumice is shown in Fig. 12. The diffusion time shows an overall range of 3 to 400 years, but the diffusion time tends to increase from rim (Fig. 12A) to core (Fig. 12F). In addition, many of diffusion times show within 30 years.

9.2. For andesite and basalt

Diffusion time of titano-magnetite in andesitic scoria is shown in Fig. 13a. This time ranges from 2 hours (0.08 days) to 50 days, with most of them showing within 3 days.

Diffusion time of the basaltic enclave is shown in Fig 13b. This time shows 1.1-3.3 days. Note that this diffusion time shows a similar time order to that of magnetite, whereas the lava dome appearance on 7 June is used as the time standard.

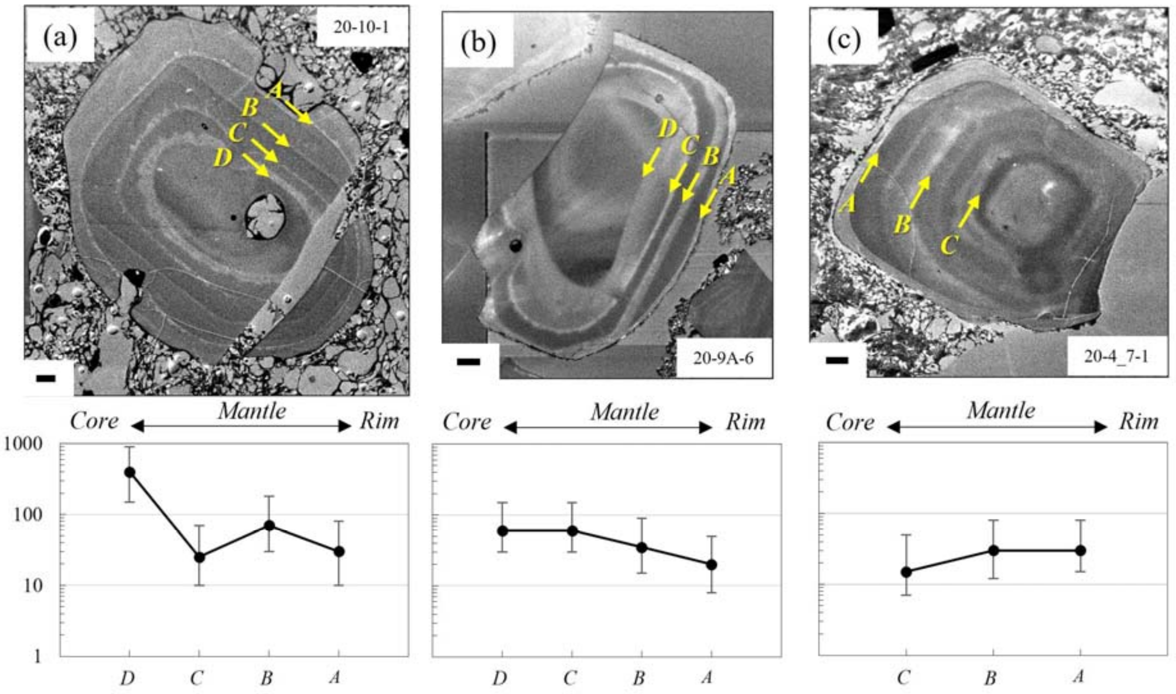

Fig. 11. Variation of the diffusion time in the direction of crystal growth. Upper and lower parts show cathodoluminescence image and the change of diffusion time, respectively. Location was labeled A, B, and so on, starting from outer rim. The black line at the bottom left of the CL image indicates the 100 μm scale.

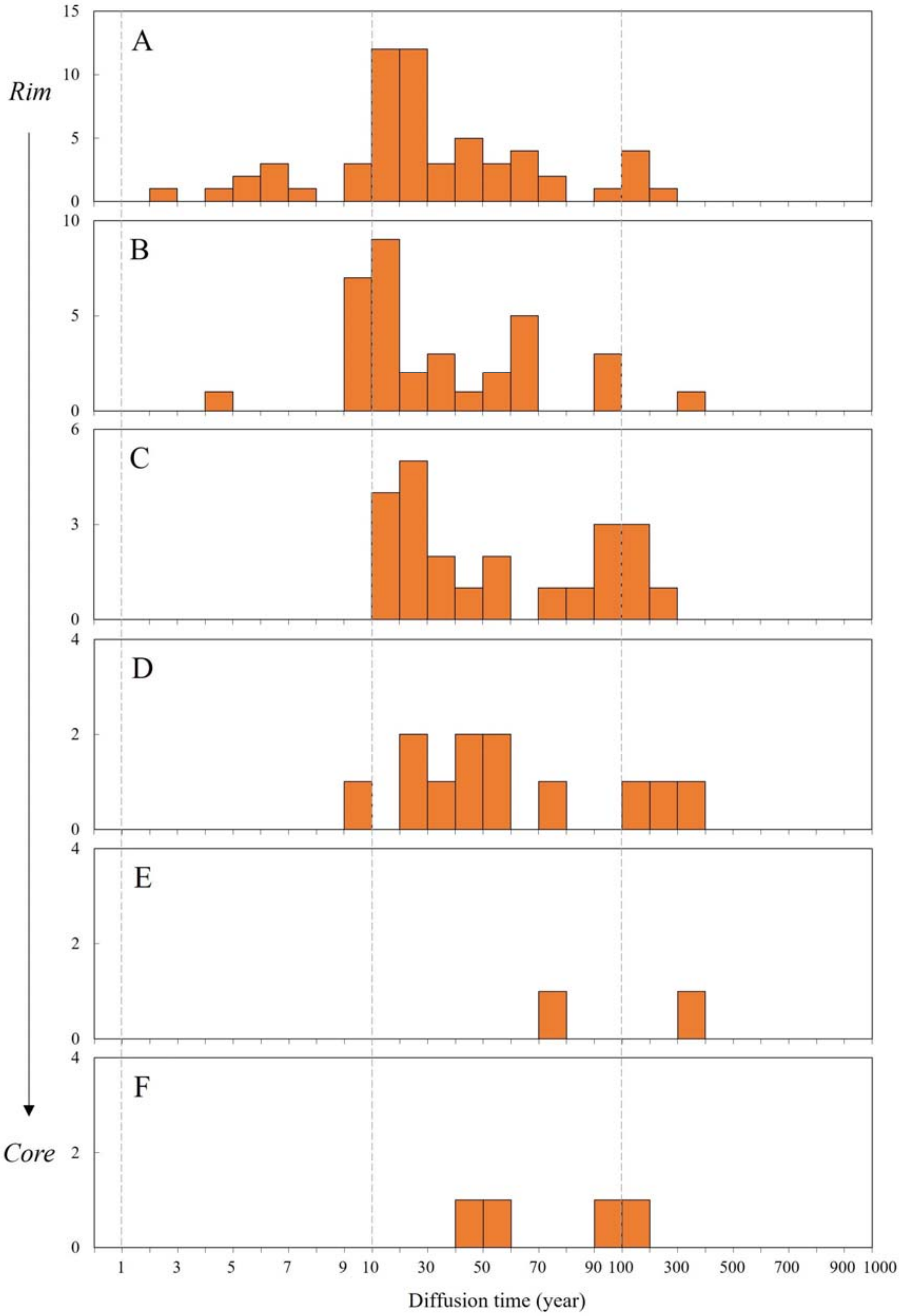

Fig. 12. Histogram of diffusion time of quartz in dacitic pumice. Zonings in quartz were labeled A, B, and so on, starting from outer rim to rim.

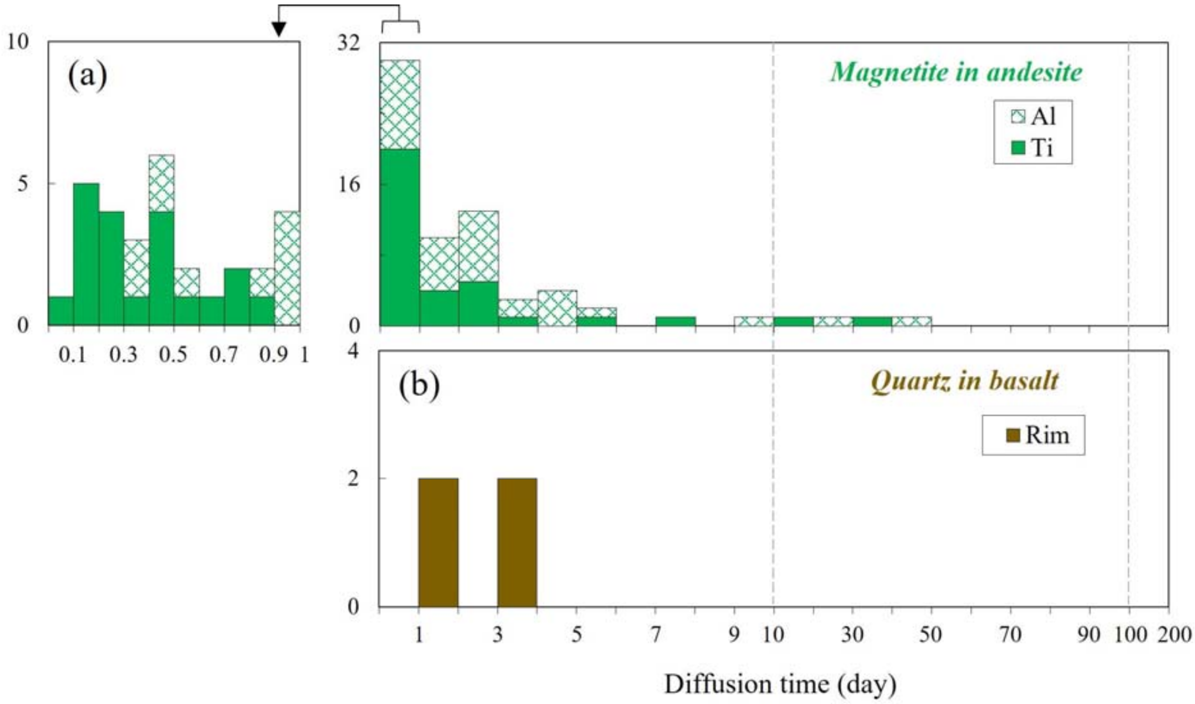

Fig. 13. Histogram of diffusion time for titano-magnetite and quartz rims. (a) Diffusion time estimated from titano-magnetite in andesitic scoria. (b) Diffusion time estimated from quartz rim in basaltic enclave. On left side of the top histogram is a detailed diagram of diffusion time within one day.

Chapter 10: Discussions

10.1. Relationship between host rocks and compositional structures of quartz and titano-magnetite

Quartz and titano-magnetite in dacitic samples, together with common hornblende and low Ca plagioclase, are phenocrysts minerals in equilibrium with dacitic magma (Part 1), and these minerals in andesitic to basaltic samples are ones derived from dacitic magma and captured by magma mixing. In other words, the compositional changes recorded in dacitic and andesitic to basaltic samples are different. Specifically, the minerals in andesitic to basaltic samples have undergone compositional changes at their rims due to magma mixing. Therefore, quartz and titano-magnetite in andesitic to basaltic samples record processes experienced by dacitic magmas on the inner side and by basaltic injection on the outer rim.

Quartz in dacitic pumice has multiple zonings, indicating that dacitic magmas have experienced not simple but complex magmatic processes. This multiple zoning is consistent with the model that dacitic magmas were produced by the accumulation of heterogeneous silicic melts (see Part 1).

On the other hand, titano-magnetite in andesitic scoria shows a clear reverse zoning structure, while that in dacitic pumice is homogeneous and has no zoning structure (Fig. 10g-i). In other words, titano-magnetite in dacitic pumice has not been affected compositionally or thermally by the injection of basaltic magma. The core should also have undergone some compositional and thermal changes due to dacitic magma accumulation of silicic melts, but since the latest time of silicic melt accumulation is three years ago (Fig. 12), the composition of titano-magnetite in dacitic magma is presumed to have homogenized over time since then (Devine et al, 2003).

10.2. Generating organization of dacitic magma based on quartz zonings

Quartz in dacitic pumice has a complex zoning structure, which indicates multiple changes in Ti content from core to rim of quartz (Fig. 7), and the temperature changes with Ti content, suggesting the involvement of thermally and compositionally different magmas. Therefore, the quartz phenocrysts may record the accumulation process of thermally and compositionally heterogeneous silicic melts produced by partial melting (see Part 1).

On the other hand, quartz in basaltic enclave has a similar complex zoning structure, whereas shows clearly higher Ti content at outer rim (Figs. 7, 14a). Magma temperature estimated from Ti content of rim is slightly above the upper limit of temperature of dacitic magmas (724-804 °C; Part 1) estimated from Fe-Ti oxide thermometers (Fig. 13b; Blundy and Cashman, 2008). Although the magma temperature is unlikely to show a clear difference because it reaches equilibrium in a relatively short time, the large increase in Ti content suggests the involvement of magma with high Ti content. However, the large increase in Ti content suggests the involvement of magma with high Ti content. Thus, the characteristic rim was formed by the injection of basaltic magma with high Ti content and temperature. Quartz rims in basaltic enclave record magmatic mixing processes prior to eruption.

Quartz in dacitic pumice shows a maximum diffusion time of 400 years (Fig. 15A), suggesting that the accumulation of silicic melts was already underway 400 years before the eruption (Fig. 15B-a). The minimum diffusion time is 3 years (Fig. 15A), suggesting that the accumulation of silicic melts continued until 3 years before the eruption. Furthermore, the diffusion time is mostly within 30 years (Fig. 12, 15A), suggesting that the accumulation of silicic melts was at its peak during this period and that the hybrid dacitic magma chamber grew rapidly (Fig. 15B-b). If this is the case, then the growth rate of magma chamber would have accelerated in the later stages of growth, rather than at the same rate over about 400 years (Druitt et al., 2012).

10.3. Organization of basaltic injection based on andesitic magma

Andesitic magmas are produced by mixing between dacitic and basaltic magmas, and the zoning structure of titano-magnetite is formed by magma mixing. The diffusion time of titano-magnetite in andesitic scoria is shown in Figure 13. This time ranges from 2 hours (0.08 days) to 50 days, suggesting that magma mixing may have already started 50 days before the eruption. This means that the basaltic magma rose from deep depth and reached near the bottom of the magma chamber before 50 days before the eruption. Time scale of diffusion obtained from titano-magnetite is also consistent with one of previous studies using same mineral at other volcanoes (weeks to months before eruption; Nakamura, 1995; Devine et al., 2003; Coombs et al., 2000).

Maximum diffusion time of titano-magnetite in andesitic scoria is 50 days (Fig. 15A), which indicates that andesitic magma had generated at least 50 days ago before the eruption (Fig. 15B-d). Thus, more than 50 days ago, basaltic magma had risen near the bottom of magma chamber and/or already injected into chamber (Fig. 15B-c). Diffusion time of titano-magnetite is also concentrated after 3 days before the eruption (Fig. 15A). This implies that magma mixing occurred frequently from 3 days ago to the eruption, which means that the supply of basaltic magma may have increased rapidly. Magma mixing may have proceeded simultaneously with magma ascent because it is difficult to finish the three processes, magma mixing, ascent and eruption, during short period of 3 days (Fig. 15B-e; e.g., Koyaguchi, 1985; Koyaguchi, 1986, Yamaguchi, 1996; Wada, 2000). Short time scale of 3 days before eruption is also consistent with one inferred from hornblende rims in previous studies (within a few days to less; Pallister et al., 1996).

10.4. Geophysical observations and magma processes

Before examining the pre-eruptive process time scale from the observed data, we present the observed data organized by previous studies and their interpretation. The number of volcanic earthquakes is organized at two different depths, and data exist since May 7 (Zobin, 2018). The earthquakes, which were predominantly 3-7 km below the surface 5 km northwest of the summit until the end of May, move to shallower than 4 km below the summit after June 1 (Fig. 16a). This has been interpreted as magma rising to shallower depths through the conduit (Mori et al., 1996; Harlow et al., 1996; Zobin, 2018). The seismic equipment installed by the PHIVOLCS records the number of high-frequency and low-frequency earthquakes occurring each day from April 5 to June 6 (Fig. 16b). The high-frequency earthquake is observed due to shear rupture of surrounding rocks caused by rising basaltic magma and plastic deformation of the upper part of magma chamber caused by increased pressure inside due to injection (e.g., Minakami, 1974; McNutt, 1996). Since the high-frequency earthquakes were already swarming when the observations started, it is possible that the basaltic magma had already risen and injected the magma reservoir before April 5 (Fig. 16d; Sabit et al., 1996). On the other hand, low-frequency earthquakes can be found when the volatile components in magma bubble up during the ascent as well as shallower volcanic tremor (e.g., Power et al., 1996; Yoshida et al., 2002). The swarm of low-frequency earthquakes during the two period, from April 8 to 22 and from May 27 to June 6, has been interpreted that the magma had risen to shallow underground (Sabit et al., 1996). In other words, magma mixing may have occurred prior to April 8 and May 27 (Fig. 16d). Two swarms of deep long period earthquakes were observed in the period from

May 26 to June 8, which was interpreted as basaltic magma rising from deep crust (White, 1996). The swarms of shallow low-frequency tremors and a sharp increase in SO_2 emissions were observed between June 9 and the first plinian eruption on June 12 (Fig. 16c; Power et al., 1996; Daag et al., 1996). This is interpreted to the rise of magma in preparation for the June 12 eruption, and the magma has risen to shallower level (Fig. 16d; Daag et al., 1996; Shinohara, 2018).

The magma movement inferred from the diffusion time scale was verified based on geophysical observations and their interpretation. Based on the diffusion time scale, the ascent and injection of basaltic magma is an event that occurred earlier than 50 days before the eruption (Fig. 17). However, it should have continued even after 50 days before the eruption (Fig. 17b). The timing of the basaltic magma ascent and injection is not known, whereas it partially overlaps with the period of the deep long period earthquakes (Figs. 16d, 17b). Given that the swarm of shallow low-frequency tremor was observed after the deep long period earthquake, it is possible that a large amount of basaltic magma was supplied during the deep long period earthquake. Next, the time scale shows that the magma mixing started 50 days ago (Fig. 17a). However, it is difficult to verify the timing of the onset of magma mixing from geophysical data, and the occurrence of high-frequency earthquakes may indicate magma mixing, but it is not certain (Fig. 16d). For the period from the acceleration of magma mixing to the eruption, the time scale indicates the period within 3 days of the eruption. During this period, a swarm of shallow low-frequency earthquakes and a rapid increase in SO_2 emission are observed. Therefore, the diffusion time indicated by titano-magnetite in andesitic scoria may represent the timing of magma mixing as magma rises in the shallow part of the volcano for eruption. Above results suggest that although the timing of the onset of magma mixing can be determined from the titano-magnetite diffusion profile, the pre-eruptive process time scale prior to the ascent of andesitic magma in the conduit cannot be determined with any accuracy.

Although time scale for the formation of hybrid dacitic magma is about 400 years (Fig. 12), there is no geophysical data observed during this period, and we cannot discuss the relationship between the petrological time scale and geophysical observations. However, in the case of Pinatubo volcano, the hybrid dacitic magma grew rapidly after 30 years before the eruption, and if we had observed crustal deformation and other phenomena during that period, we might have been able to predict the large-scale eruption. Other volcanoes that have erupted on a large-scale in the past have been reported to have accumulated large amounts of magma during the later decades to centuries of the evolution of the magma plumbing system (Morgan, 2006; Wark et al., 2007; de Silva et al., 2008; Saunders et al., 2010; Druitt et al., 2012). Therefore, it may be possible to observe the growth (accumulation) process of silicic magma by observing crustal deformation on the order of at least several decades, and to predict large-scale eruptions such as the formation of calderas.

In this study, we investigated the pre-eruptive process time scale of the 1991 Pinatubo magma plumbing system, and the relationship between magmatic processes in this system and the precursor phenomena of eruption. As a result, the inflation of magma mixing caused by the basaltic injection and the rise of its mixed magma are observed as shallow low-frequency tremor in the conduit. Moreover, this is preceded the swarm of deep long period earthquakes as basaltic magma ascent. Thus, geophysical observations on the order of weeks or months may be sufficient to assess whether the eruption is imminent. More studies like this one, which improved understanding of the time scales of pre-eruptive processes and the change in observed data, resulting that more realistic eruption prediction will be possible.

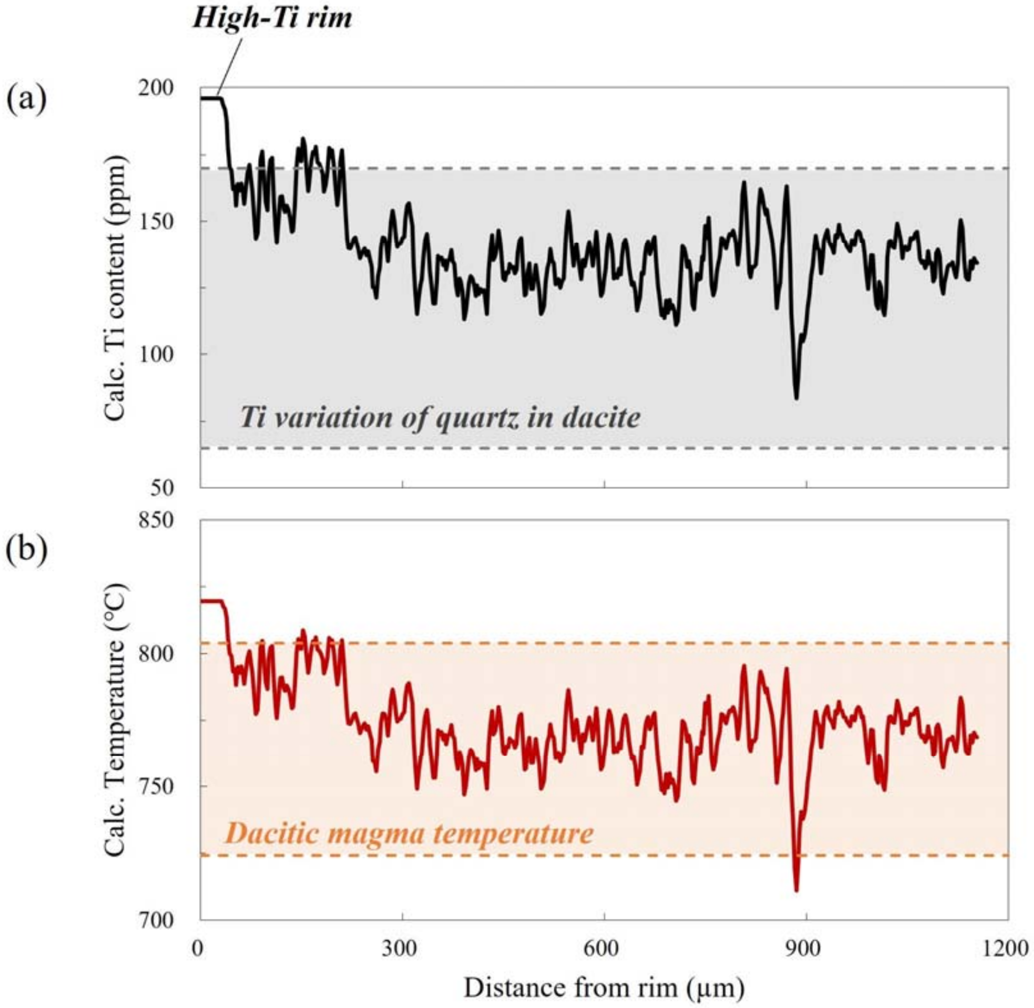

Fig. 14. Variation of Ti content (a) and temperature (b) in quartz of basaltic enclave. (a) Gray field shows the range of Ti content in dacitic pumice. (b) Light red filed shows the range of dacitic temperature estimated by Fe-Ti oxides geothermometer (Part 1).

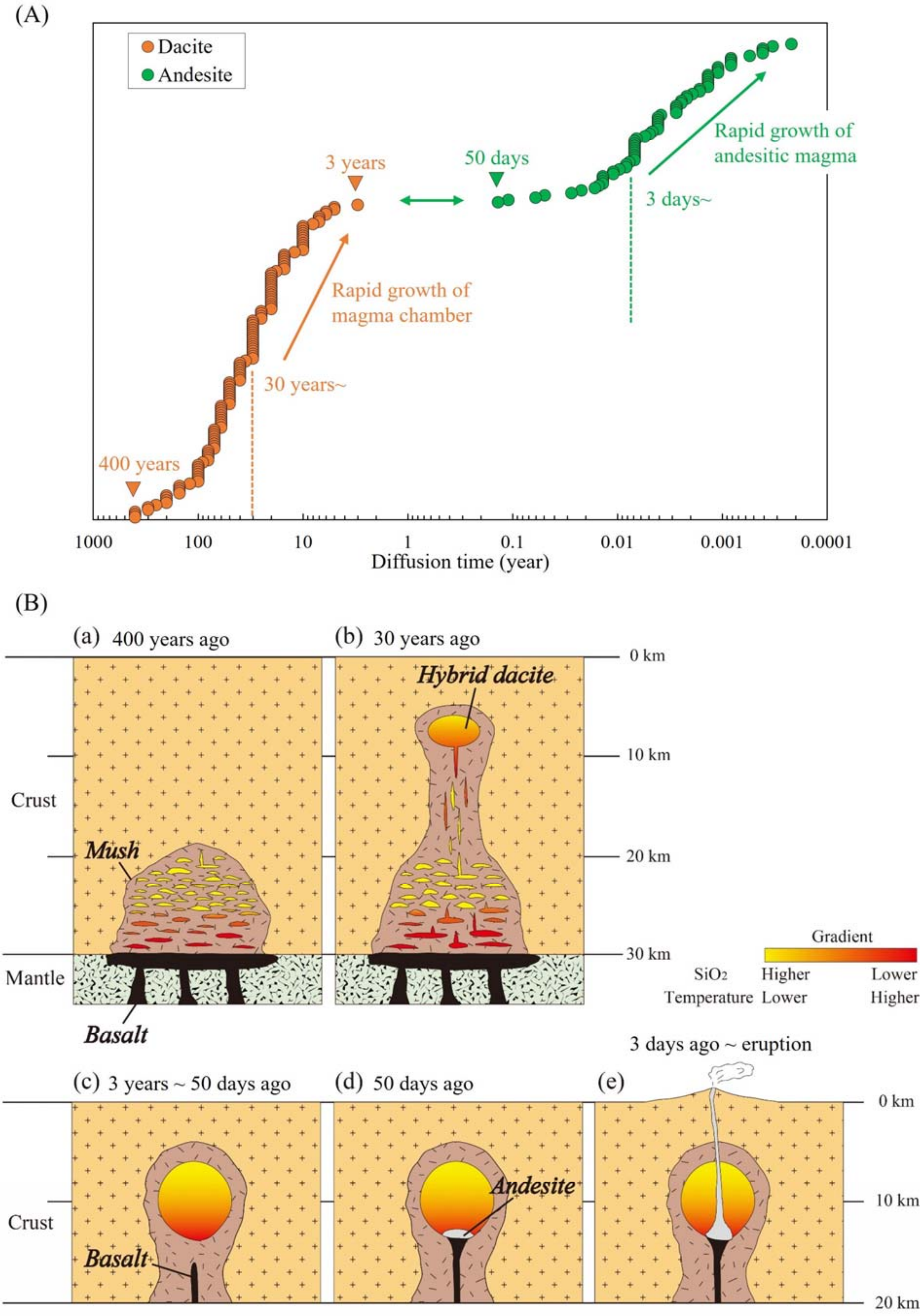
(A)
Dacite
Andesite
3 years
50 days
Rapid growth of andesitic magma
3 days~
Rapid growth of magma chamber
30 years~
400 years
1000
100
10
1
0.1
0.01
0.001
0.0001
Diffusion time (year)
(B)
(a) 400 years ago
(b) 30 years ago
0 km
Hybrid dacite
10 km
Crust
Mush
20 km
30 km
Mantle
Basalt
Gradient
SiO2 Higher Lower
Temperature Lower Higher
3 days ago ~ eruption
(c) 3 years ~ 50 days ago
(d) 50 days ago
(e)
0 km
Andesite
10 km
Crust
Basalt
20 km

Fig. 15. Time scales of magma plumbing system in the 1991 Pinatubo eruption. (A) Diffusion time of quartz in dacitic pumice and titano-magnetite in andesitic scoria. (B) Magma plumbing system with time scale. (a) 400 years before the 1991 eruption, heterogeneous silicic melts generated by the partial melting of crustal materials had begun the accumulation. (b) 30 years ago, dacitic magma chamber grew rapidly at shallow level. (c) More than 50 days before the eruption, basaltic magma ascent near the bottom of magma chamber. (d) At least 50 days ago, basaltic magma injected into magma chamber, and then magma mixing occurred, resulting in the generation of andesitic magma. (e) 3 days ago, andesitic magma grew rapidly with increased injection of basaltic magma, which led to the eruption June 12.

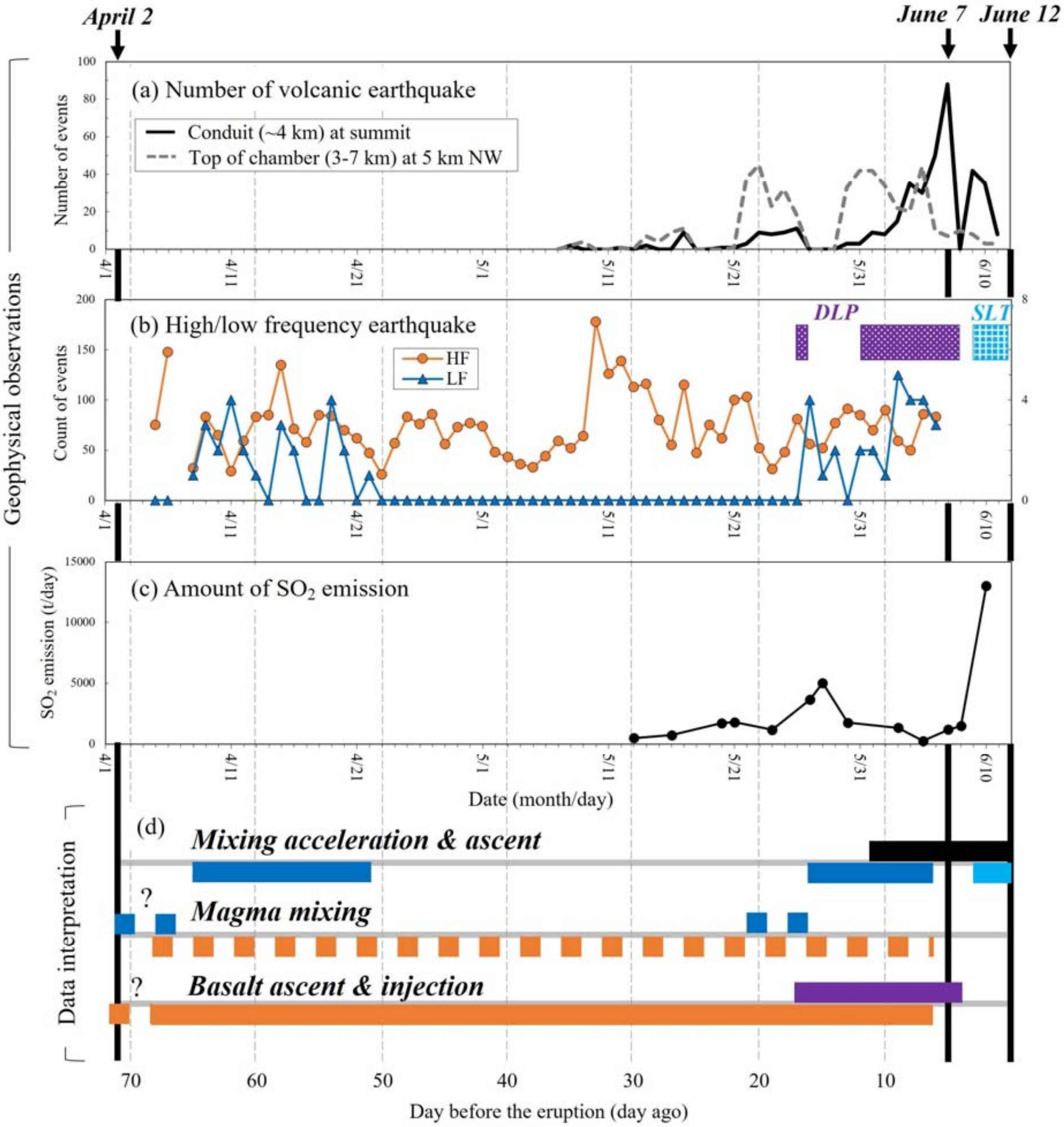

Fig. 16. Geophysical observations and its interpretation. (a) The number of earthquakes in the interior of volcano (below the summit to a depth of 4 km) and in the upper part of magma reservoir (5 km below the northwest to a depth of 3-7 km) (Mori et al., 1996; Zobin, 2018). (b) Transitions of high- and low-frequency (HF and LF) earthquakes (Sabit et al., 1996). The upper part shows when DLP (White, 1996) and swarms of shallow low-frequency tremor (SLT; Power et al., 1996) were observed. (c) Changes in SO_2 emissions measured by COSPEC (Daag et al., 1996). (d) Interpretation of geophysical data, and divided into three magmatic processes, basalt ascent and injection, magma mixing, and mixing acceleration and ascent. Each color indicates that the timing of magmatic process as estimated from the corresponding observed data.

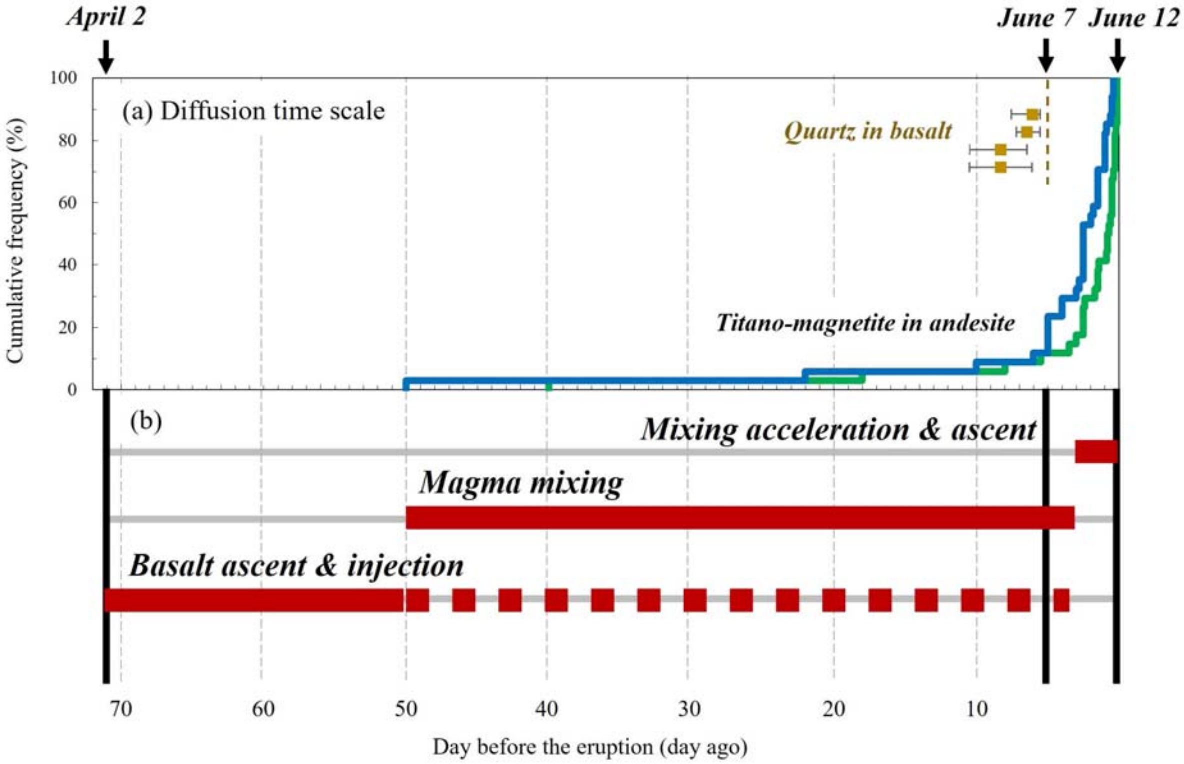

Fig. 17. Diffusional time scale and three magmatic processes. (a) Time scales were calculated from titano-magnetite in andesitic scoria and quartz in basaltic enclave. Green and blue lines show cumulative frequencies of diffusion times calculated by Ti and Al, respectively. (b) Three magma processes are basalt ascent and injection, magma mixing, and mixing acceleration and ascent.

Chapter 11: Conclusions

Diffusion profiles of phenocryst minerals (quartz and titano-magnetite) in juvenile material of the 1991 eruption of Pinatubo volcano were analyzed, and the following information was obtained.

1. Diffusion time of quartz in dacitic pumice shows a range of 3-400 years, and tends to be within 30 years, suggesting that the accumulation of silicic melts had already started 400 years before the eruption, and the magma chamber formed by them was completed 3 years before the eruption. Furthermore, the magma chamber may have grown rapidly after 30 years before the eruption. Thus, the magma chamber did not grow at a constant rate, whereas increased its growth rate in the later stages of the evolution process.
2. Diffusion time of titano-magnetite in andesitic scoria showed the range from 2 hours to 50 days and was concentrated within 3 days, suggesting that magma mixing had already started with the injection of basaltic magma 50 days before the eruption. In addition, magma mixing may have proceeded rapidly due to an increase in the supply of basaltic magma three days before the eruption, and andesitic magma may have grown rapidly. Thus, the supply of basaltic magma is not constant, but it seems to have increased rapidly 3 days before the eruption.
3. Based on the results of the diffusion profile, the time scale of the magma plumbing system of the 1991 Pinatubo eruption is as follows. Basaltic magma melted crustal materials and produced heterogeneous silicic melts before 400 years before the eruption. The silicic melts began to accumulate and form a shallow magma reservoir 400 years ago, which grew rapidly for 30 years and was completed 3 years ago. Up to 50 days before the eruption, basaltic magma injected into the bottom of the magma chamber and andesitic magma was generated by subsequent magma mixing. 3 days before the eruption, the magma mixing increased rapidly as the supply of basaltic magma increased, and the andesitic magma grew rapidly, leading to the first plinian eruption on 12 June.
4. Time scales of titano-magnetite were validated against the geophysical data recorded before the eruption. The results show that the rapid growth of andesitic magma from 3 days before the eruption is consistent with the swarm of shallow low-frequency tremors and the rapid increase in SO_2 emission. There is the possibility that we can estimate the precursor phenomena of eruption from the time scales of magmatic processes.

Part 3:

Concluding remarks

Concluding remarks

Pinatubo volcano has been active for about one million years, and seven silicic magmatic eruptions have occurred during the last 40,000 years (Newhall et al., 1996). Between 1991 and the previous active phase, the Buag period (0.5-1.0 ka), is only 500 years (Newhall et al., 1996). The time scale of the pre-eruptive process clarified in this study is only for the 1991 eruptive activity. Therefore, the relationship between the magma plumbing system and the pre-eruptive process in previous active periods is unknown. In contrast, we can clarify the long-term formation and evolution of the magma plumbing system of Pinatubo volcano by conducting the same study in the previous active period.

As mentioned in the ‘introduction’ of this dissertation, the decision criteria for new regulatory standards in nuclear power plants were established solely based on the research results of Druitt et al. (2012). To improve the reliability of the criteria, it is vital to accumulate case studies of large-scale volcanic eruptions of the past, such as the 1991 Pinatubo eruption, to clarify the formation and evolution processes of magma plumbing system and the time scales of their pre-eruptive processes. Therefore, it is desirable to study the time scale of the long-term pre-eruptive by investigating and organizing past eruption history in detail, rather than focusing on only one active period. This will make it possible to extract volcanoes with a high level of danger. It is essential to strengthen the monitoring of high-risk volcanoes and start monitoring them promptly. As pointed out in this study, monitoring on the order of at least several decades is necessary to observe the precursor phenomena of large-scale eruptions (Druitt et al., 2012). Therefore, it is important to conduct continuous geophysical observations and accumulate observational data hereon. This will enable us to understand the precursor phenomena of large-scale eruptions and predict eruptions in the future.

Acknowledgements

We are grateful to John Pallister, Cascades Volcano Observatory, United States Geological Survey, United States of America, and Takehiro Koyaguchi, Earthquake Research Institute, the University of Tokyo, Japan, for providing us many samples of Pinatubo 1991 eruption, to Mizuho Amma-Miyasaka for supporting preparing our whole analyses, to Akiko Matsumoto for supporting our XRF and EPMA analyses, and to Hidehiko Nomura and Kousuke Nakamura for preparing the thin sections. We also thank Hirohito Inakura and Yoshiyuki Horikawa, West Japan Engineering Consultants, Inc, for their many advice and support.

Appendix A. Method for studying the compositional profile of quartz.

Although the quantitative analysis by FE-EPMA can accurately measure the amount of Ti in quartz, the compositional profile can only be obtained at intervals of a few to 10 μm or more due to irradiation damage. Therefore, we took cathodoluminescence (CL) images and estimated the compositional profile of quartz from the relationship between the gray scale obtained from the CL images and the amount of Ti actually analyzed. First, CL images of arbitrary quartz speckles were taken and the amount of Ti was quantitatively analyzed at several points (Fig. A1a). The CL images were then converted to grayscale. Image J (developed by the National Institute of Health (NIH)) was used for the conversion. Then, the converted grayscale was compared with the measured Ti content (Fig. A1b), and the relationship between the two was read visually to obtain a linear approximation formula (Fig. A1c). The amount of Ti was estimated from the CL image using this approximation formula (Table A1). The difference between the measured Ti content and the estimated Ti content was generally less than 10% (Table A1).

The moving average method was used to correct (smooth out) the noise (variation) that occurred when the gray scale was converted to numerical values (Figure A1d). The numerical values used in calculating the moving average were determined to be the previous three values after trial and error.

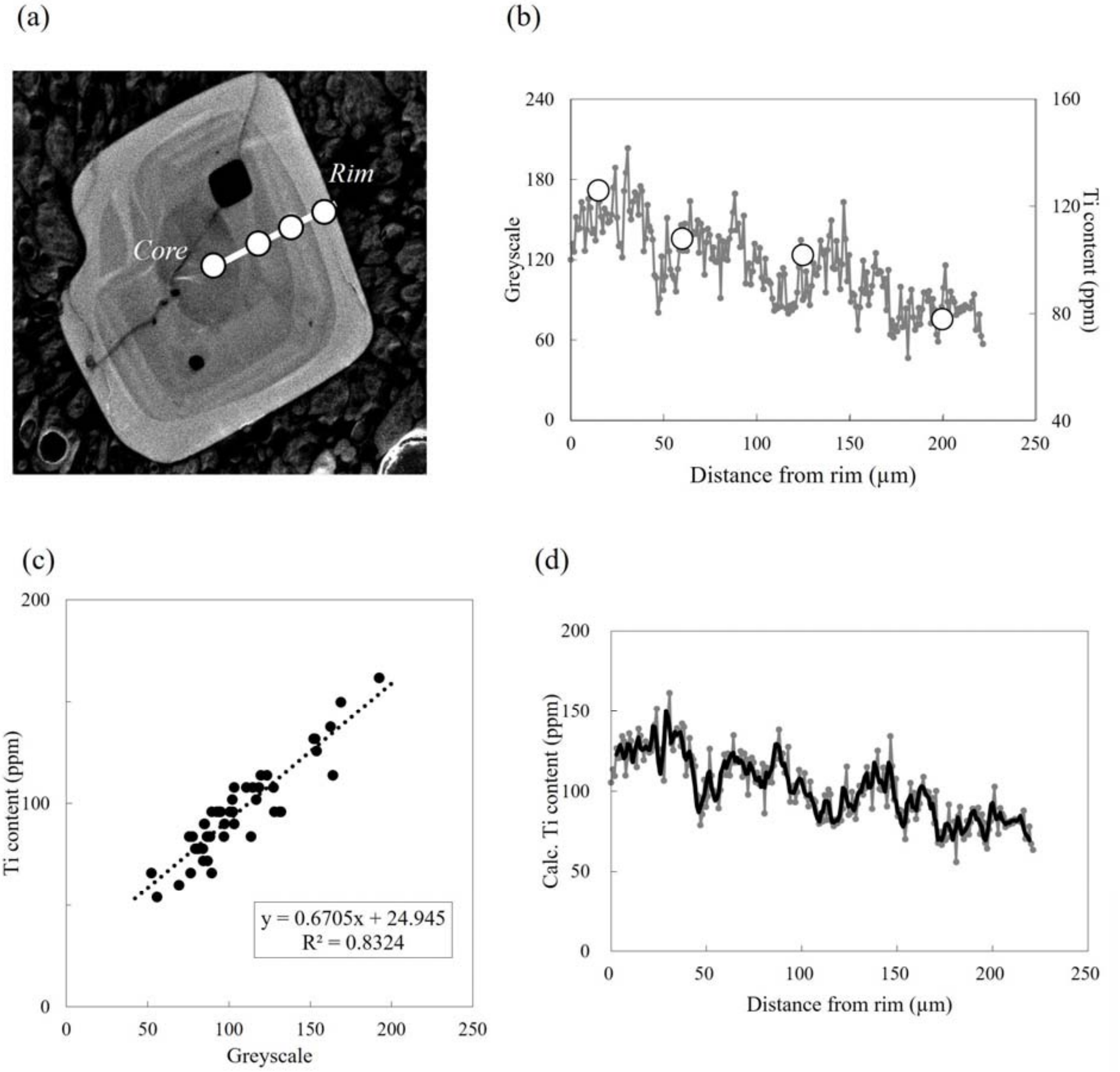

Fig. A1. Steps involved in creating a compositional profile of quartz. (a) Cathodoluminescence image of quartz and the location where the composition profile is to be estimated (white line) and the location where the amount of Ti is quantified (white circle). (b) Comparison of the grayscale composition profile and the quantified Ti content (white circle). (c) Comparison of grayscale and Ti content and linear approximation equation. (d) Moving average of the original composition profile (gray line) with noise removed (black line).

Table A1. Representative Ti contents of quartz in dacitic pumice and basaltic enclave.

Unit	Sample name	Grain name	Data							
J7-E	P22892-1A	1A-2-3	Point[*1]	Core	m1	m2	m3	m4	Rim	
			Measured[*2]	90	60	66	84	72	162	
			Calculated[*3]	94	71	76	90	81	154	
			Residue[*4]	-4 (5)	-11 (19)	-10 (15)	-6 (7)	-9 (13)	8 (5)	
J15-R	0801C-K	0801L-1	Point	Core	m1	m2	Rim			
			Measured	78	102	108	126			
			Calculated	81	103	110	128			
			Residue	-3 (4)	-1 (1)	-2 (2)	-2 (2)			
J15-R	0801C-O	0801H-3	Point	Core	m1	m2	m3	m4	m5	Rim
			Measured	96	78	84	78	108	84	114
			Calculated	92	79	84	79	102	83	108
			Residue	4 (4)	-1 (2)	0 (0)	-1 (2)	6 (6)	1 (1)	6 (6)

Unit of Ti contents is ppm.

[*1] Data location. "m1, m2, ..." show the location between core and rim.

[*2] Analytical data measured by FE-EPMA.

[*3] Estimated data calculated by the relationship between greyscale of CL image and Ti content (see text in Appendix A for detail).

[*4] Residual value (= Measured - Calculated). Residual ratio is shown in parenthesis (Residue/Measured; %).

Appendix B. Calculation of diffusion time of quartz.

In order to calculate the diffusion time of quartz, we first calculated the diffusion coefficient using the method of Cherniak et al. (2007). Assuming that the compositional profile of quartz is parallel to the c-axis, the diffusion time can be calculated from the Arrhenius:

$$D_{Ti}=7\times\exp(-237/RT)$$

where D_{Ti}: diffusion coefficient of Ti in quartz, R: gas constant, and T: temperature (in Kelvin). The temperature is assumed to be constant while diffusion is in progress, and the equilibrium thermometer with iron-titanium oxides (Anderson and Lindsley, 1988) is used for quartz from dacitic pumice, and the equilibrium temperature of colored minerals (Pallister et al., 1996) is used for quartz from basaltic inclusions to obtained (Table B1). In this study, a one-dimensional diffusion model was applied and the infinite equation given by Costa and Morgan (2010):

$$C_{(X,\ t)}=C_0+(C_1-C_0)/2\times\mathrm{erfc}\left(X/2\sqrt{D\times t}\right)$$

where $C_{(x,t)}$: composition at point X at some time t, C_1: composition of the core, C_0: composition of the rim, D: diffusion coefficient, t: diffusion time, erfc: complementary error function. The diffusion time was taken as the value when the composition profile (at a certain time t) drawn by the infinite equation and the composition profile obtained by the actual analysis overlapped the most. The overlap of the compositional profiles was selected visually by trial and error (Fig. B1). The analysis of the diffusion profile is applied assuming that it is parallel to the c-axis, but the difference in diffusion rate between parallel and perpendicular to the c-axis is less than 5% (Matthews et al., 2012). The directionality of the crystal axis is not considered in this study because this has a smaller effect on the diffusion time than the magma temperature error.

The cumulative change in the estimated diffusion time is shown in Fig. B2 (see supplementary materials for the values of diffusion times). This figure shows the error for the maximum and minimum temperature estimates, although the average magma temperature is used in the text. For the maximum temperature, the diffusion time tends to be short overall, resulting in a minimum of one year. On the contrary, for the minimum temperature, the diffusion time tends to be longer, resulting in a maximum of 900 years.

Table B1. Assumption of magma temperature for the calculation of quartz diffusion times.

Rock type	Value	Temperature (˚C)	Method	Reference	Diffusion rate (μm^2/s)[*1]
Dacite	Average	791	Fe-Ti oxide thermometry	Tamurra and Nakagawa (in press)	2.79×10^{-9}
	Maximum	824	Average absolute deviation[*2]	Blundy and Cashman (2008)	7.05×10^{-9}
	Minimum	758	Average absolute deviation[*2]	Blundy and Cashman (2008)	1.04×10^{-9}
Basalt[*3]	Average	1,200	Olivine-augite cotectic temperature	Rutherford et al. (1993)	1.46×10^{-5}
	Maximum	1,260	Olivine with Fo88 crystallization	Neilsen (1990)	3.50×10^{-5}
	Minimum	1,170	Clinopyroxene with Mg#85 crystallization	Neilsen (1990)	9.21×10^{-6}

[*1] Diffusion rate was calculated by the method of Cherniak et al. (2007).

[*2] Difference between geochemical and experimental methods, which shows in Blundy and Cashman (2008).

[*3] Temperatures of basalt were discussed in Pallister et al. (1996).

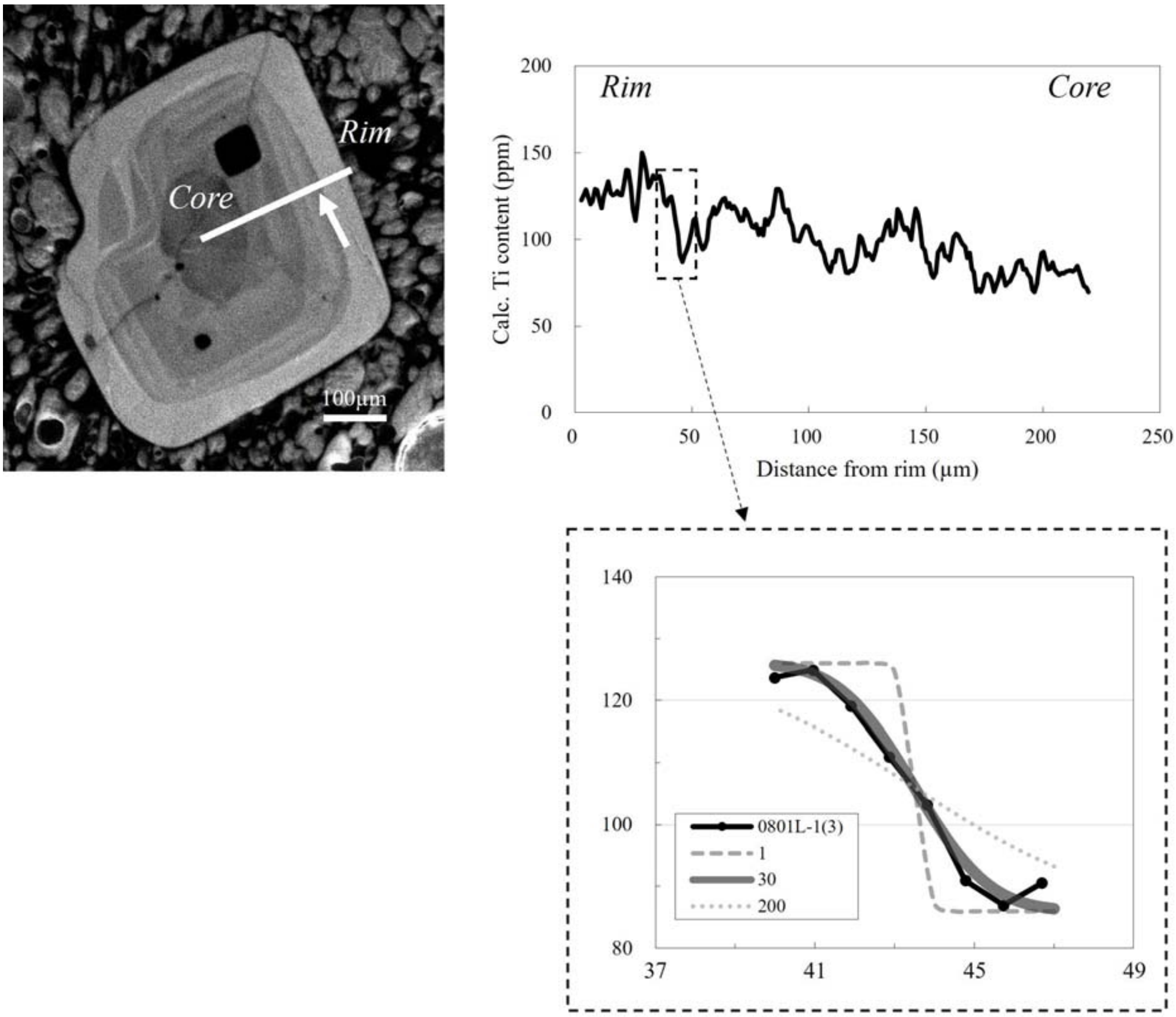

Fig. B1. An example of how to estimate the diffusion time from the diffusion profile of quartz. For each diffusion profile, the diffusion time is adjusted so that it overlaps with the profile well. The overlap was selected by visual inspection.

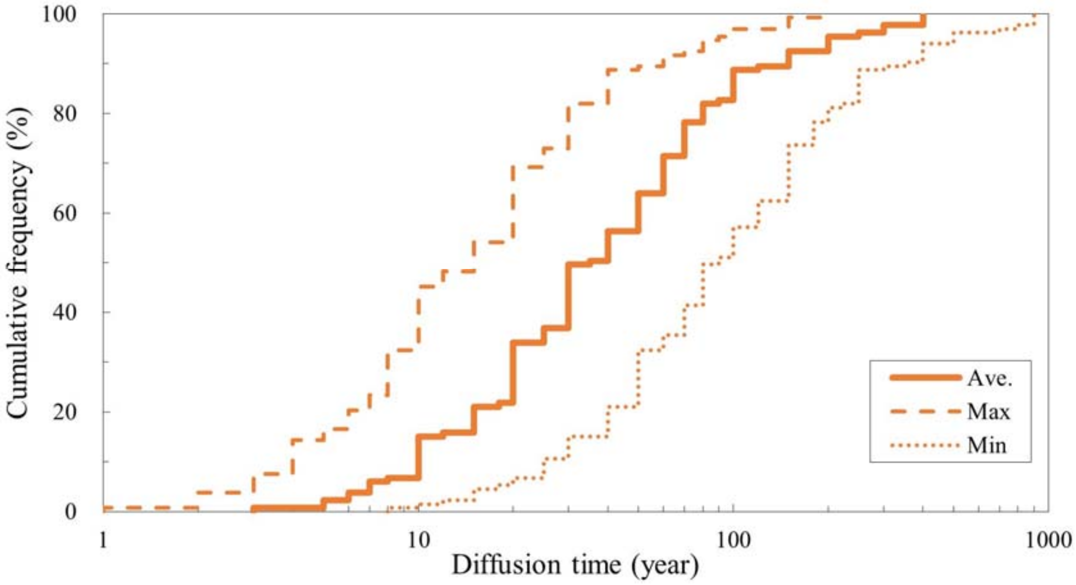

Fig. B2. Cumulative frequency of diffusion time and its error estimated from quartz in dacitic pumice. Error for calculation of diffusion time is due to one in the formula for magmatic temperature (±33℃; Blundy and Cashman, 2008).

Appendix C. Calculation of diffusion time of titano-magnetite.

Before analyzing the diffusion profile of titano-magnetite, it is necessary to distinguish whether the zoning structure of titano-magnetite rim is formed by crystal growth or by the effect of elemental diffusion (Tomiya et al., 2013). Reverse zoning structure exhibited by titano-magnetite in andesitic scoria shows different positions of compositional change for different elements, with TiO_2 and Al_2O_3 showing similar changes (~10-20 µm inward from the rim), whereas MgO changes further to the core (~30 µm inward from the rim) (Fig. C1a). In the case of simple crystal growth, the compositional changes of elements are all at the same position, so it can be concluded that the reverse zoning structure of titano-magnetite was formed by elemental diffusion. On the other hand, there are crystals in which the composition changes further out than zoning structure (Fig. C1b). Such crystals were excluded from the study of the diffusion profile because they were affected by crystal growth.

The equilibrium temperature of iron-titanium oxides (Andersen and Lindsley, 1988) was used as the temperature of the magma for calculating the diffusion time (Table C1). The calculated temperatures ranged from 919 to 1,081 °C, with an average value of 988°C. The average value was higher than that of previous studies (930°C). Although the mean value agrees with the results of previous studies (930-961°C; Pallister et al., 1996) within the error range (±33°C; Blundy and Cashman, 2008), the diffusion time calculated from the maximum and minimum temperature values is shown as the error because of the large range of temperature variation.

Diffusion times for titano-magnetite were calculated using the method of Crank (1975), which considers crystals as isotropic spheres and assumes that the core is homogeneous in composition. Titano-magnetite crystals can be approximated as isotropic spheres, as proposed by Crank (1975) (e.g., Tomiya et al., 2013; Matsumoto et al., 2018). A practical way to calculate the diffusion time is to use the semi-infinite formula presented in Costa and Morgan (2010):

$$C_{(X,\ t)}=C_0+(C_1-C_0)\times\mathrm{erf}\left(X/\sqrt{D\times t}\right)$$

where $C_{(x,\,t)}$: composition at point X at some time t, C_1: composition of the core, C_0: composition of the rim, D: diffusion coefficient, t: diffusion time, erf: error function. Diffusion coefficients were calculated using the diffusion rates and equations of Van Orman and Crispin (2010), with

$D_{Ti} = 4.58 \times 10^{-4}$ [$\mu m^2/s$] and $D_{Al} = 1.84 \times 10^{-4}$ [$\mu m^2/s$] for the average magma temperature (Table C2). The diffusion time was adopted at the time when the compositional profiles drawn by the semi-infinite equation (at a certain time t) and those obtained by the actual analysis overlapped the most. This is a commonly used method in existing studies (e.g., Masubuchi and Ishizaki, 2011; Tomiya et al., 2013; Matsumoto et al., 2018). The overlap of the compositional profiles was selected visually by trial and error (Fig. C2).

The cumulative frequency of diffusion time is shown in Fig. C3 (see supplementary materials for the values of diffusion times). This figure shows the error for the maximum and minimum temperature estimates, although the average magmatic temperature is used in the text. For the maximum temperature, the diffusion time tends to be short overall, resulting in a minimum of 0.02 days (0.5 hours). On the contrary, for the minimum temperature, the diffusion time tends to be longer, resulting in a maximum of 120 days.

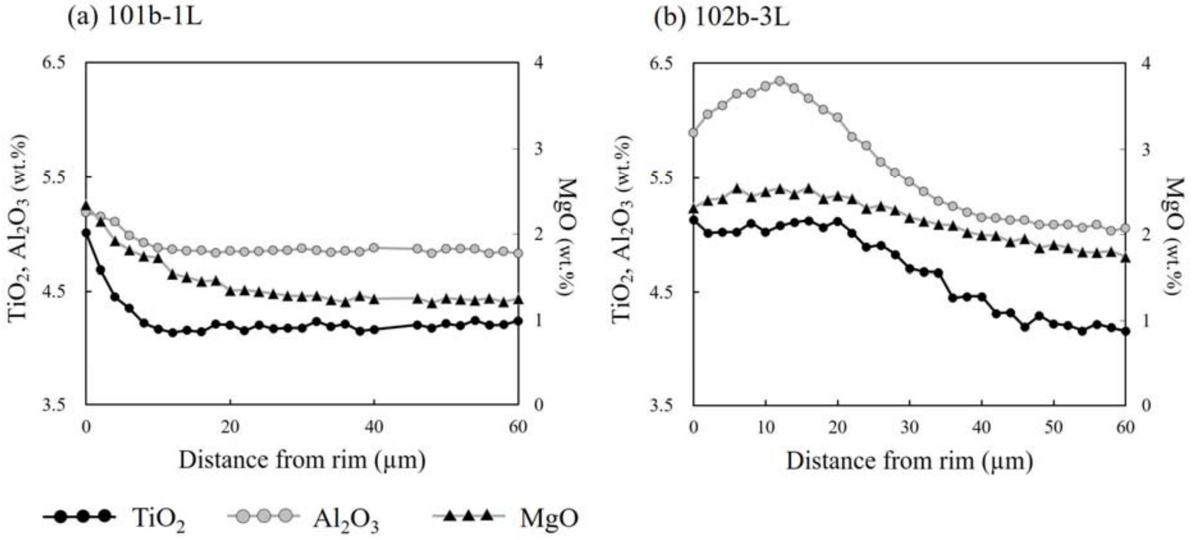

Fig. C1. Example for compositional profiles of titano-magnetite in andesitic scoria. (a) Locations of compositional changes are different for each element. (b) Compositions change at outer rim. Because the location of the compositional change is the same for all the elements, it can be concluded that the compositional change of the rim was formed by crystal growth.

Table C1. Representative chemical compositions of titano-magnetite-ilmenite pair in andesitic scoria.

Sample name	P-3ox-17m	P-3ox-17i-r	L60-2ox-5L	L63-2ox-5L	L14-2ox-1L	L15-2ox-1L	L55-2ox-1L	L53-2ox-1L	L8-2ox-5L	L9-2ox-5L
Mineral	Mt	Ilm	Mt	Ilm	Mt	Ilm	Mt	Ilm	Mt	Ilm
Point	Rim	Rim	Rim	Rim	Rim	Rim	Rim	Rim	Rim	Rim
SiO_2	0.06	0.05	0.12	0.18	0.11	0.03	0.15	0.04	0.16	0.06
TiO_2	7.79	30.64	8.60	29.90	9.72	32.37	10.59	31.87	12.00	30.29
Al_2O_3	2.10	0.40	1.98	0.47	2.80	0.78	2.71	0.45	1.63	0.43
FeO^{t}[*1]	82.36	63.41	79.80	61.38	78.47	58.78	75.64	59.78	76.54	61.87
MnO	0.61	0.29	0.61	0.30	0.77	0.59	0.71	0.43	0.55	0.28
MgO	2.15	1.76	2.39	2.01	2.36	2.66	2.50	1.77	2.21	1.90
CaO	0.02	0.01	0.04	0.03	0.04	0.02	0.02	n.d.	0.05	0.05
Na_2O	n.d.	0.03	0.00	n.d.	n.d.	0.01	n.d.	n.d.	n.d.	0.02
Cr_2O_3	0.15	0.08	0.07	0.09	0.10	0.05	0.08	0.07	0.10	0.10
NiO	0.03	0.02	n.d.	0.02	0.01	0.02	0.02	n.d.	0.05	n.d.
Total	95.26	96.68	93.62	94.37	94.38	95.31	92.42	94.41	93.28	95.01
X_{usp}[*2]	0.22	-	0.24	-	0.28	-	0.32	-	0.35	-
X_{ilm}[*2]	-	0.57	-	0.57	-	0.60	-	0.61	-	0.57
Temp.[*3]	919		947		973		1,004		1,081	

Unit of compositions is wt.%.

[*1] Total Fe is expressed as FeOt.

[*2] Ferric-ferrous ratio and mole fractions of ulvöspinel and ilmenite were calculated by the method of Stormer (1983).

[*3] Magmatic temperatures were calculated by the method of Andersen and Lindsley (1988).

Abbreviations: Mt = titano-magnetite, Ilm = ilmenite, n.d. = not detected.

Table C2. Assumption of magma temperature for the calculation of titano-magnetite diffusion times.

Rock type	Value	Temperature (˚C)[*1]	Method	Element	Diffusion rate ($\mu m^2/s$)[*2]
Andesite	Average	988	Average value of andesitic temperature	Ti	4.58×10^{-4}
				Al	1.84×10^{-4}
	Maximum	1,081	Maximum value of andesitic temperature	Ti	1.20×10^{-3}
				Al	6.32×10^{-4}
	Minimum	919	Minimum value of andesitic temperature	Ti	2.32×10^{-4}
				Al	7.37×10^{-5}

[*1] Temperature of andesitic magma was calculated by the method of Fe-Ti oxide thermometry in Andersen and Lindsely (1988).

[*2] Diffusion rate was calculated by diffusion velocity and the equation in Van Orman and Crispin (2010).

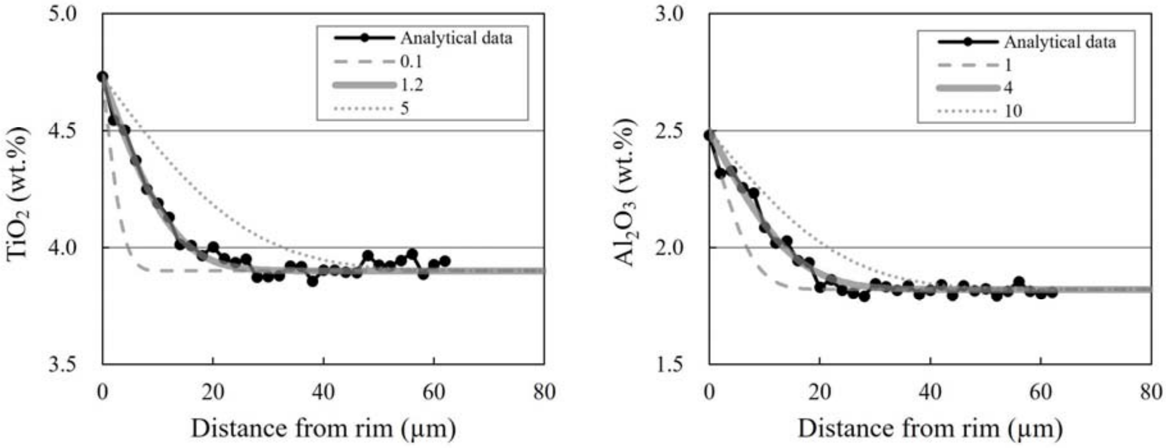

Fig. C2. An example of how to estimate the diffusion time from the diffusion profile of titano-magnetite. For each diffusion profile, the diffusion time is adjusted so that it overlaps with the profile well. The overlap was selected by visual inspection.

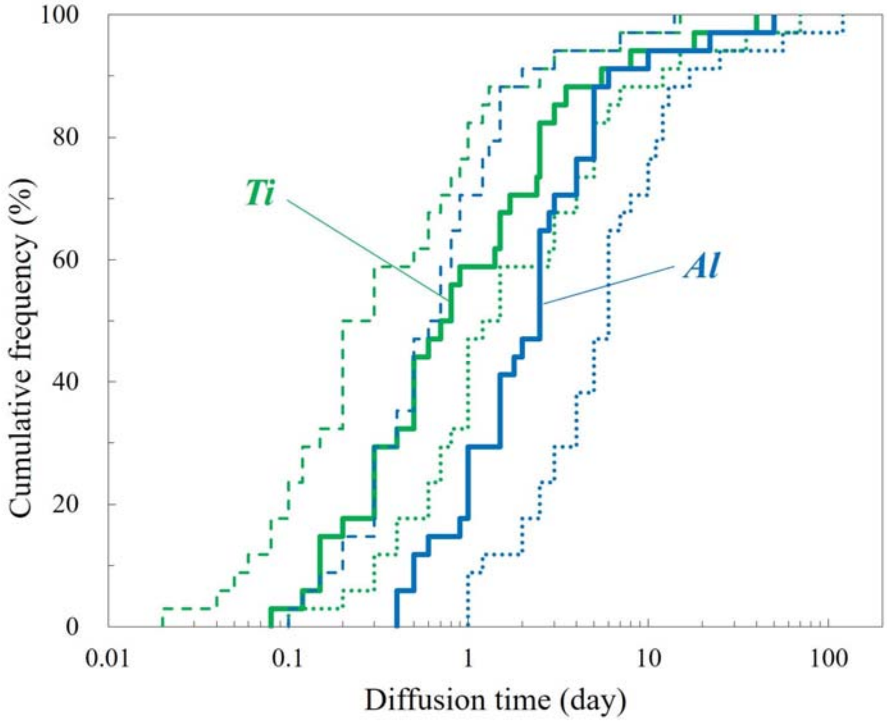

Fig. C3. Cumulative frequency of diffusion time and its error estimated from titano-magnetite in andesitic scoria. Because temperature variation of andesitic magma is larger than the error in the formula for magma temperature, this error was estimated from the maximum and minimum temperature variation.

Supplementary Materials

Part1:

Table S1. Representative chemical compositions (wt.%; n.d., not detected) of phenocrysts in dacitic samples.

Table S2. Representative chemical compositions (wt.%; n.d., not detected) of phenocrysts in andesitic samples.

Table S3. Representative chemical compositions (wt.%; n.d., not detected) of phenocrysts in basaltic sample.

Table S4. Whole-rock major (wt.%) and trace elements (ppm), and isotopic compositions of representative 1991 samples.

Table S5. Magmatic temperature (°C) of the 1991 dacitic magma (major element concentrations in wt.%; n.d., not detected) based on magnetite-ilmenite pair geothermometer.

Table S6. Whole-rock major element and mineral compositions (wt.%) for mass balance calculation.

Part2:

Table S7. Representative chemical compositions of titano-magnetite in andesitic scoria and dacitic pumice.

Table S8. Representative diffusion time and adapted parameters of two type rims in quartz.

Table S9. Representative diffusion time estimated by Ti and Al contents of titano-magnetite in andesitic scoria.

Table S1. Representative chemical compositions (wt.%; n.d., not detected) of phenocrysts in dacitic samples.

Phenocryst	Plagioclase		Plagioclase		Plagioclase		Plagioclase		Plagioclase		Plagioclase	
Unit	J15-R		J15-R		J15-R		J15-P		J15-P		J15-P	
Sample name	02C-B1-1	02C-B1-1r	02C-B1-2	02C-B1-2r	02C-B1-6	02C-B1-6r	B2-2Pl-2	B2-2Pl-2r	B2-2Pl-3	B2-2Pl-3r	B2-2Pl-10	B2-2Pl-10r
Point	Core	Rim	Core	Rim	Core	Rim	Core	Rim	Core	Rim	Core	Rim
SiO_2	57.46	59.31	57.21	60.72	62.06	58.77	59.18	59.68	59.97	60.36	58.76	56.33
TiO_2	-	-	-	-	-	-	-	-	-	-	-	-
Al_2O_3	27.01	26.60	27.67	25.06	24.27	26.28	25.91	24.65	25.06	24.87	24.73	26.58
FeO^{t*1}	0.24	0.15	0.17	0.17	0.16	0.21	0.14	0.13	0.17	0.13	0.13	0.14
MnO	-	-	-	-	-	-	-	-	-	-	-	-
MgO	< 0.01	0.01	0.01	0.01	0.01	0.01	< 0.01	0.01	0.02	n.d.	n.d.	< 0.01
CaO	9.70	8.70	10.18	7.49	6.19	8.73	7.98	6.99	7.39	7.13	7.29	9.60
Na_2O	5.95	6.62	5.71	7.14	7.85	6.56	6.90	7.43	7.16	7.47	7.33	6.18
K_2O	0.21	0.28	0.20	0.35	0.40	0.26	0.27	0.32	0.30	0.36	0.34	0.22
Cr_2O_3	-	-	-	-	-	-	-	-	-	-	-	-
NiO	-	-	-	-	-	-	-	-	-	-	-	-
Total	100.56	101.68	101.14	100.93	100.91	100.82	100.40	99.20	100.07	100.33	98.59	99.04
An#^{*2}	46.8	41.4	49.1	36.0	29.6	41.8	38.4	33.6	35.7	33.8	34.8	45.6
Si^{*3}	-	-	-	-	-	-	-	-	-	-	-	-
$(Na+K)_A{}^{*3}$	-	-	-	-	-	-	-	-	-	-	-	-
Mg/Mn	-	-	-	-	-	-	-	-	-	-	-	-
Mg#^{*4}	-	-	-	-	-	-	-	-	-	-	-	-

(continued)

Phenocryst	Amphibole (Hornblende)		Amphibole (Hornblende)		Amphibole (Hornblende)		Amphibole (Hornblende)		Amphibole (Hornblende)		Amphibole (Hornblende)	
Unit	J15-R		J15-R		J15-R		J15-P		J15-P		J15-P	
Sample name	02C-B1hy-6	02C-B1hy-6r	02C-B1hy-8	02C-B1hy-8r	02C-B1Hy-4	02C-B1Hy-4r	B2-2Hy-1	B2-2Hy-1r	M2-2Hy-1	M2-2Hy-1r	M2-2Hy2-1	M2-2Hy2-1r
Point	Core	Rim	Core	Rim	Core	Rim	Core	Rim	Core	Rim	Core	Rim
SiO_2	47.73	47.43	48.49	49.90	48.20	49.97	49.90	49.82	48.68	48.73	47.41	46.00
TiO_2	1.17	1.02	0.95	0.90	1.01	0.95	0.84	0.87	1.17	0.96	0.94	1.37
Al_2O_3	8.30	8.32	8.25	6.69	8.43	7.19	7.39	7.58	7.89	7.89	8.92	9.60
FeO^{t*1}	12.73	12.46	12.95	11.78	13.21	11.82	12.96	12.70	13.13	12.58	13.62	13.74
MnO	0.49	0.50	0.51	0.46	0.52	0.42	0.49	0.52	0.51	0.47	0.50	0.51
MgO	15.49	15.54	15.21	16.35	15.01	16.42	15.52	15.71	15.16	15.78	14.25	13.84
CaO	10.70	10.41	10.70	10.65	10.73	10.55	10.64	10.51	10.60	10.59	10.73	10.78
Na_2O	1.43	1.49	1.43	1.19	1.48	1.29	1.28	1.30	1.41	1.37	1.56	1.71
K_2O	0.25	0.31	0.31	0.21	0.37	0.22	0.30	0.27	0.26	0.29	0.42	0.42
Cr_2O_3	0.01	0.02	0.01	n.d.	0.01	0.02	0.01	0.03	0.03	n.d.	n.d.	n.d.
NiO	-	-	-	-	-	-	-	-	-	-	-	-
Total	98.29	97.50	98.80	98.12	98.96	98.87	99.32	99.31	98.84	98.65	98.35	97.97
$An\#^{*2}$	-	-	-	-	-	-	-	-	-	-	-	-
Si^{*3}	6.71	6.70	6.79	6.97	6.76	6.92	6.93	6.90	6.81	6.80	6.72	6.58
$(Na+K)_A{}^{*3}$	0.04	0.06	0.06	0.04	0.08	0.04	0.05	0.05	0.05	0.05	0.13	0.20
Mg/Mn	-	-	-	-	-	-	-	-	-	-	-	-
$Mg\#^{*4}$	-	-	-	-	-	-	-	-	-	-	-	-

(continued)

Phenocryst	Titano-magnetite		Titano-magnetite		Titano-magnetite		Biotite		Biotite	
Unit	J15-R		J15-R		J15-P		J15-R		J15-R	
Sample name	02CB1-7	02CB1-7r	02CB1-5-2	02CB1-5-3	M2-2ox-1	M2-2ox-1r	M-1-5	M-1-5r	Bt-b-1	Bt-b-1r
Point	Core	Rim	Core	Rim	Core	Rim	Core	Rim	Core	Rim
SiO_2	0.06	0.06	0.06	0.07	0.04	0.03	38.50	38.56	38.73	38.56
TiO_2	4.32	4.17	4.26	4.20	4.26	4.23	3.27	3.28	3.35	3.28
Al_2O_3	1.98	1.97	1.92	1.96	1.90	1.86	14.54	14.46	14.75	14.46
FeO^{t*1}	85.84	85.25	85.19	84.57	84.97	85.43	13.57	13.07	12.78	13.07
MnO	0.45	0.45	0.44	0.43	0.46	0.48	0.14	0.09	0.10	0.09
MgO	1.13	1.08	1.08	1.15	1.12	1.20	16.07	16.26	16.33	16.26
CaO	0.02	0.09	0.01	0.02	< 0.01	0.01	n.d.	n.d.	0.01	n.d.
Na_2O	0.01	0.01	0.03	n.d.	0.04	0.02	0.79	0.78	0.77	0.78
K_2O	-	-	-	-	-	-	9.09	9.03	8.97	9.03
Cr_2O_3	0.20	0.19	0.23	0.23	0.22	0.19	0.02	0.02	0.01	0.02
NiO	0.03	0.07	0.03	0.04	0.04	0.04	-	-	-	-
Total	94.05	93.34	93.23	92.67	93.04	93.49	95.98	95.54	95.78	95.54
An#[*2]	-	-	-	-	-	-	-	-	-	-
Si[*3]	-	-	-	-	-	-	-	-	-	-
$(Na+K)_A$[*3]	-	-	-	-	-	-	-	-	-	-
Mg/Mn	4.45	4.21	2.20	2.36	4.32	4.38	-	-	-	-
Mg#[*4]	-	-	-	-	-	-	67.9	68.9	69.5	68.9

[*1] Total Fe is expressed as FeOt. [*2] An# is reported in mol.%. [*3] Units of Si and $(Na + K)_A$ are per formula unit. [*4] Mg# is reported in mol.%.

Table S2. Representative chemical compositions (wt.%; n.d., not detected) of phenocrysts in andesitic samples.

Phenocryst	Plagioclase		Plagioclase		Plagioclase		Plagioclase		Plagioclase	
Unit	J7-L		J7-L		J7-L		J12-S		J12-S	
Sample name	CN-Pl2-18	CN-Pl2-18r	CN-Pl2-19	CN-Pl2-19r	CN-3	CN-3r	P3-Pl-5	P3-Pl-5r	P3-Pl-6	P3-Pl-6r
Point	Core	Rim	Core	Rim	Core	Rim	Core	Rim	Core	Rim
SiO_2	53.50	60.54	53.10	52.39	61.46	53.45	60.20	54.48	59.93	52.27
TiO_2	-	-	-	-	-	-	-	-	-	-
Al_2O_3	29.83	24.68	29.38	29.76	24.62	29.65	24.42	27.75	24.18	29.13
FeO^{t*1}	0.25	0.16	0.50	0.53	0.14	0.54	0.17	0.49	0.13	0.55
MnO	-	-	-	-	-	-	-	-	-	-
MgO	0.01	n.d.	0.05	0.07	n.d.	0.07	0.01	0.05	n.d.	0.07
CaO	12.42	6.81	12.49	12.96	6.85	12.78	6.38	10.71	6.17	12.64
Na_2O	4.60	7.69	4.29	4.21	7.50	4.05	7.93	5.53	8.15	4.58
K_2O	0.12	0.41	0.29	0.16	0.38	0.17	0.36	0.25	0.36	0.16
Cr_2O_3	-	-	-	-	-	-	-	-	-	-
NiO	-	-	-	-	-	-	-	-	-	-
Total	100.72	100.28	100.09	100.06	100.96	100.71	99.46	99.27	98.93	99.37
An#[*2]	59.4	32.1	60.6	62.4	32.8	62.9	30.2	51.0	28.9	59.8
Si[*3]	-	-	-	-	-	-	-	-	-	-
$(Na+K)_A$[*3]	-	-	-	-	-	-	-	-	-	-
Mg/Mn	-	-	-	-	-	-	-	-	-	-
Mg#[*4]	-	-	-	-	-	-	-	-	-	-

(continued)

Phenocryst	Amphibole (Pargasite)		Amphibole (Pargasite)		Amphibole (Pargasite)		Amphibole (Pargasite)		Amphibole (Pargasite)	
Unit	J7-L		J7-L		J7-L		J12-S		J12-S	
Sample name	CN-Hy2-2	CN-Hy2-2r	CN-Hy2-6	CN-Hy2-6r	CN-Hy-23	CN-Hy-23r	S2-3Hy-5	S2-3Hy-5r	S2-3Hy-8	S2-3Hy-8r
Point	Core	Rim	Core	Rim	Core	Rim	Core	Rim	Core	Rim
SiO_2	40.98	41.52	39.71	41.81	43.23	42.43	43.09	41.87	42.46	43.41
TiO_2	2.01	1.98	2.45	1.97	2.13	1.85	1.84	1.72	1.88	1.57
Al_2O_3	12.72	11.69	13.13	12.48	12.43	13.04	12.61	13.13	12.04	11.79
FeO^{t*1}	10.24	11.03	10.54	13.40	10.24	12.33	10.65	14.22	10.64	12.82
MnO	0.12	0.14	0.10	0.18	0.12	0.15	0.13	0.26	0.15	0.26
MgO	15.25	14.74	15.00	13.43	15.42	13.63	14.91	12.22	15.17	13.58
CaO	11.96	11.63	11.80	11.64	11.64	11.66	11.78	11.92	11.81	11.54
Na_2O	2.41	2.48	2.39	2.38	2.43	2.47	2.45	2.29	2.37	2.22
K_2O	0.84	0.74	0.98	0.68	0.90	0.81	0.80	0.75	0.70	0.64
Cr_2O_3	n.d.	n.d.	n.d.	n.d.	0.03	n.d.	0.02	n.d.	0.10	0.01
NiO	-	-	-	-	-	-	-	-	-	-
Total	96.53	95.95	96.09	97.96	98.56	98.35	98.28	98.37	97.31	97.82
An#[*2]	-	-	-	-	-	-	-	-	-	-
Si[*3]	5.99	6.13	5.85	6.08	6.17	6.13	6.18	6.12	6.15	6.29
$(Na+K)_A$[*3]	0.71	0.69	0.73	0.61	0.61	0.65	0.64	0.66	0.63	0.53
Mg/Mn	-	-	-	-	-	-	-	-	-	-
Mg#[*4]	-	-	-	-	-	-	-	-	-	-

(continued)

Phenocryst	Titano-magnetite		Titano-magnetite		Titano-magnetite		Olivine	Olivine	Clinopyroxene		Clinopyroxene	
Unit	J7-L		J12-S		J12-S		J7-L	J12-S	J7-L		J12-S	
Sample name	CN-Ox-5	CN-Ox-5r	M2-3ox-2	M2-3ox-2r	P-3ox-1	P-3ox-1r	CN-Mf2-2	P3-Mf-21	CN-Mf2-4	CN-Mf2-4r	P3-Mf-28	P3-Mf-28r
Point	Core	Rim	Core	Rim	Core	Rim	Core	Core	Core	Rim	Core	Rim
SiO_2	0.07	0.05	0.03	0.05	0.04	0.06	41.39	40.33	53.08	51.63	52.21	53.68
TiO_2	4.25	4.79	4.05	4.83	4.15	5.26	0.02	0.02	0.37	0.68	0.49	0.40
Al_2O_3	1.93	2.49	1.85	3.35	2.44	3.02	0.01	0.02	2.36	3.96	3.79	2.04
FeO^{t*1}	85.73	83.67	85.19	82.45	85.75	81.74	11.26	11.61	4.89	5.98	4.86	5.10
MnO	0.47	0.47	0.50	0.51	0.42	0.56	0.18	0.21	0.12	0.18	0.09	0.16
MgO	1.09	1.65	1.56	2.19	1.18	2.33	48.66	48.84	16.76	15.28	15.84	16.90
CaO	< 0.01	< 0.01	n.d.	0.02	n.d.	0.04	0.15	0.14	22.81	22.70	22.94	22.37
Na_2O	0.02	0.02	0.02	0.01	n.d.	n.d.	n.d.	n.d.	0.25	0.29	0.30	0.22
K_2O	-	-	-	-	-	-	-	-	-	-	-	-
Cr_2O_3	0.21	0.22	0.19	0.21	0.23	0.29	0.05	0.03	0.08	0.14	0.71	0.09
NiO	0.01	0.06	0.03	0.04	0.02	0.04	0.25	0.20	0.02	0.01	n.d.	0.01
Total	93.77	93.41	93.41	93.65	94.23	93.36	101.96	101.39	100.74	100.85	101.23	100.98
An#[*2]	-	-	-	-	-	-	-	-	-	-	-	-
Si[*3]	-	-	-	-	-	-	-	-	-	-	-	-
$(Na+K)_A$[*3]	-	-	-	-	-	-	-	-	-	-	-	-
Mg/Mn	4.10	6.24	5.49	7.56	2.39	4.84	-	-	-	-	-	-
Mg#[*4]	-	-	-	-	-	-	88.5	88.2	85.9	82.0	85.3	85.5

[*1] Total Fe is expressed as FeOt. [*2] An# is reported in mol.%. [*3] Units of Si and $(Na + K)_A$ are per formula unit. [*4] Mg# is reported in mol.%.

Table S3. Representative chemical compositions (wt.%; n.d., not detected) of phenocrysts in basaltic sample.

Phenocryst	Plagioclase		Plagioclase		Plagioclase		Amphibole (Pargasite)		Amphibole (Pargasite)		Amphibole (Pargasite)	
Sample name	1A-5	1A-5r	1A-7	1A-7r	1A-3	1A-3r	1A-Hy-3	1A-Hy-3r	1A-Hy-4	1A-Hy-4r	1A-Hy-1	1A-Hy-1r
Point	Core	Rim	Core	Rim	Core	Rim	Core	Rim	Core	Rim	Core	Rim
SiO_2	62.52	49.57	60.86	52.81	49.55	48.59	41.94	42.63	41.82	41.68	41.58	42.06
TiO_2	-	-	-	-	-	-	2.01	2.17	2.28	2.08	2.03	2.08
Al_2O_3	25.00	32.60	25.52	29.94	32.65	32.88	12.66	12.73	12.71	13.15	13.21	12.72
FeO^{t*1}	0.14	0.52	0.12	0.68	0.53	0.50	10.96	10.19	10.81	13.36	10.90	11.80
MnO	-	-	-	-	-	-	0.10	0.11	0.11	0.18	0.12	0.15
MgO	n.d.	0.07	0.01	0.07	0.06	0.06	14.63	15.22	14.84	12.87	14.50	13.91
CaO	6.62	16.42	7.23	13.38	16.00	16.27	11.98	11.90	11.88	11.89	11.94	12.00
Na_2O	7.76	2.03	7.52	3.79	2.21	2.03	2.43	2.46	2.38	2.44	2.38	2.44
K_2O	0.36	0.10	0.30	0.16	0.11	0.07	0.94	0.92	1.13	0.74	1.08	0.82
Cr_2O_3	-	-	-	-	-	-	0.02	0.02	n.d.	n.d.	n.d.	n.d.
NiO	-	-	-	-	-	-	-	-	-	-	-	-
Total	102.40	101.31	101.56	100.83	101.11	100.38	97.66	98.35	97.96	98.39	97.74	97.97
An#[*2]	31.4	81.2	34.1	65.5	79.5	81.3	-	-	-	-	-	-
Si[*3]	-	-	-	-	-	-	6.10	6.12	6.06	6.07	6.04	6.12
$(Na + K)_A$[*3]	-	-	-	-	-	-	0.73	0.68	0.72	0.68	0.73	0.71
Mg/Mn	-	-	-	-	-	-	-	-	-	-	-	-
Mg#[*4]	-	-	-	-	-	-	-	-	-	-	-	-

(continued)

Phenocryst	Titano-magnetite		Titano-magnetite		Olivine	Olivine	Olivine	Clinopyroxene		Clinopyroxene	
Sample name	1A-Ox-7	1A-Ox-7r	1A-Ox-1	1A-Ox-1r	1A-Mf-24	1A-Mf2-5	1A-Mf-5	1A-Mf-13	1A-Mf-13r	1A2-Mf-4	1A2-Mf-4r
Point	Core	Rim	Core	Rim	Core	Core	Core	Core	Rim	Core	Rim
SiO_2	0.05	0.07	0.06	0.07	40.94	41.04	41.10	47.77	51.84	51.70	52.93
TiO_2	4.23	4.85	4.10	4.52	0.03	0.01	0.01	1.16	0.60	0.49	0.36
Al_2O_3	2.03	4.90	1.97	4.19	0.02	0.01	0.01	7.50	4.00	3.00	2.24
FeO^{t*1}	85.67	80.48	85.61	82.02	11.58	10.72	10.60	6.82	6.06	6.48	5.46
MnO	0.46	0.58	0.46	0.61	0.21	0.16	0.19	0.12	0.16	0.22	0.14
MgO	1.04	2.52	1.14	1.84	48.09	49.11	49.12	13.48	15.42	16.56	16.65
CaO	0.01	n.d.	n.d.	n.d.	0.13	0.13	0.16	22.60	22.60	21.23	22.48
Na_2O	0.02	n.d.	0.01	0.03	n.d.	n.d.	< 0.01	0.33	0.32	0.28	0.24
K_2O	-	-	-	-	-	-	-	-	-	-	-
Cr_2O_3	0.23	0.22	0.23	0.21	0.02	0.05	0.03	0.06	0.09	0.01	0.08
NiO	0.04	0.05	0.08	0.04	0.22	0.24	0.29	0.01	n.d.	n.d.	0.03
Total	93.78	93.66	93.65	93.53	101.23	101.47	101.50	99.84	101.10	99.97	100.61
An#[*2]	-	-	-	-	-	-	-	-	-	-	-
Si[*3]	-	-	-	-	-	-	-	-	-	-	-
$(Na+K)_A$[*3]	-	-	-	-	-	-	-	-	-	-	-
Mg/Mn	3.39	7.70	4.35	3.85	-	-	-	-	-	-	-
Mg#[*4]	-	-	-	-	88.1	89.1	89.2	77.9	81.9	82.0	84.5

[*1] Total Fe is expressed as FeOt. [*2] An# is reported in mol.%. [*3] Units of Si and $(Na + K)_A$ are per formula unit. [*4] Mg# is reported in mol.%.

Table S4. Whole-rock major (wt.%) and trace elements (ppm), and isotopic compositions of representative 1991 samples.

Unit	J12-S	J12-S	J15-R	J15-R	J15-R	J15-R	J15-R
Sample name	P22892-3A	L-A teph	121205MP-H	121205C-Bm1	121205C-Bm2	121205C-Bm3	121205C-B1
SiO_2	59.28	59.61	64.66	66.11	65.20	65.59	65.73
TiO_2	0.67	0.67	0.60	0.53	0.51	0.52	0.52
Al_2O_3	15.99	16.08	16.10	16.30	16.29	16.59	16.54
$Fe_2O_3{}^{t*1}$	6.31	6.23	4.88	4.53	4.55	4.53	4.41
MnO	0.13	0.13	0.11	0.10	0.11	0.11	0.10
MgO	4.83	4.94	2.75	0.72	2.29	2.28	2.24
CaO	7.05	7.15	5.92	2.57	5.11	5.50	5.04
Na_2O	3.94	3.84	5.10	2.81	4.58	4.75	4.65
K_2O	1.57	1.66	1.44	3.18	1.48	1.40	1.48
P_2O_5	0.25	0.25	0.22	0.18	0.17	0.18	0.18
Total	99.61	99.90	99.70	100.32	99.52	100.52	100.39
V	171	170	123	-	-	-	111
Cr	157	154	43	-	-	-	42
Co	23	23	17	-	-	-	15
Ni	52	54	21	-	-	-	19
Rb	43	46	46	-	-	-	45
Sr	590	588	534	-	-	-	557
Y	18	17	17	-	-	-	16
Zr	106	112	127	-	-	-	120
Nb	1.9	2.5	3.6	-	-	-	2.9
Ba	402	424	508	-	-	-	498
La	18.0	-	16.0	-	-	-	-
Ce	37.1	-	32.5	-	-	-	-
Nd	18.8	-	15.3	-	-	-	-
Sm	3.99	-	3.18	-	-	-	-
Eu	1.10	-	0.83	-	-	-	-
Gd	3.55	-	2.84	-	-	-	-
Tb	0.50	-	0.42	-	-	-	-
Dy	2.76	-	2.39	-	-	-	-
Ho	0.55	-	0.49	-	-	-	-
Er	1.55	-	1.38	-	-	-	-
Tm	0.23	-	0.21	-	-	-	-
Yb	1.47	-	1.34	-	-	-	-
Lu	0.23	-	0.21	-	-	-	-

(continued)

Unit Sample name	J15-R 121205C-B2	J15-R 121205C-B3	J15-R 121202C-B1	J15-R 121202C-B2	J15-R 121202C-B3	J15-R 121202C-B4	J15-R 121202C-B5
SiO_2	65.55	65.98	66.72	66.52	65.88	65.94	65.90
TiO_2	0.56	0.55	0.50	0.52	0.51	0.54	0.51
Al_2O_3	16.45	16.44	16.24	16.28	16.98	16.63	16.57
$Fe_2O_3{}^{t*1}$	4.65	4.46	4.18	4.35	4.25	4.36	4.28
MnO	0.11	0.10	0.10	0.10	0.10	0.10	0.10
MgO	2.20	2.64	2.31	2.43	2.37	2.39	2.33
CaO	5.01	4.97	4.79	5.00	4.83	4.86	4.76
Na_2O	4.61	4.40	4.44	4.50	4.54	4.52	4.51
K_2O	1.43	1.61	1.60	1.54	1.59	1.60	1.62
P_2O_5	0.21	0.21	0.18	0.19	0.18	0.17	0.18
Total	100.42	100.51	100.52	100.62	100.67	100.54	100.22
V	116	109	103	110	106	111	109
Cr	44	40	38	41	42	40	45
Co	15	16	14	15	14	15	15
Ni	19	17	18	18	17	18	18
Rb	46	44	47	45	41	45	44
Sr	545	535	541	543	587	553	569
Y	16	16	14	15	14	14	16
Zr	127	127	117	120	123	120	124
Nb	3.2	3.2	3.5	3.1	2.6	2.8	3.5
Ba	495	505	512	514	465	503	482
La	15.8	-	15.2	14.8	-	-	-
Ce	31.5	-	30.3	31.1	-	-	-
Nd	14.9	-	13.8	13.6	-	-	-
Sm	3.02	-	2.77	2.74	-	-	-
Eu	0.77	-	0.73	0.73	-	-	-
Gd	2.74	-	2.51	2.45	-	-	-
Tb	0.40	-	0.36	0.36	-	-	-
Dy	2.27	-	2.09	2.06	-	-	-
Ho	0.46	-	0.43	0.42	-	-	-
Er	1.31	-	1.22	1.20	-	-	-
Tm	0.20	-	0.19	0.19	-	-	-
Yb	1.30	-	1.20	1.18	-	-	-
Lu	0.20	-	0.19	0.19	-	-	-

(continued)

Unit Sample name	J15-R 121202C-B6	J15-R 121202C-B7	J15-R 121202C-B8	J15-R 121202C-B9	J15-R 120801MPa	J15-R 120801MPb	J15-R 120801MPc
SiO_2	66.01	65.58	66.30	66.50	65.39	64.43	64.59
TiO_2	0.51	0.54	0.56	0.52	0.55	0.56	0.60
Al_2O_3	16.66	16.82	15.96	16.37	16.39	16.53	16.09
$Fe_2O_3^{t*1}$	4.28	4.40	4.79	4.33	4.49	4.65	5.03
MnO	0.10	0.10	0.11	0.10	0.10	0.11	0.12
MgO	2.51	2.27	2.31	2.15	2.26	2.25	2.46
CaO	4.95	4.65	4.72	4.93	4.86	4.87	4.66
Na_2O	4.45	4.48	4.47	4.66	4.60	4.62	4.39
K_2O	1.53	1.62	1.61	1.47	1.57	1.58	1.62
P_2O_5	0.18	0.20	0.19	0.19	0.19	0.20	0.21
Total	100.60	100.51	100.55	100.81	100.06	99.87	99.99
V	106	110	121	107	116	116	127
Cr	39	41	44	42	43	45	50
Co	15	14	16	15	16	16	17
Ni	18	18	20	18	20	20	22
Rb	44	44	47	44	45	41	40
Sr	564	569	522	539	563	573	543
Y	15	15	15	15	15	17	17
Zr	117	130	128	123	124	126	128
Nb	3.1	3.2	3.3	3.3	3.5	2.9	3.4
Ba	499	498	500	490	483	461	467
La	15.3	-	15.8	-	15.3	-	15.1
Ce	30.0	-	31.4	-	30.4	-	30.7
Nd	13.8	-	14.7	-	14.2	-	15.4
Sm	2.78	-	2.95	-	2.88	-	3.22
Eu	0.76	-	0.76	-	0.79	-	0.84
Gd	2.50	-	2.67	-	2.61	-	2.95
Tb	0.36	-	0.40	-	0.39	-	0.45
Dy	2.13	-	2.29	-	2.22	-	2.56
Ho	0.42	-	0.47	-	0.45	-	0.52
Er	1.22	-	1.32	-	1.29	-	1.47
Tm	0.18	-	0.20	-	0.19	-	0.23
Yb	1.19	-	1.32	-	1.23	-	1.43
Lu	0.19	-	0.21	-	0.20	-	0.23

(continued)

Unit Sample name	J15-R 120801MP e	J15-R PH-13-F-PR	J15-P 121205MP-T	J15-P 121205C-M1	J15-P PH-13-F-PP
SiO_2	64.18	64.41	64.93	63.99	64.85
TiO_2	0.57	0.58	0.54	0.44	0.58
Al_2O_3	16.46	16.04	16.72	17.73	16.60
$Fe_2O_3{}^{t*1}$	4.91	4.94	4.34	4.09	4.79
MnO	0.12	0.12	0.10	0.09	0.10
MgO	3.89	3.69	4.38	4.26	2.79
CaO	5.45	6.20	6.98	6.82	5.87
Na_2O	3.86	4.31	3.84	3.86	5.26
K_2O	1.47	1.35	1.59	1.52	1.38
P_2O_5	0.20	0.20	0.18	0.16	0.18
Total	99.82	99.44	99.82	100.03	99.87
V	122	126	109	-	124
Cr	45	50	47	-	48
Co	16	16	15	-	15
Ni	20	20	19	-	19
Rb	41	40	41	-	39
Sr	560	551	587	-	581
Y	17	16	15	-	15
Zr	134	126	123	-	128
Nb	3.3	2.9	2.8	-	2.9
Ba	477	461	468	-	452
La	-	-	-	14.2	14.6
Ce	-	-	-	28.5	28.8
Nd	-	-	-	12.8	13.5
Sm	-	-	-	2.56	2.72
Eu	-	-	-	0.78	0.77
Gd	-	-	-	2.34	2.50
Tb	-	-	-	0.34	0.36
Dy	-	-	-	1.94	2.10
Ho	-	-	-	0.40	0.43
Er	-	-	-	1.13	1.19
Tm	-	-	-	0.17	0.18
Yb	-	-	-	1.12	1.20
Lu	-	-	-	0.17	0.19

(continued)

Unit Sample name	J12-S P22892-3A	J12-S L-A teph	J15-R 121205MP-H	J15-R 121205C-Bm1	J15-R 121205C-Bm2	J15-R 121205C-Bm3	J15-R 121205C-B1
^{87}Sr/^{86}Sr^{*2}	0.704236	-	0.704196	-	-	-	-
^{143}Nd/^{144}Nd	0.512842	-	0.512924	-	-	-	-
^{206}Pb/^{204}Pb	18.4400	-	18.4242	-	-	-	-
^{207}Pb/^{204}Pb	15.5944	-	15.5892	-	-	-	-
^{208}Pb/^{204}Pb	38.6185	-	38.5943	-	-	-	-

Unit Sample name	J15-R 121205C-B2	J15-R 121205C-B3	J15-R 121202C-B1	J15-R 121202C-B2	J15-R 121202C-B3	J15-R 121202C-B4	J15-R 121202C-B5
^{87}Sr/^{86}Sr^{*2}	0.704184	-	0.704219	0.704188	-	-	-
^{143}Nd/^{144}Nd	0.512919	-	0.512915	0.512918	-	-	-
^{206}Pb/^{204}Pb	18.4235	-	18.4232	18.4235	-	-	-
^{207}Pb/^{204}Pb	15.5896	-	15.5897	15.5902	-	-	-
^{208}Pb/^{204}Pb	38.5939	-	38.5940	38.5954	-	-	-

Unit Sample name	J15-R 121202C-B6	J15-R 121202C-B7	J15-R 121202C-B8	J15-R 121202C-B9	J15-R 120801MP a	J15-R 120801MP b	J15-R 120801MP c
^{87}Sr/^{86}Sr^{*2}	0.704184	-	0.704188	-	0.704202	-	0.704194
^{143}Nd/^{144}Nd	0.512927	-	0.512919	-	0.512918	-	0.512920
^{206}Pb/^{204}Pb	18.4240	-	18.4241	-	18.4245	-	18.4239
^{207}Pb/^{204}Pb	15.5903	-	15.5898	-	15.5907	-	15.5898
^{208}Pb/^{204}Pb	38.5962	-	38.5957	-	38.5973	-	38.5950

Unit Sample name	J15-R 120801MP e	J15-R PH-13-F-PR	J15-P 121205MP-T	J15-P 121205C-M1	J15-P PH-13-F-PP
^{87}Sr/^{86}Sr^{*2}	-	-	-	0.704194	0.704193
^{143}Nd/^{144}Nd	-	-	-	0.512914	0.512918
^{206}Pb/^{204}Pb	-	-	-	18.4229	18.4220
^{207}Pb/^{204}Pb	-	-	-	15.5907	15.5900
^{208}Pb/^{204}Pb	-	-	-	38.5959	38.5938

V-Ba and La-Lu were analyzed by XRF and ICP-MS, respectively.

[*1] Total Fe expressed as $Fe_2O_3^t$. In Harker diagrams (Fig. 7), total Fe is expressed as $FeO^t = FeO + 0.8998Fe_2O_3$ and normalized to 100%.

[*2] Maximum standard errors are 0.000008 for Sr, 0.000005 for Nd, 0.0003 for ^{206}Pb and ^{207}Pb, and 0.0008 for ^{208}Pb.

Table S5. Magmatic temperature (°C) of the 1991 dacitic magma (major element concentrations in wt.%; n.d., not detected) based on magnetite-ilmenite pair geothermometer.

	Magma type	Dacite		Dacite		Dacite		Dacite	
	Phenocryst	Magnetite	Ilmenite	Magnetite	Ilmenite	Magnetite	Ilmenite	Magnetite	Ilmenite
	Grain name	02CB1-14-3	02CB1-14-4	0801Cd-15-2	0801Cd-15-3	0801L-9-3	0801L-9-2	0801H-6-5	0801H-6-4
	Point	Rim	Rim	Rim	Rim	Rim	Rim	Rim	Rim
	SiO_2	0.05	0.02	0.06	0.03	0.05	< 0.01	0.07	n.d.
	TiO_2	4.47	28.49	4.58	28.55	4.49	28.52	4.78	28.28
	Al_2O_3	1.95	0.35	2.00	0.36	1.94	0.37	1.91	0.35
	FeO^{t*1}	86.42	65.78	83.74	63.52	85.96	65.02	84.59	64.86
	MnO	0.44	0.23	0.43	0.23	0.42	0.23	0.45	0.23
	MgO	1.18	1.05	1.10	0.99	1.15	1.06	1.11	0.92
	CaO	n.d.	0.01	n.d.	0.01	n.d.	0.00	n.d.	n.d.
	Na_2O	n.d.	n.d.	0.01	n.d.	n.d.	n.d.	0.01	0.01
	Cr_2O_3	0.19	0.06	0.18	0.07	0.22	0.08	0.21	0.07
	NiO	0.01	n.d.	0.02	n.d.	0.07	n.d.	0.04	0.02
	Total	94.70	96.00	92.12	93.76	94.30	92.28	93.16	94.75
	Mg/Mn	4.74	7.96	4.50	7.67	4.77	8.05	4.31	6.99
T^{*2}	A&L88	788		795		781		804	
	G&E08	732		745		735		749	

[*1] Total Fe is expressed as FeO^t.

[*2] Temperatures calculated by Andersen and Lindsley (1988; 'A&L88') and Ghiorso and Evans (2008; 'G&E08'). The original temperature of Andersen and Lindsley (1988) is reduced by 30˚C following Geschwindt and Rutherford (1993). According to Blundy and Cashman (2008), the average absolute deviations of A&L88 and G&E08 are ±33 ˚C and ±44 ˚C, respectively. For the temperature calculation, the ferric-ferrous ratio and the mole fractions of ulvöspinel and ilmenite were calculated by the method of Stormer (1983).

Table S6. Whole-rock major element and mineral compositions (wt.%) for mass balance calculation.

Magma or Mineral	D1	Plagioclase	Amphibole	Titano-magnetite	D2
SiO_2	63.97	55.57	45.36	0.04	66.37
TiO_2	0.56	-	1.59	4.27	0.52
Al_2O_3	16.84	28.17	10.42	1.95	16.15
FeO^{t}[*1]	4.29	0.17	13.81	86.05	3.86
MnO	0.11	-	0.46	0.43	0.10
MgO	2.59	-	13.81	1.14	2.20
CaO	5.44	10.77	11.00	0.01	4.53
Na_2O	4.58	5.43	1.82	0.01	4.46
K_2O	1.43	0.16	0.40	-	1.62
P_2O_5	0.20	-	-	-	0.18
Total[*2]	100.00	100.27	98.67	93.90	100.00
Proportion[*3]	1.000	0.094	0.055	0.003	0.848
Mineral ratio (%)	-	61.8	36.1	2.1	-

[*1] Total Fe is expressed as FeO^{t}.

[*2] Total of mineral was normalized to 100% prior to calculation.

[*3] Proportions of magma and mineral were gained by best fitting (see text for detail).

Table S7. Representative chemical compositions (wt.%; n.d., not detected) of titano-magnetite in andesitic scoria and dacitic pumice.

Unit	J12-S	J12-S	J12-S	J12-S	J12-S	J12-S	J15-P	J15-P	J15-R	J15-R
Sample name	100a-2	100a-2r	101a-1	101a-r	S2-3ox-5	S2-3ox-5r	S2-2ox-1	S2-2ox-1r	B2-1ox-1	B2-1ox-1r
Point	Core	Rim	Core	Rim	Core	Rim	Core	Rim	Core	Rim
SiO_2	0.07	0.05	0.04	0.09	0.07	0.08	0.03	0.04	0.06	0.04
TiO_2	4.03	5.00	4.20	5.22	4.10	5.29	4.20	4.17	4.04	4.07
Al_2O_3	1.75	2.47	2.19	3.26	2.03	2.69	1.74	1.79	1.84	1.86
FeO^{t*1}	86.80	84.20	85.73	83.87	85.25	82.52	85.20	84.49	85.87	85.39
MnO	0.47	0.54	0.41	0.50	0.45	0.55	0.51	0.43	0.51	0.56
MgO	1.68	2.29	2.25	2.38	1.14	2.16	1.13	1.13	1.00	1.05
CaO	n.d.	0.01	n.d.	0.04	0.00	0.15	n.d.	n.d.	n.d.	0.02
Na_2O	0.01	n.d.	0.01	0.01	n.d.	n.d.	0.00	n.d.	n.d.	0.00
Cr_2O_3	0.23	0.01	0.21	0.24	0.24	0.07	0.21	0.21	0.21	0.19
NiO	0.02	0.04	0.07	0.03	0.03	n.d.	0.03	0.03	0.02	0.02
Total	95.05	94.80	95.09	95.63	93.32	93.51	93.05	92.27	93.54	93.21
Mg/Mn	6.35	7.41	9.76	8.43	2.32	4.45	2.31	2.32	2.03	2.15
$X_{usp}{}^{*2}$	0.11	0.14	0.12	0.15	0.11	0.11	0.11	0.11	0.11	0.11

[*1] Total Fe is expressed as FeO^t.

[*2] Ferric-ferrous ratio and mole fractions of ulvöspinel was calculated by the method of Stormer (1983).

Table S8. Representative diffusion time and adapted parameters in quartz.

Rock type	Sample name	Grain name	Location	Diffusion time (year)[*1]		
				Ave.	+ σ	- σ
Dacite	0801C-K	0801L-1	Core	15	6	40
			Rim	10	4	25
	0801C-O	0801H-3	Rim	7	3	15
		0801H-2	Core	50	20	150
			Mantle	50	20	100
			Rim	50	20	120
	PH-13-F-PR	20-9A-6	Core	60	30	150
			Mantle	35	15	90
			Rim	20	8	50
		20-9A-8	Core	80	30	200
			Rim	10	4	25
		20-9A-2	Mantle	20	7	50
			Rim	70	25	180
		20-9A-11	Rim	300	100	800
		20-9_10-2	Core	400	150	900
			Rim	200	90	500
	120801MP b	20-6B-3	Rim	5	2	12
		20-6D-1	Core	50	20	120
			Mantle	20	8	50
			Rim	60	20	150
		20-6D-2	Mantle	60	20	150
			Rim	80	30	200
		20-6D-10	Core	40	10	100
			Mantle	100	40	250
			Rim	20	8	50
	1202C-B1	20-10-1	Core	400	150	900
			Mantle	70	30	180
			Rim	30	10	80
Basalt	P22892-1A	1A-2-3	Rim	0.009	0.003	0.015
		1A-2-2	Rim	0.003	0.001	0.007
		1A-2-5	Rim	0.004	0.0015	0.006
		1A-2-t	Rim	0.009	0.003	0.015

[*1] Diffusion time was gained due to confirming best fitting value by eye. Temperature uncertainty show Appendix B for detail. '+0' and '-0' correspond to positive and negative uncertainty, respectively.

Table S9. Representative diffusion time estimated by Ti and Al contents of titano-magnetite in andesitic scoria.

		Diffusion time (day)[*1]					
Sample name	Grain name	Ave.		Max.		Min.	
		Ti	Al	Ti	Al	Ti	Al
P22892-3	ox-4L	0.2	0.5	0.08	0.15	0.4	1.2
	ox-8L	0.12	1	0.04	0.3	0.2	2.5
	M2-3ox-1L	0.4	0.9	0.15	0.3	0.7	2.5
	101a-4L	1.4	5	0.5	1.5	2.8	12
	101a-5L	2.4	2.5	0.8	1.6	4	6
	101a-6L	0.6	1.5	0.2	0.5	1.2	4
	101a-2L	40	50	15	14	70	120
TephraA	100a-10L	0.8	2.5	0.3	0.8	1.5	6
	100b-2L	0.5	1.5	0.2	0.5	1	5
P22892-3A	102b-5L	0.5	2.0	0.2	0.5	1	5
	102b-6L	3.5	5	1.3	1.5	7	13
	102b-17L	2.5	2.5	1	0.7	5	6
	102b-20L	0.3	1	0.12	0.3	0.6	3
	102b-19L	8	4	3	1.2	15	10
	102b-24L	3	5	1.2	1.5	6	12

[*1] Diffusion time of Ti and Al were calculated by the method of Crank (1975). 'Ave', 'Max' and 'Min' correspond to average, maximum and minimum temperatures, respectively. They were estimated from Fe-Ti oxide thermometry in Andersen and Lindsley (1988). See Appendix C for detail.

References

Andersen, D.J., Lindsley, D.H., 1988. Internally consistent solution models for Fe-Mg-Mn-Ti oxides; Fe-Ti oxides. American Mineralogist 73, 714-726.

Bachmann, O., Bergantz, G.W., 2004. On the origin of crystal-poor rhyolites: extracted from batholithic crystal mushes. Journal of Petrology 45, 1565-1582.

Bacon, C.R., Druitt, T.H., 1988. Compositional evolution of the zoned calcalkaline magma chamber of Mount Mazama, Crater Lake, Oregon. Contributions to Mineralogy and Petrology 98, 224-256.

Bacon, C.R., Hirschmann, M.M., 1988. Mg/Mn partitioning as a test for equilibrium between coexisting Fe-Ti oxides. American Mineralogist 73, 57-61.

Beard, J.S., Lofgren, G.E., 1991. Dehydration melting and water-saturated melting of basaltic and andesitic greenstones and amphibolites at 1, 3 and 6.9 kb. Journal of Petrology 32, 365-401.

Bernard, A., Knittel, U., Weber, B., Weis, D., Albrecht, A., Hattori, K., Klein, J., Oles, D., 1996. Petrology and Geochemistry of the 1991 Eruption Products of Mount Pinatubo. In: Newhall, C.G., Punongbayan, R.S. (eds.), Fire and Mud. Eruptions and Lahars of Mt. Pinatubo, Philippines. University of Washington Press, Seattle, 767-798.

Bindeman, I.N., Bailey, J.C., 1994. A model of reverse differentiation at Dikii Greden' Volcano, Kamchatka: progressive basic magma vesiculation in a silicic magma chamber. Contributions to Mineralogy and Petrology 117, 263-278.

Blundy, J., Cashman, K., 2008. Petrologic reconstruction of magmatic system variables and processes. Reviews in mineralogy and geochemistry 69, 179-239.

Borisova, A.Y., Toutain, J.P., Dubessy, J., Pallister, J.S., Zwick, A.Z., Salvi, S., 2014. H2O-CO2-S fluid triggering the 1991 Mount Pinatubo climatic eruption (Philippines). Bulletin of Volcanology 76, 1-9.

Castillo, P.R., Punongbayan, R.S., 1996. Petrology and Sr, Nd, and Pb isotopic geochemistry of Mount Pinatubo volcanic rocks. In: Newhall, C.G., Punongbayan, R.S. (eds.), Fire and Mud. Eruptions and Lahars of Mt. Pinatubo, Philippines. University of Washington Press, Seattle, 799-806.

Chamberlain, K.J., Morgan, D.J., Wilson, C.J., 2014. Timescales of mixing and mobilisation in the Bishop Tuff magma body: perspectives from diffusion chronometry. Contributions to Mineralogy and Petrology, 168, 1034.

Cherniak, D.J., Watson, E.B., Wark, D.A., 2007. Ti diffusion in quartz. Chemical Geology, 236, 65-74.

Coombs, M.L., Gardner, J.E., 2004. Reaction rim growth on olivine in silicic melts: implications for magma mixing. American Mineralogist 89, 748-758.

Coombs, M.L., Eichelberger, J.C., Rutherford, M.J., 2000. Magma storage and mixing conditions for the 1953-1974 eruptions of Southwest Trident volcano, Katmai National Park, Alaska. Contributions to Mineralogy and Petrology, 140, 99-118.

Cooper, G.F., Wilson, C.J.N., Millet, M.A., Baker, J.A., Smith, E.G.C., 2012. Systematic tapping of independent magma chambers during the 1 Ma Kidnappers supereruption. Earth and Planetary Science Letters 313-314, 23-33.

Costa, F., Morgan, D., 2010. Time constrains from chemical equilibration in magmatic crystals. Timescales of magmatic processes: from core to atmosphere, 1, 125-159.

Crank, J., 1975. The mathematics of diffusion (2nd eds). Oxford University Press.

Daag, A.S., D., Dolan, Laguerta, E.P., Meeker, G.P., Newhall, C.G., Pallister, J.P., Solidum, R.U., 1996. Growth of a postclimactic lava dome at Mount Pinatubo, July-October 1992. In: Newhall, C.G., Punongbayan, R.S. (eds.), Fire and Mud. Eruptions and Lahars of Mt. Pinatubo, Philippines. University of Washington Press, Seattle, 647-664.

Deer, W.A., Howie, R.A., Zussman, J., 1992. An Introduction to the Rock-Forming Minerals (2nd eds.). London (Longman Scientific and Technical), pp.696.

Delfin, F.G., Jr., 1983. Geology of the Mt. Pinatubo geothermal project: Philippine National Oil Company, unpublished report, 35p. plus figure.

Delfin, F.G., Jr., 1984. Geology and geothermal potential of Mt. Pinatubo: Philippine National Oil Company, unpublished report, 36p.

de Silva, S., Salas, G., Schubring, S., 2008. Triggering explosive eruptions-The case of silicic magma recharge at Huaynaputina, southern Peru. Geological Society of America, 36, 387-390.

Devine, J.D., Rutherford, M.J., Norton, G.E., Young, S.R., 2003. Magma storage region processes inferred from geochemistry of Fe-Ti oxides in andesitic magma, Soufriere Hills Volcano, Mountserrat WI. Journal of Petrology, 44, 1375-1400.

Druitt, T.H., Costa, F., Deloule, E., Dongan, M., Scaillet, B., 2012. Decadal to monthly timescales of magma transfer and reservoir growth at a caldera volcano. Nature 482, 77-80.

Dunstan, L.P., Gramlich, J.W., Bornes, I.L., 1980. Absolute isotopic abundance and the atomic weight of a reference sample of thallium. Journal of Research of the National Bureau of Standards, 85, 1-10.

Eichelberger, J.C., Izbekov, P.E., Browne, B.L., 2006. Bulk chemical trends at arc volcanoes are not liquid lines of descent. Lithos 87, 135-154.

Ewert, J.W., Lockhart, A.B., Marcial, S., Ambubuyog, G., 1996. Ground deformation prior to the 1991 eruptions of Mount Pinatubo. In: Newhall, C.G., Punongbayan, R.S. (eds.) Fire and Mud. Eruptions and Lahars of Mt. Pinatubo, Philippines. University of Washington Press, Seattle,329-350.

Feeley, T.C., Dungan, M.A., Frey, F.A., 1998. Geochemical constraints on the origin of mafic and silicic magmas at Cordon El Guadal, Tatara-San Pedro Complex, central Chile. Contributions to Mineralogy and Petrology 131, 393-411.

Fournelle, J., Carmody, R., Daag, A.S., 1996. Anhydrite-bearing pumices from the June 15, 1991, eruption of Mount Pinatubo: Geochemistry, mineralogy, and petrology. In: Newhall, C.G., Punongbayan, R.S. (eds.), Fire and Mud. Eruptions and Lahars of Mt. Pinatubo, Philippines. University of Washington Press, Seattle, 845-864.

Geschwind, C.H., Rutherford, M.J., 1992. Cummingtonite and the evolution of the Mount St. Helens (Washington) magma system: An experimental study. Geology 20, 1011-1014.

Ghiorso, M.S., Evans, B.W., 2008. Thermodynamics of rhombohedral oxide solid solutions and a revision of the Fe-Ti two-oxide geothermometer and oxygen-barometer. American Journal of Science 308, 957-1039.

Gualda, G.A.R., Pamukcu, A.S., Ghiorso, M.S., Anderson Jr., A.T., Sutton, S.R., Rivers. M.L., 2012. Timescale of quartz crystallization and the longevity of the Bishop giant magma body. Plos One, 7, e37492.

Hammer, J.E., Rutherford, M.J., 2003. Petrologic indicators of pre-eruption magma dynamics. Geology 31, 79-82.

Hansen, J., Skjerlie, K.P., Pederson, R.B., Rosa, J.D.L., 2002. Crustal melting in the lower parts of island arcs: an example from the Bremanger Granitoid Complex, west Norwegian Caledonides. Contributions to Mineralogy and Petrology 143, 316-335.

Hanson, R.B., 1992. Effects of fluid production on fluid flow during regional and contact metamorphism. Journal of Metamorphic Geology, 10, 87-97.

Harlow, D.H., Power, J.A., Laguerta, E.P., Ambubuyog, G., White, R.A., Hoblitt, R.P., 1996. Precursory seismicity and forecasting of the June 15, 1991, eruption of Mount Pinatubo. In: Newhall, C.G., Punongbayan, R.S. (eds.) Fire and Mud. Eruptions and Lahars of Mt. Pinatubo, Philippines. University of Washington Press, Seattle, 285-305.

Hattori, K., Sato, H., 1996. Magma evolution recorded in plagioclase zoning in 1991 Pinatubo eruption products. American Mineralogist 81, 982-994.

Hildreth, W., 1981. Gradients in silicic magma chambers: Implications for lithospheric magmatism, Journal of Geophysical Research 86, 10153-10192.

Hildreth, W., Wilson, C.N., 2007. Compositional zoning of the Bishop Tuff. Journal of Petrology 48, 951-999.

Hoblitt, R.P., Wolfe, E.W., Scott, W.E., Couchman, M.R., Pallister, J.S., Javier, D., 1996. The preclimatic eruption of Mount Pinatubo, June 1991. In: Newhall, C.G., Punongbayan, R.S. (eds.) Fire and Mud. Eruptions and Lahars of Mt. Pinatubo, Philippines. University of Washington Press, Seattle, 457-512.

Holland, T., Blundy, J., 1994. Non-ideal interactions in calcic amphiboles and their bearing on amphibole-plagioclase thermometry. Contributions to Mineralogy and Petrology 116, 433-447.

Huang, R., Audetat, A., 2012. The titanium-in-quartz (TitaniQ) thermobarometer: A critical examination and re-calibration. Geochimica et Cosmochimica Acta, 84, 75-89.

Jego, S., Maury, R.C., Polve, M., Yumul Jr., G.P., Bellon, H., Tamayo Jr., R.A., Cotton, J., 2005. Geochemistry of adakites from the Philippines: constraints on their origins. Resource Geology 55, 161-185.

Kaneko, K., Kamata, H., Koyaguchi, T. Yoshikawa, M., Furukawa, K., 2007. Repeated large-scale eruptions from a simple compositionally stratified magma chamber: An example from Aso volcano, Southwest Japan. Journal of Volcanology and Geothermal Research 167, 160-180.

Kanno, T., Ishibashi, H., 2017. Pre-eruptive timescales estimated by diffusion chronometry of phenocryst minerals: a review. Geoscience Reports, Shizuoka University, 44, 47-64 (in Japanese).

Kilgour, G.N., Saunders, K.E., Blundy, J.D., Cashman, K.V., Scott, B.J., Miller, C.A., 2014. Timescales of magmatic processes at Ruapehu volcano from diffusion chronometry and their comparison to monitoring data. Journal of Volcanology and Geothermal Research, 288, 62-75.

King, C.R., Cooper, K.M., Shrecengost, K., Bradshaw, R.W., Kent, A.J., Huber, C., 2016. Plagioclase, Amphibole, and Magnetite in the 1991 Pinatubo Reservoir: Timescales of Crystallization. Fall Meeting of the American Geophysical Union, V43C-3166.

Kiss, B., Harangi, S., Ntaflos, T., Mason, P.R.D., Pal-Molnar, E., 2014. Amphibole perspective to unravel pre-eruptive processes and conditions in volcanic plumbing systems beneath intermediate arc volcanoes: a case study from Ciomadul volcano (SE Carpathians). Contributions to Mineralogy and Petrology 167, 1-27.

Koyaguchi, T., 1985. Magma mixing in a conduit. Journal of Volcanological and Geothermal Research, 25, 365-369.

Koyaguchi, T., 1986. Mixing mechanism of mafic and felsic magmas-origin of heterogeneous magmas-. Bulletin of Volcanological Society of Japan, 30, S41-S54 (in Japanese).

Kuritani, T., Nakamura, E., 2002. Precise isotope analysis of nanogram-level Pb for natural rock samples without use of double spikes. Chemical Geology 186, 31-43.

Kuritani, T., Sakuyama, T., Kamada, N., Yokoyama, T., Nakagawa, M., 2017. Fluid-fluxed melting of mantle versus decompression melting of hydrous mantle plume as the cause of intraplate magmatism over a stagnant slab: implications from Fukue Volcano Group, SW Japan. Lithos 282-283, 98-110.

Leake, B.E., Woodlley, A.R., Arps, C.E.S., Birch, W.D., Gilbert, M.C., Grice, J.D., Hawthorne, F.C., Kato, A., Krivovichev, V.G., Linthout, K., Laird, J., Mandarino, J.A., Maresch, W.V., 1997. Nomenclature of amphiboles: Report of the subcommittee on amphiboles of the international mineralogical association, commission on new minerals and mineral names. The Canadian Mineralogist 35, 219-246.

Lockhart, A.B., Marcial, S., Ambubuyog, G., Laguerta, E.P., Power, J.A., 1996. Installation, operation, and technical specification of the first Mount Pinatubo telemeteres seismic network. In: Newhall, C.G., Punongbayan, R.S. (eds.) Fire and Mud. Eruptions and Lahars of Mt. Pinatubo, Philippines. University of Washington Press, Seattle, 215-224.

Luhr, J.F., Melson, W.G., 1996. Mineral and glass compositions in June 15, 1991, Pumices: Evidence for dynamic disequilibrium in the dacite of Mount Pinatubo. In: Newhall, C.G., Punongbayan, R.S. (eds), Fire and Mud. Eruptions and Lahars of Mt. Pinatubo, Philippines. University of Washington Press, Seattle, 733-750.

Machida, H., Arai, F., 1978. Akahoya Ash-A Holocene widespread tephra erupted from the

Kikai caldera, south Kyushu, Japan. Quaternary Research, 143-163.

Marsh, B.D., 2015. Magmatism, magma, and magma chambers. In Schubert. G. ed., Treatise on Geophysics (2nd eds.) Elsevier, 273-323.

Masubuchi, Y., Ishizaki, Y., 2011. Magmatic plumbing system of the 3400 BC caldera-forming eruption (Numazawaka eruption) of Numazawa volcano as deduced by componentry and whole-rock and mineral compositions of the pyroclastic deposits. Journal of Geological Society of Japan, 117, 357-376 (in Japanese).

Matsumoto, A., Nakagawa, M., 2010. Formation and evolution of silicic magma plumbing system: Petrology of the volcanic rocks of Usu volcano, Hokkaido, Japan. Journal of Volcanology and Geothermal Research 196, 185-207.

Matsumoto, A., Hasegawa, T., Nakagawa, M., 2018. Petrology of the 120 ka Caldera-Forming Eruption of Kutcharo Volcano, Eastern Hokkaido, Japan: Coexistence of Multiple Silicic Magmas and their Relationship with Mafic Magmas. Journal of Petrology 59, 771-793.

Matsumoto, T., Uto, K., Ono, K., Watanabe, K., 1991. K-Ar age determinations for Aso volcanic rocks: concordance with volcanostratigraphy and application to pyroclastic flows. Proceedings of the Fall Meeting of the Volcanological Society of Japan, 73 (in Japanese).

Matthews, N.E., Pyle, D.M., Smith, V.C., Wilson, C.J., Huber, C., Van Hinsberg, V., 2012. Timescales of Magma Recharge and Reactivation of Large Silicic Systems from Ti Diffusion in Quartz. Journal of Petrology, 7, 1385-1416.

McBirney, A.R., Baker, B.H., Nilson, R.H., 1985. Liquid fractionation. Part I: Basic principles and experimental simulations. Journal of Volcanology and Geothermal Research 24, 1-24.

McNutt, S.R., 1996. Seismic monitoring and eruption forecasting of volcanoes: A review of the state-of-the-art and case histories. In Scarpa, R., Tilling, R. (eds.) Monitoring and Mitigation of Volcano Hazards. Springer, 99-146.

Minakami, T., 1974. Seismology of volcanoes in Japan. In Civetta, L., Gasparini, P., Luongo, G., Rapolla, A. (eds.) Physical Volcanology. Development in Solid Earth Geophysics, 6, 1-17.

Mooney, W.D., Laske, G., Maters, T.G., 1998. CRUST 5.1. A global crustal model at 5°x5°. Journal of Geophysical Research, 103, 727-747.

Moore, A., Coogan, L.A., Costa, F., Perfit, M.R., 2014. Primitive melt replenishment and crystal-mush disaggregation in the weeks preceding the 2005-2006 eruption 9°50'N, EPR. Earth and Planetary Science Letters, 403, 15-26.

Morgan, D.J., Blake, S., Rogers, N.W.B., DeVivo, B., Rolandi, G., Macdonald, R., Hawkesworth, C.J., 2004. Time scales of crystal residence and magma chamber volume from modeling of diffusion profiles in phenocrysts: Vesuvius 1944. Earth and Planetary Science Letters, 222, 933-946.

Morgan, D.J., Blake, S., Rogers, N.W.B., DeVivo, B., Rolandi, G., Davidson, J.P., 2006. Magma chamber recharge at Vesuvius in the century prior to the eruption of A.D. 79. Geological Society of America, 34, 845-848.

Mori, J., Eberhart-Phillips, D., Harlow, D.H., 1996. Three-dimensional velocity structure at Mount Pinatubo: Resolving magma bodies and earthquake hypocenters. In: Newhall, C.G., Punongbayan, R.S. (eds.), Fire and Mud. Eruptions and Lahars of Mt. Pinatubo, Philippines. University of Washington Press, Seattle, 371-382.

Muro, A., Pallister, J., Villemant, B., Newhall, C., Semet, M., Martinez, M., Mariet, C., 2008. Pre-1991 sulfur transfer between mafic injections and dacite magma in the Mt. Pinatubo reservoir. Journal of Volcanology and Geothermal Research, 175, 517-540.

Mutch, E.J.F., Blundy, J.D., Tattitch, B.C., Cooper, F.J., Brooker, R.A., 2016. An experimental study of amphibole stability in low-pressure granitic magmas and a revised Al-in-hornblende geobarometer. Contributions to Mineralogy and Petrology 171, 1-27.

Nakamichi, H., Hamaguchi, H., Tanaka, S., Ueki, S., Nishimura, T., Hasegawa, A., 2003. Source mechanisms of deep and intermediate-depth low-frequency earthquakes beneath Iwate volcano, northeastern Japan. Geophysical Journal International, 154, 811-828.

Nakamura, M., 1995a. Continuous mixing of crystal mush and replenished magma in the ongoing Unzen eruption. Geology, 23, 807-810.

Nakamura, M., 1995b. Residence time and crystallization history of nicheliferous olivine phenocrysts from the northern Yatsugatake volcanoes, Central Japan: Application of a growth and diffusion model in the system Mg-Fe-Ni. Journal of Volcanology and Geothermal Research, 66, 81-100.

Neilsen, R.L., 1990. Simulation of igneous differentiation processes. In Nicholls, J., Russell, J.K. (eds.) Reviews in mineralogy, 27: Blacksburg, Va., Mineralogical Society of America, 65-105.

Newhall, C.G., Self, S., 1982. The Volcanic Explosivity Index (VEI): an estimate of explosive magnitude for historical volcanism. Journal of Geophysical Research, 87, 1231-1238.

Newhall, C.G., Daag, A.S., Deflin, Jr., F.G., Hoblitt, R.P., McGeehin, J., Pallister, J.S., Regalado, M.T.M., Rubin, M., Tubianosa, B.S., Tamayo, Jr., R.A., Umbal, J.V., 1996. Eruptive history of Mount Pinatubo. In: Newhall, C.G., Punongbayan, R.S. (eds.), Fire and Mud. Eruptions and Lahars of Mt. Pinatubo, Philippines. University of Washington Press, Seattle, 165-196.

Noguchi, T., Shinjo, R., Ito, M., Takada, J., Oomori, T., 2011. Barite geochemistry from hydrothermal chimneys of the Okinawa Trough; insight into chimney formation and fluid/sediment interaction. Journal of Mineralogical and Petrological Sciences 106, 26-35.

Obata, M., Banno, S., Mori, T., 1974. The iron-magnesium partitioning between naturally occurring coexisting olivine and Ca-rich clinopyroxene: an application of the simple mixture model to olivine solid solution. Bulletin de Mineralogie, 97, 101-107.

Paladio-Melosantos, M.L.O., Solidum, R.U., Scott, W.E., Quiambao, R.B., Umbal, J.V., Rodolfo, K.S., Tubianosa, B.S., Reyes, P.J.D., Alonso, R.A., Ruelo, H.B., 1996. Tephra falls of the 1991 eruptions of Mount Pinatubo. In: Newhall, C.G., Punongbayan, R.S. (eds.), Fire and Mud. Eruptions and Lahars of Mt. Pinatubo, Philippines. University of Washington Press, Seattle, 513-536.

Pallister, J.S., Hoblitt, R.P., Reyes, A.G., 1992. A basalt trigger for the 1991 eruptions of Pinatubo volcano? Nature 356, 426-428.

Pallister, J.S., Hoblitt, R.P., Meeker, G.P., Knight, R.J., Siems, D.F., 1996. Magma mixing at Mount Pinatubo: Petrographic and chemical evidence from the 1991 deposits. In: Newhall, C.G., Punongbayan, R.S. (eds.), Fire and Mud. Eruptions and Lahars of Mt. Pinatubo, Philippines. University of Washington Press, Seattle, 687-731.

Peppard, B.T., Steele, I.M., Davis, A.M., Wallace, P.J., Anderson, A.T., 2001. Zoned quartz ohenocrysts from the rhyolitic Bishop Tuff. American Mineralogist, 86, 1034-1052.

Pichavant, M., Myscn, B.O., Macdonald, R., 2002. Source and H2O content of high-MgO magmas in island arc settings: an experiental study of a primitive calc-alkaline basalt from St. Vincent, Lesser Antillcs arc. Geochimica et Cosmochimica Acta 66, 2193-2209.

Pin, C., Zalduegui, J.F.S., 1997. Sequential separation of light rare-earth elements, thorium and uranium by miniaturized extraction chromatography: application to isotopic analyses of silicate rocks. Analytica Chimica Acta 339, 79-89.

Pin, C., Briot, D., Bassin, C., Poitrasson, F., 1994. Concomitant separation of strontium and samarium-neodymium for isotopic analysis in silicate samples, based on specific extraction chromatography. Analytica Chimica Acta 298, 209-217.

Power, J.A., Murray, T.L., Marso, J.N., Laguerta, E.P., 1996. Preliminary observations of seismicity at Mount Pinatubo by use of the Seismic Spectral Amplitude Measurement (SSAM) system, May 13-June 18, 1991. In: Newhall, C.G., Punongbayan, R.S. (eds.) Fire and Mud. Eruptions and Lahars of Mt. Pinatubo, Philippines. University of Washington Press, Seattle, 269-284.

Prouteau, G., Scaillet, B., 2003. Experimental constraints on the origin of the 1991 Pinatubo dacite. Journal of Petrology 44, 2203-2241.

Rae, A.S., Edmonds, M., Maclennan, J., Morgan, D., Houghton, B., Hartley, M.E., Sides, I., 2016. Time scales of magma transport and mixing at Kilauea Volcano, Hawai'i. Geology, 44, 463-466.

Rapp, R.P., Watson, E.B., Miller, C.F., 1991. Partial melting of amphibolite/eclogite and the origin of Archean trondhjemites and tonalities. Precambrian Research, 51, 1-25.

Roser, B.P., Kimura, J.-I., Hisatomi, K., 2000. Whole-rock elemental abundances in sandstones and mudrocks from the Tanabe Group, Kii Peninsula, Japan. Geoscience Report of Shimane University, 19, 101-112.

Rusk, B.G., Lowers, H.A., Reed, M.H., 2008. Trace elements in hydrothermal quartz: relationships to cathodoluminescent textures and insights into vein formation. Geology, 36, 547-550.

Rutherford, M.J., Devine, J.D., 1996. Preeruption pressure-temperature conditions and volatiles in the 1991 dacitic magma of Mount Pinatubo. In: Newhall, C.G., Punongbayan, R.S. (eds.), Fire and Mud. Eruptions and Lahars of Mt. Pinatubo, Philippines. University of Washington Press, Seattle, 751-766.

Rutherford, M.J., Hill, P.M., 1993. Magma ascent rates and magma mixing from amphibole breakdown: experiments and the 1980-1986 Mount St. Helens eruptions. Journal of Geothermal Research, 98, 19667-19685.

Rutherford, M.J., Brown, L., Pallister, J.S., 1993. Petrologic constraints on timing of magmatic processes in the 1991 Pinatubo volcanic system. Eos, Transactions, American Geophysical Union, 74, 671.

Sabit, J.P., Pigtain, R.C., de la Cruz, E.G., 1996. The West-Side Story: Observations of the 1991 Mount Pinatubo Eruptions from the West. In: Newhall, C.G., Punongbayan, R.S. (eds.), Fire and Mud. Eruptions and Lahars of Mt. Pinatubo, Philippines. University of Washington Press, Seattle, 445-455.

Sakai, S., Yamada, T., Ide, S., Mochizuki, M., Shiobara, H., Urabe, T., Hirata, N., Shinohara, M., Kanazawa, T., Nishizawa, A., Fujie, G., Mikada, H., 2001. Magma migration from the point of view of seismic activity in the volcanism of Miyake-jima Island in 2000. Journal of Geography, 110, 145-155 (in Japanese).

Sato, H.,1975. Diffusion coronas around quartz xwnocrysts in andesite and basalt from Tertialy volcanic region in Northeastern Shikoku, Japan. Contributions to Mineralogy and Petrology 50, 49-64.

Saunders, K.E., Morgan, D.J., Baker, J.A., Wysoczanski, R.J., 2010. The magma evolution of the Whakamaru supereruption, New Zealand, constrained by a microanalytical study of plagioclase and quartz. Journal of Petrology, 51, 2465-2488.

Scaillet, B., Evans, B.W., 1999. The 15 June 1991 eruption of Mount Pinatubo. I, Phase equilibria and preeruption P-T-fO2-fH2O conditions of the dacite magma. Journal of Petrology 40, 381-411.

Schmincke, H.U., 2004. Volcanism. Springer, 324p.

Scott, W.E., Hoblitt R.P., Torres, R.C., Self, S., Martinez, M.L., Nillos, T., 1996. Pyroclastic flows of the June 15, 1991, climactic eruption of Mount Pinatubo. In: Newhall, C.G., Punongbayan, R.S. (eds.), Fire and Mud. Eruptions and Lahars of Mt. Pinatubo, Philippines. University of Washington Press, Seattle, 545-570.

Sparks, R.S.J., Sigurdsson, H., Wilson, L., 1977. Magma mixing: a mechanism for triggering acid explosive eruptions. Nature 267, 315-318.

Stormer, J.C., 1983. The effects of recalculation on estimates of temperature and oxygen fugacity from analyses of multi-component iron-titanium oxides. American Mineralogist 68, 586-594.

Streck, M.J., Grunder, A.L., 2008. Phenocryst-poor rhyolites of bimodal, tholeiiticprovinces: the Rattlesnake Tuff and implications for mush extraction models. Bulletin of Volcanology 70, 385-401.

Sun, S.S., McDonough, W.F., 1989. Chemical and isotopic systematics of ocean basalts: implications for mantle composition and processes. Magmatism in the Ocean Basins 42, 313-345.

Tahira, M., 1992. Infrasound waves generated by volcanic eruptions. Acoustical Society of Japan 48, 742-748 (in Japanese).

Tahira, M., Nomura, M., Sawada, Y., Kamo, K., 1996. Infrasonic and acoustic-gravity waves generated by the Mount Pinatubo eruption of June 15, 1991. In: Newhall, C.G., Punongbayan, R.S. (eds.), Fire and Mud. Eruptions and Lahars of Mt. Pinatubo, Philippines. University of Washington Press, Seattle, 601-614.

Tomiya, A., Miyagi, I., Saito, G., Geshi, N., 2013. Short time scales of magma-mixing processes prior to the 2011 eruption of Shinmoedake volcano, Kirishima volcanic group, Japan. Bulletin of Volcanology, 75, 1-19.

Toya, N., Bam, M., Shinjo, R., 2005. Petrology of Aoso volcano, northeast Japan arc: temporal variation of the magma feeding system and nature of low-K amphibole andesite in the Aoso-Osore volcanic zone. Contributions to Mineralogy and Petrology 148, 566-581.

Tsune, A, 2005. Maa Balance Calculator Coded in Java. Geoinformatics 16, 235-241 (in Japanese with English abstract).

Ukawa, M., Ohtake, M., 1987. A monochromatic earthquake suggesting deep-seated magmatic activity beneath the Izu-Ooshima volcano, Japan. Journal of Geophysical Research, 92, 12649-12663.

Umakoshi, K., Shimizu, H., Matsuwo, N., 2001. Volcano-tectonic seismicity at Unzen volcano, Japan, 1985-1999. Journal of Volcanology and Geothermal Research, 112, 117-131.

Van Orman, J.A., Crispin, K.L., 2010. Diffusion in oxides. Reviews in Mineralogy and Geochemistry, 72, 757-825.

Viccaro, M., Giuffida, M., Nicotra, E., Cristofolini, R., 2016. Timescales of magma strage and migration recorded by olivine crystals in basalts of March-April 2010 eruption at Eyjafjallajokull volcano, Iceland. American Mineralogist, 101, 222-230.

Wada, K., 2000. Magma plumbing system in O-akan volcano, eastern Hokkaido, Japan: shallow-felsic and deep-mafic magma chambers inferred from petrological study of the O-akan mixed basaltic andesite. Reports of the Taisetsuzan Institute of Science, 34, 46p (in Japanese).

Wark, D.A., Spear, F.S., 2005. Titanium in quartz: cathodoluminescence and thermometry. Geochimica et Cosmochimica Acta, 69, A592.

Wark, D.A., Hildreth, W., Spear, F.S., Cherniak, D.J., Watson, E.B., 2007. Pre-eruption recharge of the Bishop magma system. Geological Society of America, 35, 235-238.

Watanabe, S., Widom, E., Ui, T., Miyagi, N., Roberts, A.M., 2006. The evolution of a chemically zoned magma chamber: The 1707 eruption of Fuji volcano, Japan. Journal of Volcanology and Geothermal Research 152, 1-19.

White, R.A., 1996. Precursory deep long-period earthquakes at Mount Pinatubo: Spatio-temporal link to a basalt trigger. In: Newhall, C.G., Punongbayan, R.S. (eds) Fire and mud. Eruptions and lahars of Mt. Pinatubo, Philippines. University of Washington Press, Seattle, 307-328.

Wiebe, R.A., 1988. Structural and magmatic evolution of a magma chamber: The network island layered intrusion, Nain, Labrador. Journal of Petrology 29, 383-411.

Wilcox, R.E., 1954. Petrology of Paricutin volcano, Mexico. Bulletin of U.S. Geological Survey, 281-349.

Winther, K.T., 1996. An experimentally based model for the origin of tonalitic and trondhjemitic melts. Chemical Geology, 127, 43-59.

Wolf, M.B., Wyllie, P.J., 1994. Dehydration-melting of amphibolite at 10 kbar: the affects of temperature and time. Contributions to Mineralogy and Petrology, 115, 369-383.

Wolfe, E.W., Hoblitt, R.P., 1996. Overview of the Eruptions. In: Newhall, C.G., Punongbayan, R.S. (eds.), Fire and Mud. Eruptions and Lahars of Mt. Pinatubo, Philippines. University of Washington Press, Seattle, 3-20.

Wu, F.T., 1979. Recent tectonics of Taiwan. In Uyeda, S., Murphy, S.W. and Kobayashi, K (eds.) Geodynamics of the Western Pacific. Advances in Earth and Planetary Sciences, 6, 265-299.

Yamaguchi, Y., 1996. Basaltic end-member magma and its vesiculation and degassing during the Asama Tenmei eruption: Glass inclusions in olivine phenocryst. Fall Meeting of Volcanological Society of Japan, B20 (in Japanese).

Yoshida, K., Sasatoni, T., Ichiyanagi, M., Oshima, H., Tamura, M., 2002. Low frequency earthquake by eruptive activities of Mt. Usu in 2000. Bulletin of the Volcanological Society of Japan, 47, 507-519 (in Japanese).

Zobin, V.M., 2018. An overview of the dynamics of the volcanic paroxysmal explosive activity, and related seismicity, at Andesitic and dacitic volcanoes (1960-2010). Frontiers in Earth Science, 6, 1-16.